Observational Effects of Strong Gravity

by Kristian R. C. Beckwith

A thesis submitted to the University of Durham
in accordance with the regulations for
admittance to the Degree of Doctor of Philosophy.

Department of Physics
University of Durham
August 2005

Observational Effects of Strong Gravity

by Kristian R. C. Beckwith

PhD Thesis, October 2005

Abstract

It is now a century since Einstein tore down the edifice of classical physics, ultimately replacing it with his crowning achievement, the General Theory of Relativity, the most remarkable prediction of which is the black hole. There are many astrophysical examples of black holes, understanding which has long been a goal of high-energy astronomy. We review how these observations can be explained in terms of a two-phase accretion flow. Hard X-ray photons produced in an optically thin gas are reflected from a cool accretion disk, resulting in a complex reflection spectra, which are dominated by a narrow Iron Kα fluorescence feature at 6.4 keV (dependent on the ionisation state of the cool disk). The photons that form this spectral feature originate in rapidly moving material, close to the black event horizon. They are therefore subject to the combined dynamical effects of the accretion disk and those of General Relativity, resulting in a highly broadened line profile. The observed form of the line can then, in principle, be used as a test of the strong gravitational field of the black hole.

We have developed a new, extremely fast strong gravity code that accurately calculates the effect of strong gravity on photons originating close to the black hole event horizon, including the ability to calculate the trajectories of photons that perform multiple orbits of the black hole. We compare results from the code to the standard models describing relativistic smeared lines available to the community, finding that they match to within $\lesssim 5\%$. We apply this code to the observed shape of the Iron Kα line and show that

the (poorly understood) vertical structure of the accretion disk strongly affects the derived radial emissivity profile, which has important consequences for the interpretation of observational data.

Following on from this, we consider the spectral and imaging properties of thin Keplerian accretion disks, fully including the effects of photons that perform multiple orbits of the black hole. Viewed at high inclinations, these photons can carry as much as $\sim 60\%$ of the total luminosity of the system, which returns to the disk at a range of radii. At low inclinations, the multiple orbit photons re-intercept the disk plane close to the black hole. For a Schwarzschild black hole, this lies within the plunging region and so the photons need not be absorbed by the disk. The resultant ring is bright it may well be possible to use these as a future test of strong gravity via X-ray interferometric images of accreting black holes.

Finally, we examine the observational properties of accretion flows where angular momentum transport is provided by the Magneto-Rotational Instability. It is shown that the dissipation profile derived from the magnetic 4-current density in these simulations provides a remarkably close match to that derived from the standard relativistic disk model at large radii. At small radii however, the descriptions of dissipation in the two models are rather different, which has important *observational* consequences. With this model of dissipation, we examine the observed properties of optically thin accretion flows, discussing the implications of these calculations for the low / hard state of Galactic Black Holes. Additionally, we describe a simple reflection geometry for Iron Kα fluorescence, assuming that this MHD flow is optically thick in the equatorial plane. The resultant line shapes are markedly different to those predicted in the standard relativistic disk model, showing that the (currently unknown) flow dynamics are also important in shaping the line.

Contents

List of Figures

Declaration

The work described in this thesis was undertaken between 2002 and 2005 while the author was a research student under the supervision of Dr Christine Done in the Department of Physics at the University of Durham. This work has not been submitted for any other degree at the University of Durham or any other University.

Portions of this work have appeared in the following papers:

- Chapter 3: Beckwith, K. & Done, C. 2004, MNRAS, 352, 353
- Chapter 4: Beckwith, K. & Done, C. 2005, MNRAS, 359, 1217

The author has also either worked on, or been involved in the following work:

- Gregory, R.; Whisker, R.; Beckwith, K.; Done, C. 2004, JCAP, 10, 13

Acknowledgements

In all, I have spent a total of seven years at the Department of Physics, University of Durham, during the course of which I have acquired two degrees and made many friends. As such, the list of acknowledgements is rather long and varied. Firstly, I'd like to thank all of the staff at the Department who have taught (and put up with) me during this time, in particular Dr Steve Rayner, Dr Paula Chadwick, Dr John Lucey, Dr Stewart Clark and Prof. Carlos Frenk. Secondly, I'd like to thank Mr Bill Frith, Dr Mark Swinbank, Dr Phil Outram, Dr Marek Gierliński, Mr Richard Whittaker, Mr Claudio Della, Mr Mark Norris, Mr Nic Ross and Ms. Jeannette Getty for general help, friendship and encouragement over the last three years.

My PPARC Ph.D. studentship was carried out under the supervision of Dr Chris Done, who introduced me as a naive undergraduate to the wonders of the General Theory of Relativity. Over the past three years, her guidance, encouragement and general enthusiasm have proved invaluable, thank you. Special mentions are needed for Dr Marek Gierliński for physics, proof reading, computing and XSPEC along with Mr Alan Lotts for his tireless efforts to keep the computers working. Thanks also go to Prof. Eric Agol, Prof. Julian Krolik, Prof. Vladimir Karas, Prof. Rob Fender, Prof. John Miller and Dr Michal Dovčiak for help and encouragement.

None of this could have been possible without the love and support of my parents over the past twenty-four years and eight months (to the day!), I am eternally in their debt. Finally, I would like to dedicate this work to my girlfriend, Miss Alexandra Sanderson who has given me her love, support, friendship and tolerance for the past five years, without which none of this would have been possible.

Kris Beckwith, Durham, 18th August 2005

Theory: We know everything, but nothing works;

Practice: Everything works, but we don't know why;

Here we combine theory and practice: nothing works and we don't know why!

Dr Marek Gierliński

Chapter 1

General Relativity and The Failure of Classical Physics

Abstract

The failure of the Michelson-Morley experiment led to the downfall of classical physics as the description of the universe. Einstein, exactly one century ago[1], seized this remarkable opportunity with breath-taking audacity, remoulding the classical concepts of space and time into a singular entity, *spacetime*. However, these ideas were directly in conflict with Newtonian Gravity, which led Einstein to his crowning achievement, the General Theory of Relativity. To date, this modern theory of gravity has passed every test to which it has been subject with flying colours, but what of the future? As an introduction to the remainder of this work, we outline the shortcomings of classical physics and how these led Einstein to a General Theory of Relativity, along with one of the theories most remarkable predictions, the Black Hole.

1.1 The Failure of Classical Physics

The beginning of the twentieth century witnessed a remarkable revolution in our understanding of the universe. The failure of the Michelson-Morley experiment to detect the

[1] at the time of writing

motion of the Earth through the mysterious ether, through which it was thought that Maxwell's Electromagnetic waves must propagate, lead to the realisation that 'something was rotten in the state of Denmark'. At the time, a little known Swiss patent clerk wondered with his friends as to whether one would see ones image in a mirror whilst travelling at the speed of light. This simple puzzle marked the beginning of a quest that would shatter classical physics, for the young patent clerk was Albert Einstein.

Einstein finally rejected the notion of the all-pervading ether, leading to his 1905 paper, *'On the Electrodynamics of Moving Bodies'* (Einstein, 1905), containing his two famous postulates of Special Relativity:

> The phenomena of electrodynamics as well as of mechanics possesses no properties corresponding to the idea of absolute rest. They suggest rather that ... the same laws of electrodynamics and optics will be valid for all frames of reference for which the equations of mechanics hold good. We will raise this conjecture (the purport of which will hereafter be called the 'Principle of Relativity') to the status of a postulate, and also introduce another postulate, which is only apparently irreconcilable to the former, namely, that light is always propagated in empty space with a definite speed c which is independent of the state of motion of the emitting body

These two postulates enable Einstein to derive the transformation (previously derived by Lorentz, see e.g. Lorentz, 1928) between two inertial frames, S, S' moving with relative velocity u:

$$x' = \gamma(x - ut);\;\; y' = y;\;\; z' = z;\;\; t' = \gamma(t - \frac{ux}{c^2});\;\; \gamma = \frac{1}{\sqrt{1 - \frac{u^2}{c^2}}} \tag{1.1}$$

Clearly, the application of the Lorentz Transformations result in the mixing of the spatial and temporal co-ordinates (rotation in a four-dimensional space). Space and time can no longer be considered as distinct entities, but instead must be unified into a single whole, *spacetime.*

The fundamental implications of Special Relativity for classical physics do not finish there, however. Newtonian mechanics, based on the Galilean transformation was reformulated such that it was consistent with the Lorentz transformations, a tedious process that is discussed in many texts on the subject (see e.g. Jackson, 1975). More interestingly, Special Relativity is fundamentally incompatible with the 'jewel in the crown' of classical physics, Newtonian Gravity. Newton's Universal Law of Gravitation tells us that the gravitational force between two bodies, F_G is proportional to their masses, m_1, m_2 and inversely proportional to the square of the separation between them, r^2:

$$F_G \propto \frac{m_1 m_2}{r^2} \tag{1.2}$$

However, Newtonian gravity makes no comment about the nature of transmission of this force that links the two bodes. Furthermore, the theory predicts that changes in the mass of either of the bodies, or the separation between them results in an instantaneous change in this force. This prediction is clearly at odds with Special Relativity, where nothing can travel faster than the speed of light.

There is a further question upon which Newtonian gravity is disturbingly silent. Newtons First Law of Motion states that the acceleration of a body, a is equal to the force acting upon it, F, divided by the inertial mass of the body, m_i:

$$a = \frac{F}{m_i} \tag{1.3}$$

For a body falling under the influence of the gravitational field of a body of mass, M, we therefore have that:

$$a = \frac{GM}{r^2}\frac{m_g}{m_i} \tag{1.4}$$

Here, G is Newton's Universal Gravitational constant and m_g is the gravitational mass of the falling body. Experimentally it is found that that the ratio m_g/m_i is a constant to one part in 10^{12}, yet Newtonian gravity gives no indication as to why this should be the case. Contrast this with the situation in Electromagnetism, where the force acting

between two charged particles (with charges e_1, e_2, masses m_1, m_2) is given by:

$$F = k\frac{e_1 e_2}{r^2}$$

In this case, the acceleration acting on particle 1 due to particle 2 is given by:

$$a = k\frac{e_2}{r^2}\frac{e_1}{m_1}$$

Here, the ratio e_1/m_1 varies hugely, for example, electrons and protons both posses the same charge, yet their masses differ by three orders of magnitude.

In fact, this equivalence of inertial and gravitation mass presents Special Relativity with something of a problem. If these masses are equivalent, then it is impossible to distinguish between a free-falling reference frame in a gravitational field and an accelerated reference frame in free space. Special Relativity is a theory of inertial, not accelerated frames and if we cannot distinguish between a free-falling frame in a gravitational field and an accelerated frame in free space, then an inertial frame cannot be applied in the presence of a gravitational field.

Einstein, however, was able to turn this seemingly fundamental contradiction to his advantage in 1907, when he had what he later described as 'the happiest thought of my life':

> I was sitting in a chair in the patent office at Bern when all of a sudden a thought occurred to me: "If a person falls freely he will not feel his own weight." I was startled. This simple thought made a deep impression on me. It impelled me toward a theory of gravitation

Simply put, gravity can be eliminated by surrendering oneself to its hands, which raises a fundamental problem with the infinite inertial reference frame described by Special Relativity. In the presence of a massive body, different paths in spacetime must be freely falling at different rates to properly remove the effects of gravity and it is clearly impossible to define a global reference frame that accomplishes this feat. Instead we

must define a Local Reference Frame which is small enough that the acceleration due to gravity is constant across the frame. This notion is embodied in the cornerstone of General Relativity, the Principle of Equivalence:

> All local, freely falling, non-rotating laboratories [locally inertial reference frames] are fully equivalent for the performance of all physical experiments.

Einstein followed this remarkable realisation with the crowning achievement of General Relativity, the deduction of the Einstein Field Equations (Einstein, 1916):

$$R_{\mu\nu} - \frac{1}{2}g_{\mu\nu}R + \Lambda g_{\mu\nu} = \frac{8\pi G}{c^4}T_{\mu\nu} \tag{1.5}$$

These equations allows to relate the mass-energy density, encapsulated in the stress-energy tensor, $T_{\mu\nu}$ to the curvature of spacetime, described by the metric $g_{\mu\nu}$[2]. The above is the most general form of the Einstein Equations, which includes the cosmological constant, Λ. Einstein regarded these equations as too complex to allow a solution to ever be found. However, in 1916, just one year after the publication of General Relativity, the German astronomer, Karl Schwarzschild published an exact solution to the Einstein equations describing the external static, spherically symmetric gravitational field of a point mass, M, known as the Schwarzschild metric:

$$ds^2 = g_{\mu\nu}dx^\mu dx^\nu = \left(1 - \frac{2GM}{c^2 r}\right)c^2dt^2 - \left(1 - \frac{2GM}{c^2 r}\right)^{-1} dr^2 - r^2\left(d\theta^2 + \sin^2\theta d\phi^2\right) \tag{1.6}$$

Even more remarkably, Kerr (1963) was able to write down an explicit analytic solution describing the exterior of a rotating point mass (see e.g. Misner et al., 1973; Chandrasekhar, 1983). This solution, known as the Kerr metric, will be the subject of extensive discussion in Chapter 3.

[2]Note that the Ricci tensor, $R_{\mu\nu}$ and the curvature scalar, R are generated from the Riemann curvature tensor, $R^\alpha_{\beta\gamma\delta}$, which is the only tensor that can be constructed from the metric and its second derivatives (Weisstein, 2005).

1.2 Black Holes & Properties of Strong Gravitational Fields

General Relativity, as encapsulated in the Einstein Field Equations (Eqn. 1.5), provides a remarkable theoretical framework to understand the relationship between mass-energy and spacetime curvature. However, the Einstein Field Equations are not an *ab-initio* prediction of the theory, rather they were deduced by Einstein as having the correct mathematical form to describe this relationship. Their validity (or otherwise) does not lie in some esoteric mathematical proof, rather it lies in the experimental verification of their predictions, which, fortunately, was rapidly forthcoming. We have already seen that Newtonian gravity was undone theoretically by its inconsistency with the fundamental principles of Special Relativity. Furthermore, Newtonian gravity was unable to explain 43" per century of the advance of the perihelion of Mercury, which led some of the physicists of the time (the mid-Nineteenth century) to suggest that either gravity did not obey an exact inverse square law, or that another (as yet unseen) planet must exist inside the orbit of Mercury. Einstein's first act upon completion of General Relativity was to apply this new theory of gravity to this problem, with the remarkable result that this new theory explained exactly the perihelion shift. In fact, General Relativity has passed every experimental test to which it has been subjected, from predictions regarding the passage of light through curved spacetime to the effect of time dilation in the gravitational field of a massive body (see e.g. Will, 2001).

General Relativity's most remarkable predictions can be found in the Kerr metric describing a rotating point mass, which reduces to the Schwarzschild metric (Eqn. 1.6) in the non-rotating limit. These solutions to the Einstein Field Equations, the properties of which will be discussed extensively in Chapter 3, predict that, if one concentrates a sufficient amount of mass in a sufficiently small space, then the resulting gravitational field will be so strong that not even light can escape. Naively, we can see this in Newtonian

gravity by following the Eighteenth century amateur astronomer and clergyman, George Michell (Michell, 1784). He proposed that if light were indeed composed of particles (as was the case in Newtons corpuscular theory of light), then it would be subject to the influence of gravity. As such, light would be unable to escape from a star whose escape velocity was the speed of light, $v_{esc} = c = \sqrt{2GM/r_*}$, implying that $r_* = 2GM/c^2$, which for a star with the mass of the Sun, is approximately $3km$.

In full General Relativity, such a radius is described by a null hyper-surface, understanding the nature and existence of which is somewhat more complex. Notice that something strange occurs in the Schwarzschild metric at $r_S = 2GM/c^2$, known as the Schwarzschild radius, whilst remembering that the co-ordinates in which the line element (Eqn. 1.6) is written are physically meaningless[3]. In the region below r_S, notions of space and time are reversed and material within this region must necessarily fall radially inwards. Furthermore, if a photon were to be emitted by this material, then it would also necessarily fall to ever smaller radii, independent of its in initial direction. The radius r_S therefore marks the boundary (the event horizon, r_h)[4] from within which not even light can escape. Any object whose radius falls within this boundary is effectively cut-off from the outside world, able to digest any object foolish enough to approach it - a black hole. The predictions of General Relativity as to the nature of these compact objects (i.e those objects with $r_* \approx r_h$) do not end here - many of the properties of spacetime contrast markedly with Newtonian gravity. These properties are discussed at length in Chapter 3 - here, we merely give a summary of those that are most important for our purposes[5]:

- Particle orbits: Stable circular orbits are only possible outside the 'marginally stable

[3]Note that it is possible to transform to co-ordinates where the strange behaviour of the line element at r_S disappears - a co-ordinate singularity

[4]Note that whilst $r_h = r_S$ for the Schwarzschild metric, this is not true in general (see Chapter 3)

[5]Light bending and gravitational redshift are not unique to black holes - they are a fundamental consequence of General Relativity. The solutions describing black holes enable us to make specific prediction regarding these effects, which can then be tested by comparison to observational data.

orbit', once within this radius, particles are necessarily captured by the black hole.

- Light bending: Photons follow null geodesics, which are determined by the curvature of spacetime, i.e. light no longer travels in straight lines. Light is able to exist in unstable circular orbits close to the black hole.

- Gravitational Redshift: Photons emitted from radius r_e with energy E_e are received at radius r_o with energy E_o where $E_o/E_e = \sqrt{(g_{tt})_o/(g_{tt})_e}$.

Furthermore, if we consider the general case of a rotating black hole, then we have an additional property that we wish to test:

- Frame dragging: Material close to a rotating black hole is dragged round by the angular momentum of the hole itself. Within the 'ergosphere', no geodesics exhibiting purely radial motion are possible - test particles are forced to rotate in the same direction as the black hole.

Clearly, confirming the existence and nature of black holes is an extremely important step in confirming the validity of General Relativity. The past three decades have seen remarkable progress in attempting to accomplish this aim, driven (in part) by the rapid development of the relatively young field of X-ray astronomy. It now seems almost certain that supermassive black holes ($M \approx 10^8 M_\odot$) are present at the hearts of many (if not all) Galactic Nuclei, whilst stellar mass black holes are thought to be the compact companion in many Galactic Binary systems. In recent years, a new class of Ultraluminous X-ray sources have emerged, which may well harbour intermediate mass black holes, although this result is still uncertain (see e.g. Miller & Colbert, 2004). Testing the properties of the associated space-times remains a highly controversial topic however, but even here, efforts have met a remarkable degree of success, as we shall shortly see.

Chapter 2

Black Holes, Accretion and Tests of Strong Gravity

Abstract

Astrophysical black holes are macroscopic objects, ranging from the stellar mass black holes found in many galactic sources to the supermassive black holes found at the hearts of many galactic nuclei. In this Chapter, we outline how such objects are detected and examine in detail the high-energy spectral characteristics of stellar mass black holes where gas is accreted by means of a disk. We briefly review how, in these systems, it is possible to interpret the two canonical spectral states in terms of two corresponding accretion geometries, which can be used to drive our understanding of the physics of accretion. Illumination of gas within the accretion disk necessarily results in the production of a complex reflection spectrum, which, for low to moderately ionised material contains an intrinsically sharp Iron Kα fluorescence line at $\sim$ 6.4 keV. The observed properties of photons emitted from an accretion disk within a strong gravitational field are determined by both the accretion disk and the gravitational potential, which has led to the adoption of the properties of the Iron Kα line as a test of strong gravity. We review the processes by which this spectral feature is formed and briefly examine the observational evidence in support of these ideas.

2.1 Detecting Black Holes

The formation of a stellar mass black hole represents the likely end point of stellar evolution for massive stars. Calculations of the structure of the degenerate remnants of these objects, using realistic equations of state and applying General Relativity, indicate that the upper mass limit for a relativistic compact star is $2-3M_{\odot}$ - above this limit collapse to a black hole seems inevitable. The question therefore is to identify such objects within the galaxy - black holes are, by their very nature, dark objects and so we must infer their existence from secondary data. Gas accreted onto a stellar mass compact object within a binary system is expected to emit radiation in the medium to hard X-ray bands (see Section 2.4), which implies that luminous galactic X-ray sources may well be associated with stellar mass black holes. We can determine whether such as system does indeed contain a black hole by use of the mass function, $f(M)$:

$$f(M) \equiv \frac{P_{orb}K_2^3}{2\pi G} = \frac{M_1 sin^3 i}{(1+q)^2} \tag{2.1}$$

$f(M)$ allows us to infer the mass of the compact star (the primary), M_1 from observations of the inclination, i and the mass ratio, $q = M/M_1$, where M is the mass of the companion star. Inspection of Eqn. 2.1 reveals that $f(M)$ represents a minimum estimate for the mass of the compact star in a binary system. Therefore, if we determine that $f(M) \gtrsim 3M_{\odot}$, then this alone is sufficient to strongly imply that the compact star is indeed a black hole. To date, 12 galactic binary systems have been confirmed as containing a black hole using this technique, with a further 6 being confirmed by combination with additional data, which implies that $M_1 \gtrsim 3M_{\odot}$. Additionally another 22 binary systems are strongly suspected of containing a black hole primary. For a detailed review of all of these systems, the reader is referred to McClintock & Remillard (2003) and references therein. Of course, the mass of the compact object in the binary system may not exceed the critical mass for gravitational collapse - in this case the compact object is likely either a Neutron Star (for masses $1.4-2.0M_{\odot}$) or a White Dwarf (for masses $< 1.4M_{\odot}$). These systems are,

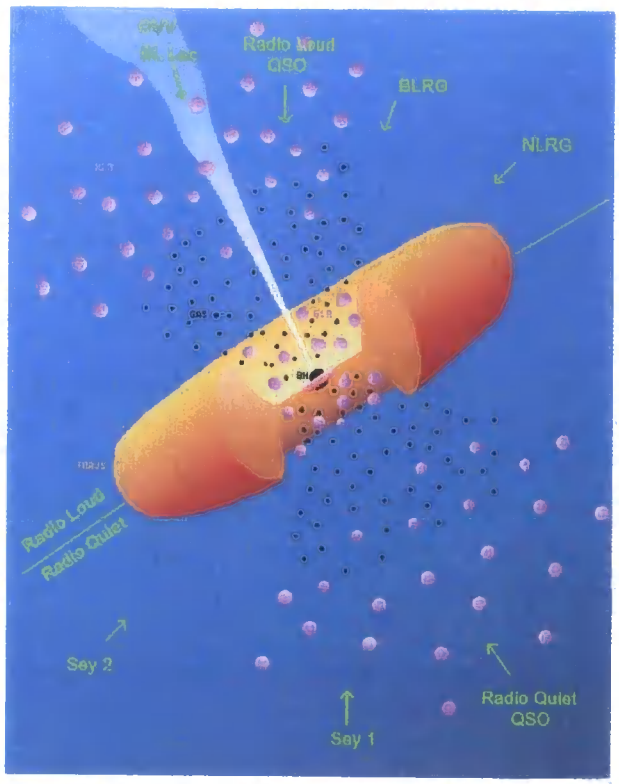

Figure 2.1: Artistic interpretation of the unified model of Active Galactic Nuclei. For clarity, we have added labels indicating observational classification of the nucleus, dependent on observers line-of-sight. Created with support to AURA/ST Scl from NASA contract NAS5-26555.

in general, rather more complex than those containing black holes, mainly due to the existence of a stellar surface (i.e. the existence of a boundary layer between the inner regions of the accretion flow and the surface along with the presence of a stellar magnetic field).

Examples of astrophysical black holes are not limited to the end points of stellar evolution, however. It has long been suspected that the centre of our own Galaxy, the Milky way, harbours a massive dark object. Recent infrared observations by two independent groups have shown that the orbits of stars in the nucleus are under the influence of a mass

of $3 \times 10^6 M_\odot$ concentrated within a distance of $2 \times 10^{13} m$ (Schödel et al., 2002; Eisenhauer et al., 2003; Ghez et al., 2003, 2005). Furthermore, observations of the (seemingly) associated radio source, Sagittarius A* indicate that the dark object possesses $M \geq 10^5 M_\odot$, $R \leq 27 R_S$ (Bower et al., 2004). It therefore seems likely that the galactic centre contains a supermassive black hole. Taken in context, this result is unsurprising, Magorrian et al. (1998) had already used extensive data from the Hubble Space Telescope to demonstrate that most, if not all, nucleated galaxies harbour a supermassive black hole at their centre.

However, as with the stellar mass black holes, it is far easier to identify supermassive black holes by looking for copious amounts of radiation being produced in a small region. The nuclear luminosity of many galaxies (i.e emission from the very centre of the galaxy) far exceeds that of the combined emission from the rest of the galaxy. Not only are these nuclei extremely bright, but are also highly variable, which implies a large energy output in a small region. The only description of these Active Galactic Nuclei (AGN) which appears capable of describing the central engine powering the output of the galactic nucleus is accretion onto a super-massive black hole (Lynden-Bell, 1969). One can explain the bewildering variety of associated phenomena via the unified model of AGN (Figure 2.1, see e.g. Krolik, 1999). In this description, emission from the central disk is reprocessed on larger scales giving rise to the wide variety of phenomena associated with these objects (examples of which are show in Figure 2.1), with the model gaining widespread acceptance through the work of Antonucci & Miller (1985).

2.2 Observing Black Holes

It seems likely that many astronomical systems contain a massive compact object whose properties strongly resemble those of the black holes predicted by Einstein's General Relativity. *Proving* that these are indeed the black holes predicted by General Relativity and that their properties are correctly described by General Relativity is somewhat more challenging. To accomplish this, we need more detailed information than it is possible

to obtain from the mass function (in the case of the BHBs) or qualitative arguments regarding the properties of AGN.

We first turn our attention to the Black Hole Binaries. Here, if the companion star fills its Roche Lobe, then mass transfer can occur through the inner Lagrange point and flow towards the compact object. This includes all of the systems where the companion star has lower mass than the primary (known as a Low Mass X-ray Binary, LMXB). Alternatively, if the companion star is of sufficiently high mass ($\gtrsim 10M_{\odot}$), then it is capable of driving a strong wind, which can then be accreted by the compact object (known as a High Mass X-ray Binary, HMXB). Independent of the type of system, the fate of the transferred matter depends principally on three physical properties / processes (see e.g. Frank et al., 2002, for a review):

1. The angular momentum of the material
2. The physical process by which the material loses angular momentum
3. The physical process by which the material cools

We refer to the structures formed by the gas in this process as the *accretion flow*, which (generically) must provide some method for the gas to lose angular momentum (and hence flow towards the black hole) and, if the flow is to be luminous, some method by which gravitational potential energy released in the accretion process can be converted into radiation. For LMXBs, the luminosity of the system is dominated by emission in the X-ray spectral band, which has its origin in the inner regions of the accretion flow and is accompanied by emission in the optical band due to reprocessing of the X-ray flux. By contrast, the spectra of HMXBs are rather more complex, due to (for example) absorption and / or a wind from the companion star. In common with many other types of accreting objects (from young stars to AGN), BHBs also exhibit outflows and collimated jets, which also seem to posses the relativistic velocities observed in similar phenomena in Active Galactic Nuclei. Co-ordinated radio, infrared and X-ray observations of sources

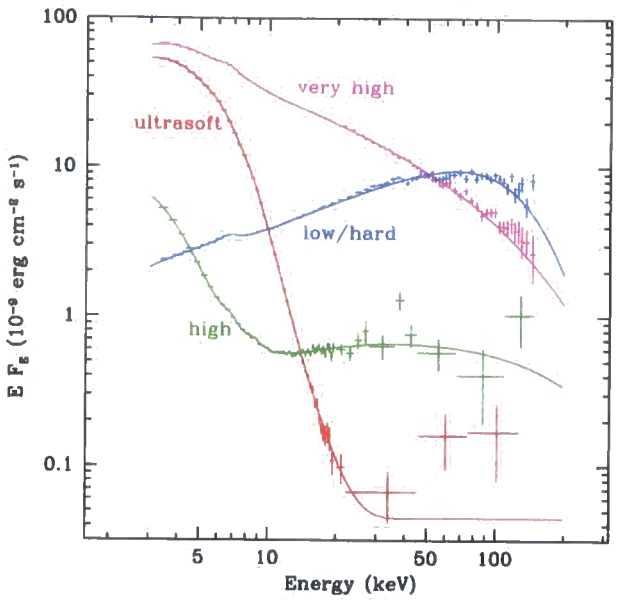

Figure 2.2: "Characteristic spectra from XTE J1550-564. The VHS spectrum is from MJD 51077 and corresponds to $\sim 2/3$ of the overall maximum of the outburst." Adapted from Zdziarski & Gierliński (2004)

exhibiting these phenomena (such as GRS 1915+105) show a strong correlation between the X-ray spectral properties of the accretion flow and the behaviour of the jet, which provides us with useful insights into the behaviour of the accreting matter in these systems (Fender & Belloni, 2004).

Some of the most informative insights into the behaviour of Black Hole Binaries[1] have, in recent years, been provided by the fields of X-ray spectroscopy and timing. The unprecedented sensitivity, accuracy, resolution and coverage provided by the high-energy observatories, *RXTE, BeppoSAX, Chandra, XMM-Newton* have enabled rapid advances in our understanding of the bewildering variety of phenomena exhibited by

[1]In what follows, when we refer generically to Black Hole Binaries we are referring to examples of these systems where the transferred material is in possession of a large amount of angular momentum (i.e. mass transfer via Roche Lobe overflow) and hence accretes via a disk, rather than a wind or other exotic method

these sources. The recently launched Japanese observatory *Astro-E2* will further enhance our understanding, as it is capable of providing high-resolution, broad band spectra of many of these systems.

In the most simplistic description (following Done & Gierliński, 2004; Zdziarski & Gierliński, 2004), the X-ray spectra associated with these sources can be divided into two categories (known as *spectral states*). The first of these, known as the soft state, is dominated by a strong black body component, peaking at $\sim 1keV$ for a $10M_{\odot}$ black hole at the Eddington luminosity[2] (having its origin in thermalised emission from a cold accretion disk) along with an additional X-ray tail to higher energies (the cut-off of which is, as yet, undetermined). The properties of this X-ray tail allow us to divide the soft state into three sub-categories: (i) the ultrasoft state (US, weak tail); (ii) the high state (HS, moderate tail); (iii) the very high state (VHS, strong tail). At lower luminosities (as denoted by $L/L_{\rm Edd}$), Black Hole Binaries exhibit a rather different spectra, known as the low/hard state (LS), characterised by a weak soft black body component, but is dominated by emission at energies substantially higher than that of the disk, which cut-off at energies $\gtrsim 100keV$. To produce any emission at energies substantially higher than that of the intrinsic disk energy requires that some fraction of the gravitational potential energy is dissipated in optically thin regions, so that a small number of electrons gain the majority of the released energy and are therefore able to produce hard X-ray emission by Compton up-scattering of lower energy photons.

It is possible to interpret the two distinct spectral states observed in BHBs in terms of two different accretion geometries (see Figures 2.2, 2.3 Zdziarski & Gierliński, 2004; Done & Gierliński, 2004). The soft states correspond to a cold accretion disk, surrounded by an optically thin, Comptonising corona, the relative strength of which is correlated with the strength of the hard X-ray tail. By contrast, the canonical hard state corresponds to an optically thin, geometrically thick accretion flow close to the black hole, joining

[2]The Eddington luminosity, $L_{\rm Edd}$ is defined as the luminosity at which the gravity is exactly balanced by radiation pressure, for a system with negligible angular momentum

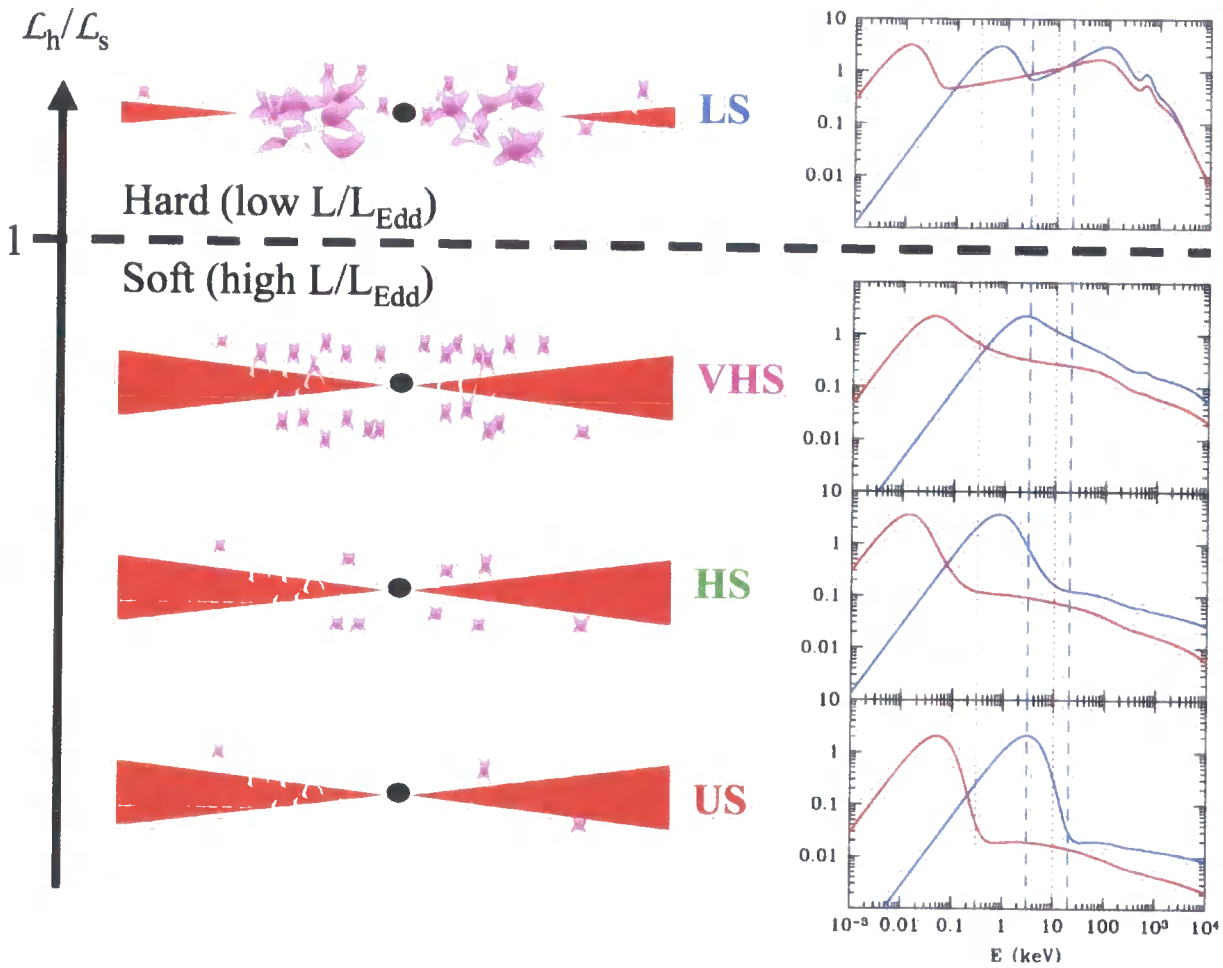

Figure 2.3: Schematic representations of the likely geometries associated with the various spectral states of Black Hole Binaries, shown as a function of the ratio of the power in the hot electrons to that in the seed photons illuminating them, $\mathcal{L}_h/\mathcal{L}_s$. On the right-hand side of the panel are shown the spectra associated with the state for the BHBs (blue lines) and the expected spectra for an equivalent geometry in AGN (red lines). Figure courtesy of Chris Done (unpublished)

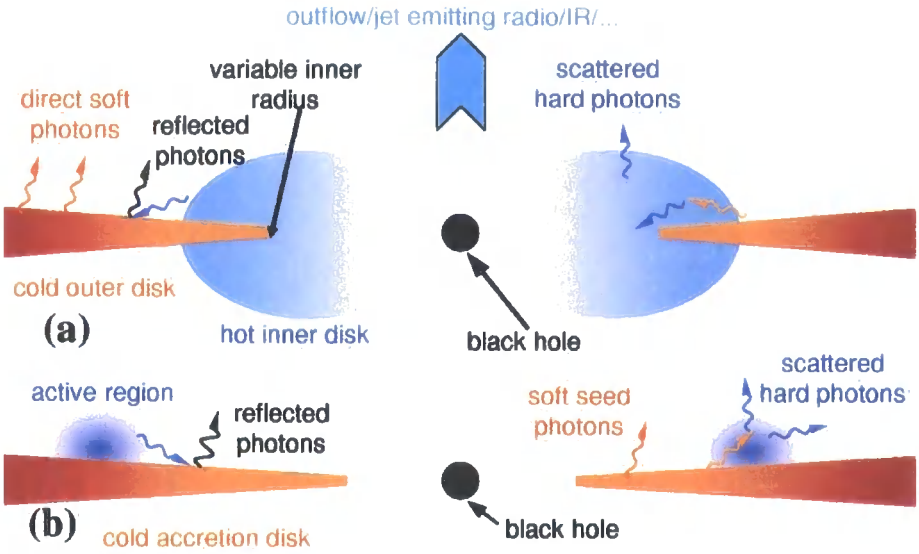

Figure 2.4: "(a) A schematic representation of the likely geometry in the hard state, consisting of a hot inner accretion flow surround by [an] optically-thick accretion disk. The hot flow constitutes the base of the jet(with the counter-jet omitted from the figure for clarity). The disk is truncated far away from the minimum stable orbit, but it overlaps with the hot flow. The soft photons emitted by the disk are Compton up-scattered in the hot flow, and emission from the hot flow is partly Compton-reflected from the disk. (b) The likely geometry in the soft state consisting of flares / active regions above an optically-thick accretion disk extending close to the minimum stable orbit. The soft photons emitted by the disk are Compton upscattered in the flares and emission from the flares is partly Compton-reflected from the disk." Taken from Zdziarski & Gierliński (2004)

on to a cold accretion disk at larger radii. It is important to realise that the spectral states of individual sources evolve in time, thereby enabling us to trace the evolution of the accretion flow. Note, however, that (in general), state transitions in LMXBs can take place at a wide range of luminosities and so the spectral state for a particular source at any given moment is determined by the history of the source (*hysteresis*, see Zdziarski & Gierliński, 2004). The maximum luminosity associated with the hard state (determined by cooling processes within the flow) overlaps that of the minimum luminosity associated with the soft state (determined by evaporation of the cold disk) and so the transition can take place at a range of luminosities. Fender et al. (2004, 2005) have recently proposed a model, based on combined radio, infrared and X-ray observations of a range of BHBs which shows how the spectral evolution of BHBs can be related to the changing accretion geometry and, more importantly, to injections of relativistic blobs into the jet observed in many BHBs (see Figure 2.5).

Black holes are incredibly simple objects, which can be fully described by knowledge of their mass and angular momentum (see Chapter 3). Theoretically, we should therefore be able to understand the behaviour of the supermassive black holes found at the hearts of AGN simply by scaling, for a given $L/L_{\rm Edd}$, the observed properties of the accretion flow in BHBs (Done & Gierlinski, 2005). The principal effect (in theory at least) of this vast increase in black hole mass is to move the peak energy of the spectrum from $\sim 1keV$ in BHBs to $\sim 10eV$ in AGN (for systems emitting at $L_{\rm Edd}$, see Section 2.4). This complicates the picture for observations of AGN in the canonical soft state[3] as the $2-10keV$ spectral band is now dominated by the highly variable X-ray tail due to the optically thin corona, in contrast to the BHBs, which are disk dominated here (see Figure 2.3).

[3]such as the PG quasars (the likely counterpart of the high state, see Sanders et al., 1989; Elvis et al., 1994; Laor et al., 1997; Boroson, 2002) and NLS1's (the likely counterpart of the very high state, see Boller et al., 1996; Brandt et al., 1997)

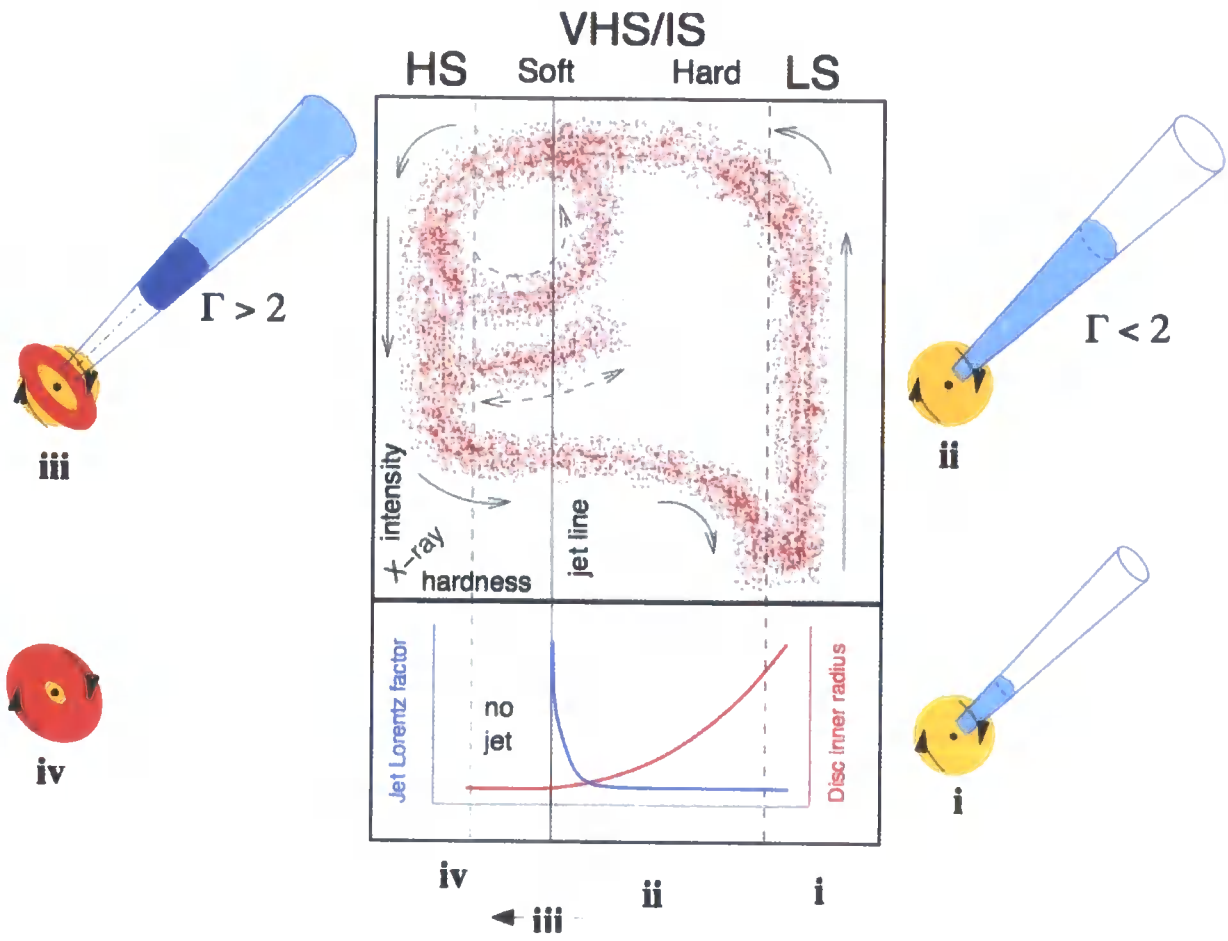

Figure 2.5: "A schematic of our simplified model for the jet-disc coupling in black hole binaries. The central box panel represents an X-ray hardness-intensity diagram (HID); HS indicates the high/soft state, VHS/IS indicates the very high/intermediate state and LS the low/hard state. In this diagram, X-ray hardness increases to the right and intensity upwards. The lower panel indicates the variation of the bulk Lorentz factor of the outflow with hardness, in the LS and hard-VHS/IS the jet is steady with an almost constant bulk Lorentz factor $\Gamma < 2$, progressing from state i to state ii as the luminosity increases. At some point, usually corresponding to the peak of the VHS/IS, Γ increases rapidly producing an internal shock in the outflow (iii) followed in general by cessation of jet production in a disc-dominated HS (iv). At this stage fading optically thin radio emission is only associated with a jet/shock which is now physically decoupled from the central engine. As a result the solid arrows indicate the track of a simple X-ray transient outburst with a single optically thin jet production episode. The dashed loop and dotted track indicate the paths that GRS1915+105 and some other transients take in repeatedly hardening and then crossing zone iii, the jet line, from left to right, producing further optically thin radio outbursts. Sketches around the outside illustrate our concept of the relative contributions of jet (blue), corona (yellow) and accretion disc (red) at these different stages." Taken from Fender et al. (2005)

2.3 Reflection and Iron Kα Fluorescence

In reality, the spectra of these systems are rather more complex. Consider, for example, the situation in the soft states, where we have a cold accretion disk surrounded by a hot Comptonising corona. Soft seed photons from the disk are Compton up-scattered into the hard X-ray band, which we see as the tail in the soft spectra. These hard X-ray photons are also able to re-illuminate the disk, which has important consequences for the observed spectra (see Figure 2.4b). A similar situation is possible in the hard state, where the source of hard X-ray photons is now the hot inner flow, which are incident on the disk at larger distances from the central mass (see Figure 2.4a). Additionally, it may be possible that hard X-ray photons are produced in shocked material above the spin axis of the black hole, which are then able to illuminate the disk (the lamp post model, Martocchia et al., 2000). Whatever the illumination geometry, many studies (see e.g. George & Fabian, 1991; Matt et al., 1991; Reynolds, 1996; Ballantyne et al., 2001; Ross & Fabian, 2005) have shown that illumination of a semi-infinite slab of cold gas (i.e. the disk) by a hard X-ray power law results in a complex reflection spectrum (see Figure 2.6, left-hand panel). This figure clearly demonstrates that this reflection spectrum in the $1 - 50keV$ X-ray spectral band is dominated by Iron Kα fluorescence at $6.4keV$. A detailed description of this process can be found in the excellent review by Fabian et al. (2000), the principle arguments of which we summarise here for completeness.

Hard X-ray photons incident on the slab of cold, neutral gas are subject to one of three possible outcomes, which can be grouped into two distinct categories

1. Scattering out of the slab

2. Absorption, followed by:

   - Destruction by Auger de-excitation
   - Reprocessing into a fluorescent line photon which escapes the slab

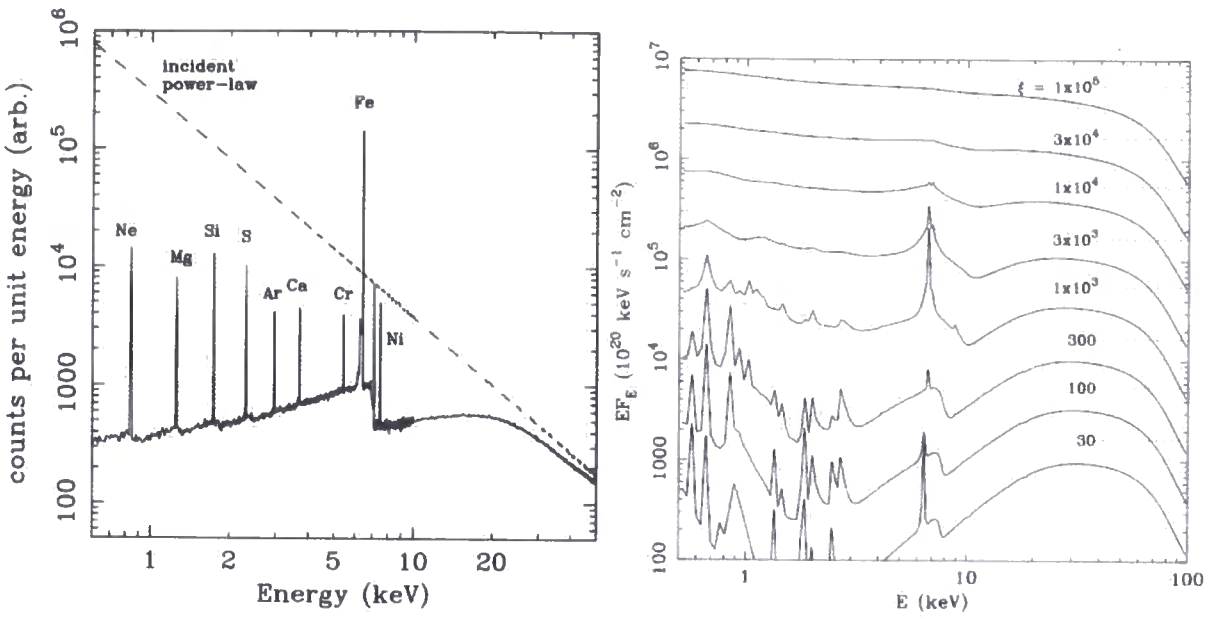

Figure 2.6: "X-ray reflection from an illuminated slab. Dashed line shows the incident continuum, and solid line shows the reflected spectrum (integrated over all angles). Monte Carlo simulation from Reynolds (1996)." (left-hand panel). "Reflection spectra from ionised matter for various values of the ionisation parameter ξ. The dotted lines show the level of the illuminating power-law continuum for each value of ξ." (right-hand panel). Both panels taken from Fabian et al. (2000)

The dominant fluorescence feature, due to Iron Kα is produced when one of the K-shell electrons of Iron (neutral or ionised) is ejected following photoelectric absorption of a X-ray. Such an event results in a excited state, which can decay by many different routes. Of these, the transition with greatest probability of producing fluorescent line emission is the decay of an L-shell electron into the vacant state in the K-shell. This requires the release of $6.4keV$, either as an emission-line photon (34% probability) or as an Auger electron (66% probability - destruction of the hard X-ray photon by Auger de-excitation).

X-ray irradiation can photo-ionise the surface layers of the disk (Ross & Fabian, 1993; Ross et al., 1999), which affects the properties of the Iron Kα line. For ionised iron, the

picture is more complex, but qualitatively similar to the neutral case, up until He-like and H-like iron ions, where line production is due to capture of free electrons (recombination), which also results in a radiative recombination continuum (RRC). Introducing the ionisation parameter, $\xi(r) \propto F_X(r)/n(r)$ (where $F_X(r)$ is the incident X-ray flux per unit area of the disk and $n(r)$ is the co-moving electron number density), enables to us to split Iron Kα fluorescence as a function of ionisation state into four different regimes (Matt et al., 1993b, 1996, see Figure 2.6, right-hand panel):

1. $\xi < 10^2$ erg cm s^{-1}: Disk is weakly ionised, reflection spectrum resembles that due to cold gas with a strong, narrow Iron Kα line at $6.4keV$.

2. 10^2 erg cm s^{-1} $< \xi < 5 \times 10^2$ ergs cm s^{-1}: Intermediate regime - partially ionised iron resonantly absorbs Kα line photons (provided the disk is non-turbulent), which are trapped in surface layers of disk (until destruction by Auger effect), leading to very weak Iron Kα line

3. 5×10^2 erg cm s^{-1} $< \xi < 5 \times 10^3$ ergs cm s^{-1}: Iron is sufficiently ionised that Auger de-excitation is no longer possible; Iron Kα photons are able to escape the disk after multiple scatterings, resulting in strong line at $6.8keV$.

4. $\xi > 5 \times 10^3$ erg cm s^{-1}: Disk highly ionised (iron completely); no line production

Provided that the disk is not too highly ionised, it therefore seems likely that we should expect to see a significant contribution to the spectrum in the X-ray spectral band due to reflection from the disc surface, in particular, a strong, narrow feature at $\sim 6.4keV$ due to Iron Kα fluorescence. Indeed, in many sources (both BHBs and AGN), this is indeed what we observe, however, the observed Iron Kα feature is rather broad, instead of the narrow line predicted by the neutral reflection spectra (see Section 2.5). In fact, Fabian et al. (1989) predicted that an intrinsically narrow spectral feature produced in an accretion disk in the strong gravitational field of a black hole should be broadened by the combined effects of gravitational redshift (due to the gravitational potential) and Doppler

broadening (due to the motion of material in the disk)[4]. This idea lies at the heart of this work, the spectra of accretion flows in strong gravity carry the imprint of not only the accretion flow (which produces the spectra in the first place) but also the gravitational field in which the photons are produced. This leads us to the somewhat bold hypothesis:

> *Detailed modelling of both the accretion flow and the propagation of photons in the spacetime of the black hole enables us to perform precision tests of Einstein's General Relativity in the strong field regime*

In the remainder of this Chapter, we treat these two ideas in turn, with accretion flows addressed in Section 2.4 and how the spectral and timing properties of these flows may be used to provide observational tests of strong gravity, along with the current status of these tests in Section 2.5.

2.4 Accretion Flows in Strong Gravity

The challenge set for theoretical discussions of accretion in Black Hole Binaries and Active Galactic Nuclei is to develop a self-consistent picture of the properties of these accretion flows that are capable of being tested against observational data. In the case of BHBs, this picture must explain the two-phase accretion flow (i.e. cold disk + hot corona; hot inner flow + cold outer disk) along with the connection to the relativistic jet. For AGN, we have a similar picture, with the state associated with the hot inner flow + cold disk probably corresponding to low luminosity (quiescent) AGN (such as the galactic centre, NGC4258) and the cold disk + hot corona corresponding to objects such a MCG-6-30-15.

The surge of efforts in this direction in the early 1970's led to the development of what is now known as the *standard model of accretion disks* that was developed by Shakura &

[4]Whilst alternative explanations of the observed broadness of the Iron Kα line do exist, the level to which these affect the line remains highly controversial (see e.g. Reynolds & Nowak, 2003, for a recent review)

Sunyaev (1973); Novikov & Thorne (1973); Page & Thorne (1974) and has been described by many authors subsequently. Our discussion largely follows the excellent treatments given in Frank et al. (2002); Krolik (1999). The standard disk model describes thin accretion disks, where gas moves on circular orbits very close to the plane $z = 0$ in the cylindrical co-ordinate system (r, ϕ, z). The dynamics of the disk are modelled through conservation of both mass and angular momentum, which are enforced, respectively, by the continuity equation and the analogue of the Navier-Stokes equation for angular momentum. Assuming that the disk is azimuthally symmetric, we are then able to follow the dynamics by use of the (one-dimensional) surface density, $\Sigma(r) = \int \rho(r, z)dz$, rather than the (two-dimensional) mass density, $\rho(r, z)$. We start by treating the problem in Newtonian gravity, which enables to examine the underlying physics without the complication introduced by relativity (the fully relativistic version of the calculation is discussed later). With these assumptions the equations governing the dynamics of the disk are:

$$\frac{\partial \Sigma}{\partial t} + \frac{1}{r}\frac{\partial}{\partial r}\left(r\Sigma v_r\right) = 0; \quad \text{(Mass Conservation)} \tag{2.2}$$

$$\frac{\partial}{\partial t}\left(r^2\Sigma\Omega\right) + \frac{1}{r}\frac{\partial}{\partial r}\left(r^3\Sigma\Omega v_r\right) = \frac{1}{2\pi r}\frac{\partial G}{\partial r}; \quad \text{(Angular Momentum Conservation)} \tag{2.3}$$

Here, Ω is the orbital frequency (for a Keplerian disk $\Omega \propto r^{-3/2}$) and v_r is the speed in the radial direction. The right-hand side of the second of these Eqn. 2.3, describes the (local) gradient of the torque, G, per unit length around an annulus. That such a torque is necessary, is clearly the case if material is to be accreted by the central object, however the nature of this torque is unclear. The boundary conditions for the above equations are rather different, dependent on whether we wish to discuss BHBs or AGN. In the former case, mass streams from the companion star by Roche Lobe overflow, through the inner Lagrange point and joins onto the outer edge of the disk. Mass is (primarily) lost from the inner edge of the disk, whilst the angular momentum of the accreting material must be transferred to the outer edge of the disk, where it is lost to the companion star by tidal torques. The situation in AGN is rather different - whilst mass is still lost from the inner edge of the disk, we have no knowledge of the source of the material forming the disk, nor

is there a convenient angular momentum sink in the form of the companion star.

Before we can progress further with the discussion, we need some model of describing the torque, G. Simplistically, this can be done by assuming that the torque is due to some local viscosity, the origin of which is unspecified (gas pressure, magnetised winds, or ?). To accomplish this, we introduce the stress tensor, T_{ij} which describes the rate at which momentum in the ith direction is carried in the jth direction by the (unknown) viscosity:

$$T_{ij} = \rho\nu \left[\frac{\partial v_i}{\partial x_j} + \frac{\partial v_j}{\partial x_i} - \frac{2}{3} (\nabla \cdot \vec{v}) \delta_{ij} \right] \tag{2.4}$$

For standard accretion disks, the only interesting component of T_{ij} is that relating the (r, ϕ)-coordinates:

$$T_{r\phi} = \rho\nu \left[\frac{\partial v_\phi}{\partial r} + \frac{v_\phi}{r} \right] = \rho\nu r \frac{\partial \Omega}{\partial r} \tag{2.5}$$

Here, ν is the viscosity. The torque between two adjacent rings is then:

$$G = \int \int r^2 T_{r\phi} d\phi dz = 2\pi r^3 \nu \Sigma \frac{\partial \Omega}{\partial r} \tag{2.6}$$

In combination with Eqn's 2.2, 2.3, this prescription for the torque allows us to write down expressions for the radial velocity, v_r (which can be instantly used to solve the continuity equation):

$$v_r = \left[\frac{\partial}{\partial r} \left(r^3 \nu \Sigma \frac{\partial \Omega}{\partial r} \right) \right] \left[r\Sigma \frac{\partial}{\partial r} \left(r^2 \Omega \right) \right]^{-1} \tag{2.7}$$

Now, for time-steady disks, we can simplify much of the above discussion to yield some important insights into the behaviour of a simple accretion disk solution. By setting the time derivatives of Eqn's. 2.2 and 2.3 to zero, we obtain:

$$\dot{M} = -2\pi r \Sigma v_r; \text{ (Mass Conservation)} \tag{2.8}$$

$$r^2 \dot{M} \Omega + C = -G; \text{ (Angular Momentum Conservation)} \tag{2.9}$$

The constant of integration, C corresponds, physically, to the angular momentum flow in the disk, which is determined by finding the radius, r_{ms}, where the stress is forced to zero. For a black hole, we expect such a radius to located at the marginally stable orbit,

r_{ms}, below which material falls ballistically into the hole (see Chapter 3). We therefore have:

$$C = -r_{ms}^2 \Omega(r_{ms}) \dot{M} \tag{2.10}$$

We can therefore write conservation of angular momentum in the form:

$$\nu\Sigma = -\frac{1}{2\pi}\frac{\dot{M}\Omega(r)}{r}\left[1 - \left(\frac{r_{ms}}{r}\right)^2 \frac{\Omega(r_{ms})}{\Omega(r)}\right]\left[\frac{\partial\Omega(r)}{\partial r}\right]^{-1} \tag{2.11}$$

Thus far, our only concession to a full relativistic treatment of the problem has been the enforcement of the stress-free boundary condition at the marginally stable orbit, r_{ms}, which we have taken as the inner edge of the disk. Novikov & Thorne (1973); Page & Thorne (1974) explicitly demonstrated that the dynamics of the disk in a fully relativistic calculation could be introduced by the inclusion of three multiplicative functions, the properties of which are discussed at length in Krolik (1999). However, we can still continue without these corrections to gain a qualitative understanding of the properties of accretion disks as predicted in the standard model. Following Frank et al. (2002), the energy dissipated into the gas (by the torque) per unit disk surface area, $D(r)$ is found by considering the work done by the net torque acting on a ring of gas, yielding:

$$D(r) = \frac{G}{4\pi r}\frac{\partial\Omega(r)}{\partial r} = \frac{\nu\Sigma}{2}\left[r\frac{\partial\Omega(r)}{\partial r}\right]^2 = -\frac{r\dot{M}\Omega(r)}{4\pi}\frac{\partial\Omega(r)}{\partial r}\left[1 - \left(\frac{r_{ms}}{r}\right)^2 \frac{\Omega(r_{ms})}{\Omega(r)}\right] \tag{2.12}$$

The luminosity emitted by a disk from $r_1 \rightarrow r_2$ is found by integrating this function over this region of the disk. For a Keplerian disk, we find that:

$$L(r) = 2\int_{r_1}^{r_2}\int_0^{2\pi} D(r) r dr d\phi = \begin{cases} \frac{3GM\dot{M}}{2}\left(\frac{1}{r_1} - \frac{1}{r_2}\right) & (r_2 > r_1 \gg r_{ms}) \\ \frac{1}{2}\frac{GM\dot{M}}{r_{ms}} & (r_1 = r_{ms}; r_2 \rightarrow \infty) \end{cases} \tag{2.13}$$

The first of these solutions, valid for regions of the disk far away from its inner edge, tells us that the radiated energy is greater than the gravitational potential energy lost by the gas in the disk. Essentially, potential energy that is released in the inner regions of the disk has been transported out with the angular momentum and is radiated at larger radii. The second of these solutions, valid for the entire disk, tells us that overall, half of the

gravitational potential energy liberated during the accretion process is radiated away by the disk, whilst the remainder is converted into kinetic energy of the gas.

If we assume that the disk is optically thick in the z-direction, then each element of the disk surface will radiate approximately as a blackbody, the temperature of which is found from the dissipation equation: (Eqn. 2.12) via:

$$T(r) \propto \sqrt[4]{D(r)} \tag{2.14}$$

Ignoring relativistic corrections (to both the dynamics of the disk and the propagation of photons to the observer), the spectrum of the disk can therefore be approximated by:

$$F_\nu = \frac{4\pi h \cos i \nu^3}{c^2 D^2} \int_{r_{in}}^{r_{out}} \frac{r dr}{exp[h\nu/kT(r)] - 1} \tag{2.15}$$

Importantly, F_ν is independent of viscosity, implying that observed deviations of the accretion disk spectrum from a blackbody cannot be due to the viscosity mechanism - rather they will due to our assumptions regarding the vertical structure of the disk and lack of relativistic corrections to both the disk structure equations and the propagation of photons. This prediction, however, matches well to the observed properties of accreting black holes, where we observe a blackbody component in the soft X-rays for BHBs and in the UV for AGN.

The standard accretion disk model therefore provides us with something that at least approximates the cool accretion disk seen in the soft states of BHBs. How then can we explain the hot inner flow observed in the low-luminosity, hard X-ray dominated states of these systems? Qualitatively, at low luminosities, the mass accretion rate through the disk is reduced, which implies a corresponding decrease in the surface mass density, Σ. Below a certain level, there is no longer enough mass contained within an annulus of the disk for it to be accurately described as optically thick in the z-direction. The disk is therefore no longer able to radiate as a blackbody, which requires that, for an equal amount of heat to be dissipated at a given radius, the temperature of the material must rise. This in turn causes the mass density to decrease (as the material now has more

thermal energy) and the disk evaporates, leaving us with a geometrically thick, optically thin accretion flow (Różańska & Czerny, 2000). If heat is dissipated in the protons, then the low mass densities imply that it may be difficult for the flow to efficiently transfer the heat to the electrons, which is necessary for the efficient conversion of heat to radiation. If this is the case, then the heat may well be advected (along with the protons) into the black hole, instead of being radiated away, known as an Advection Dominated Accretion Flow (ADAFs, for an in depth discussion see e.g. Frank et al., 2002).

We are now in possession of a simple description of the accretion flow, which appears to match (at least some of) the observed properties. What then provides the viscosity driving the outward transport of angular momentum in the accretion disk? Shakura & Sunyaev (1973) noted that the natural scale for *any* hydrodynamic stress is the (gas) pressure, p and therefore proposed that the viscosity should be proportional to this $\nu \propto p$, which implies an effective viscosity $\nu \sim \alpha c_s h$ (see e.g Frank et al., 2002). This α-model, as this prescription has become known, takes all of our ignorance and wraps it up into α. Unfortunately, this approach is rather unsuccessful. The *only* physical mechanism that seems capable of generating angular momentum transport out through the disk is the Magneto-Rotational Instability that was rediscovered by Balbus & Hawley (1991) and originally described by Velikhov (1959); Chandrasekhar (1961). The essential idea behind this instability is that a radial perturbation of an initially poloidal magnetic field is unstable, with the growth rate $\lesssim$ the orbital frequency. This instability is rather different from the α-model as the free energy arises from the shear between adjacent rings of gas, but different radii within the disk are coupled by the magnetic field - hence the instability is fundamentally non-viscous in nature (as opposed to the α-model).

So what of the α-model? Are we to consign it to the 'dustbin of history', despite its successes in explaining the observed spectra? Leaving aside the problems of the viscosity mechanism, does the α-model give a good description of the possible form of an accretion disk? The answer to this question lies in the stability of the α-model solution of the thin

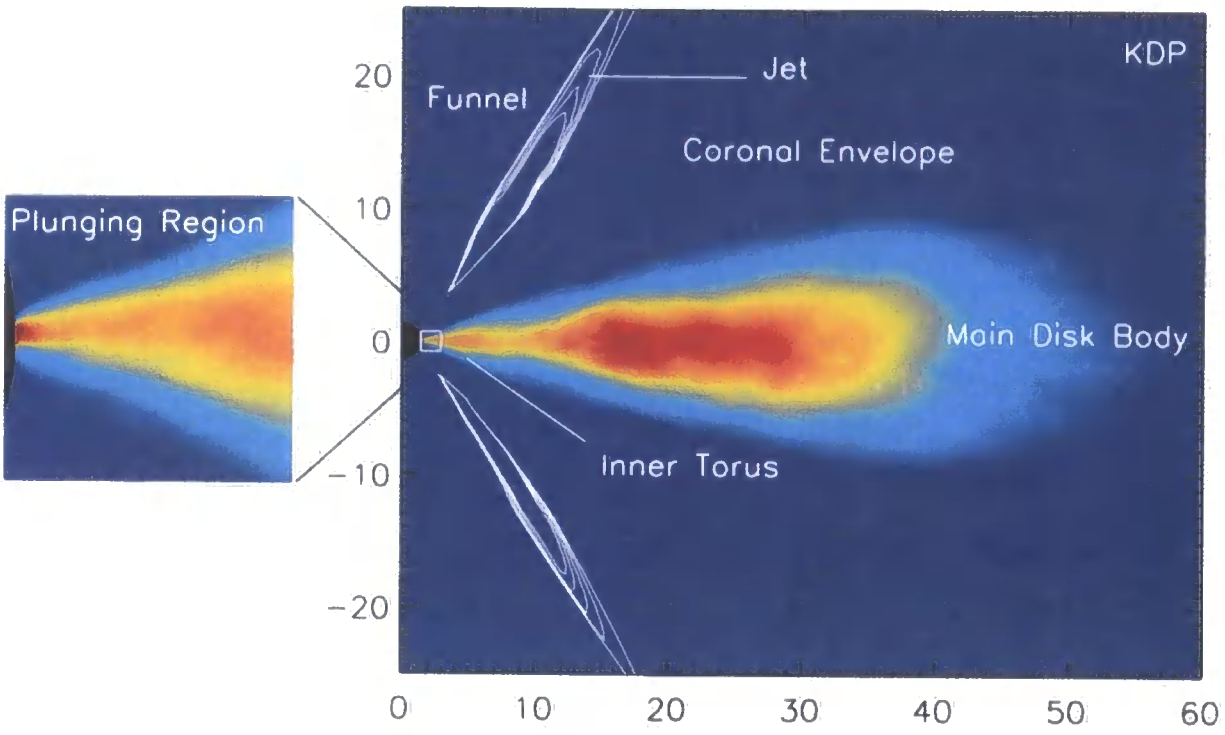

Figure 2.7: Results of non-radiative, global, general relativistic MHD accretion flow simulations performed by De Villiers et al. (2003). Shown here are the generic structures in the azimuthally averaged gas density, along with contours of positive radial momentum and a close-up view of the plunging region. Taken from De Villiers et al. (2003).

disk equations. When these are analysed in the radiation pressure dominated regime, then the disks are both thermally and viscously unstable. Even worse, this is the type of solution which we would expect to see in the inner regions of the accretion disk, where the majority of energy is liberated from the flow. These instabilities lead the standard disk model to predict limit-cycle variability for disk-dominated states in BHBs - however, long-term observations of these states in various sources demonstrate that they are rather stable (Gierliński & Done, 2004). Combined with the problems of the viscosity mechanism, this leaves the α-model in serious difficulties, the resolution of which is (currently) entirely open.

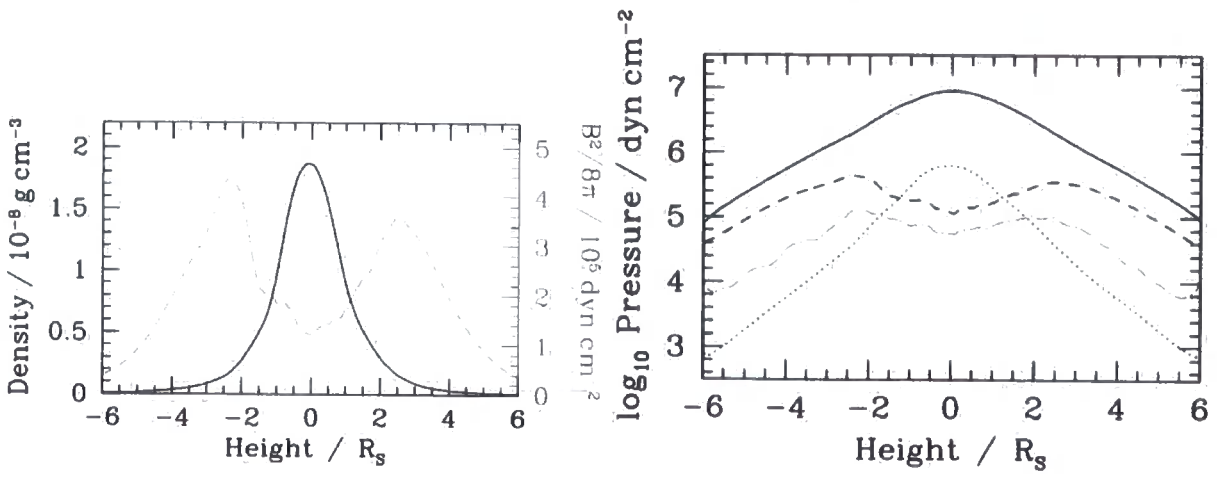

Figure 2.8: Results of three-dimensional radiation-MHD stratified shearing-box simulations of a small patch of disk located $200GMc^{-2}$ away from a $10^8 M_\odot$ black hole. The left-hand panel shows time-averaged, horizontally-averaged distribution of density (solid line, left scale) and magnetic pressure (dashed, right scale) as a function of height. The right-hand panel shown radiation pressure (solid line), gas pressure (dotted line), magnetic pressure (dashed line) and total accretion stress (dot-dashed line). Taken from Turner (2004).

If angular momentum transport is indeed provided by the alternative to the α-model, the Magnetic-Resonance Instability (MRI), then the resulting accretion flows are rather more complex. Excellent reviews of the basic physics that comprises these Magneto-Hydrodynamics (MHD) studies can be found in Balbus & Hawley (1998); Blaes (2004); Armitage (2004) - our interest lies in how the properties of these flows can enhance our understanding of accretion onto black holes. Numerical simulations of this mechanism generically demonstrate that, in the absence of radiative cooling, the flow takes the form of a geometrically thick structure, qualitatively similar to that described by the advection dominated case (see Figure 2.7). The flows are, however, highly turbulent and also posses evidence for relativistic outflows, which, in the fully General Relativistic case, exhibit

a strong dependence on black hole spin (see e.g. De Villiers et al., 2005). Inclusion of radiative cooling into these simulations complicates the picture enormously, due to the presence of three instabilities (convection, Shaviv modes and photon bubbles) which can lead to vertical energy transport by the MRI (Turner et al., 2005). Current state-of-the-art studies are limited to the investigation of small patches of disk around $\sim 40GM/c^2$ from the central black hole, where gravity can be taken to be approximately Newtonian. Generically, these studies seem to predict disks that are qualitatively similar to the standard case, with the bulk of the magnetic pressure (which is thought to trace dissipation Rosner et al., 1978, see Chapter 6) concentrated external to the main disk body, as shown in Figure 2.8. As an aside, we note that Figure 2.8 illustrates that the accretion stress approximately traces the magnetic pressure, rather than the gas or radiation pressure, in distinct contrast to the α-model. Returning to the initial thrust of our discussion, it fortunately, therefore, it appears likely that accretion disks in the MHD approximation are still able to provide a two-phase description of the accretion flow, which appears to correspond well to the geometry's observed in both BHBs and AGN. Interestingly, these studies also give us a quantitative insight into how relativistic jets may be formed in these systems and how these jets are related to the properties of both the accretion flow and the central black hole (for recent reviews see, e.g. Begelman, 2001; Blandford, 2002; Meier, 2003).

2.5 Testing Strong Gravity

The obvious way to test both the models of the accretion flow and the predictions of General Relativity is by direct comparison of their predictions to the observed spectral properties of accreting black holes. In Newtonian physics, such a calculation is straightforward. Light travels in straight lines, unaffected by the gravitational potential and so one can analytically relate the observed and emitted spectral properties of the accretion flow. In a fully General Relativistic calculation, light no longer travels in straight lines,

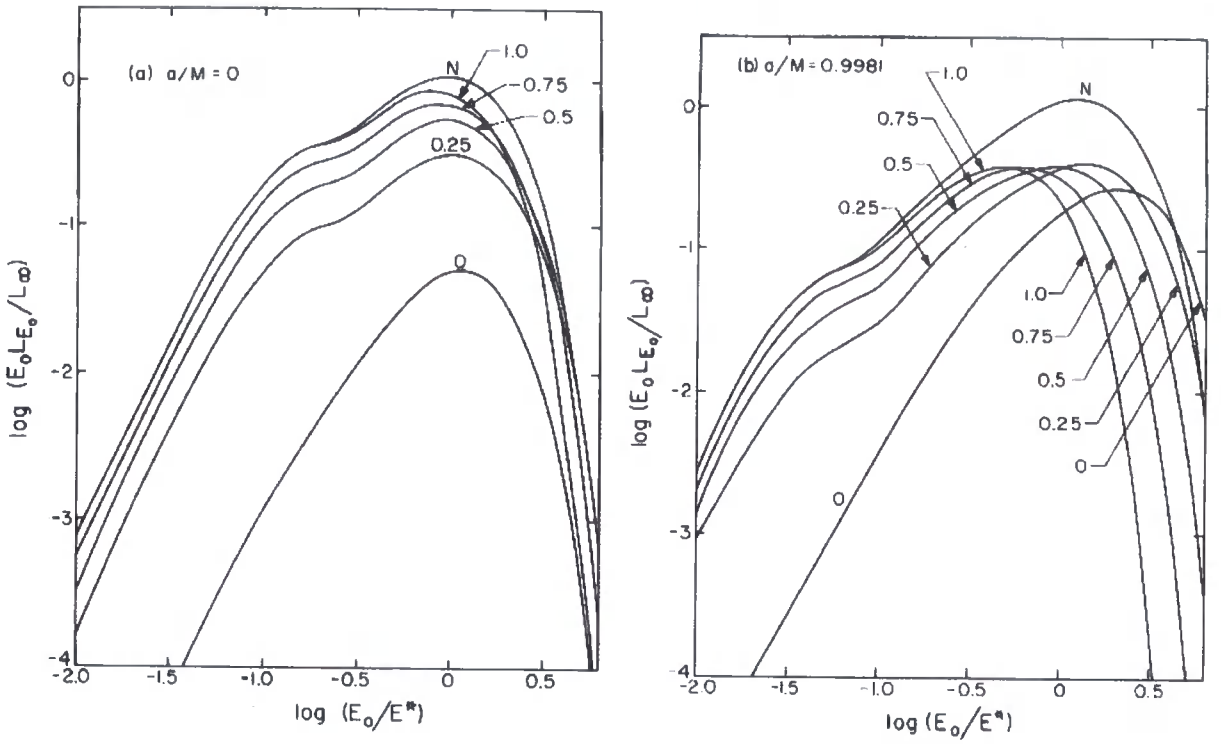

Figure 2.9: "The spectrum of a disk which radiates like a blackbody. Curves are labelled by the values of $\cos\theta_O$. ('N' is a Newtonian for the axial observer, evaluated neglecting effects of redshift and focusing...). Separate graphs for the two values of a/M are given... Note the sensitive dependence of the peak of the spectrum on the observer's polar angle. The low energy feature in the spectrum (which is due to the temperature distribution in the disk, not to focusing or redshifts) is very much attenuated for observers near the plane". Taken from Cunningham (1975)

which rather complicates the issue as the calculation is no longer analytic.

The first attempt to calculate the observed spectra of accretion disks around black holes in full General Relativity was undertaken by Cunningham (1975), who determined the shape of the observed spectrum by convolution of the intrinsic disk spectrum from the standard accretion disk model with a transfer function that encapsulated photon propagation in the Kerr metric (i.e. the effects of gravitational redshift, light-bending,

etc.) along with those due to the dynamics of the disk (Doppler shift, length-contraction, etc.). The resulting spectra are shown in Figure 2.9, along with the intrinsic disk spectrum for comparison. The differences between the predicted spectra for different black hole spins at constant inclination are clearly rather small. Attempts to determine the form of the gravitational potential using this broad spectral feature (see e.g. Laor & Netzer, 1989; Ebisawa et al., 1991, 1993; Makishima et al., 2000; Gierliński et al., 2001; Li et al., 2005) not only suffer from the problems of attempting to distinguish between similar broad spectral components, but also from our limited knowledge of the shape of the intrinsic disk spectrum.

From an observational point of view, it is far easier to examine relativistic effects on an intrinsically narrow spectral feature, such as the Iron Kα fluorescence feature expected to be present when the cold accretion disk is illuminated by hard X-ray photons. Fabian et al. (1989) first examined the influence of both gravitational and dynamical effects on this intrinsically narrow line, finding that they resulted in a characteristic broad, double-peaked, skewed profile (see Figure 2.10). Laor et al. (1990); Laor (1991) extended these results to the case of maximally rotating black holes, fully including the effects of light-bending. Further work continued apace, Chen & Halpern (1990) examined the polarisation properties of broad optical emission lines; Matt et al. (1991) extended the earlier results to different disk geometries and illumination patterns; Matt et al. (1993b) demonstrated the formation of substructure in the line, due to gravitational lensing effects, for flat accretion disks viewed at high inclinations around Schwarzschild black holes (see Chapter 4); Matt et al. (1993a) examined the line shapes produced by photo-ionised accretion disks; Bao et al. (1994) determined the contribution of multiple-orbit photons to line formation for a Schwarzschild black hole (see Chapter 5); Viergutz (1993) described how photon trajectories could be quickly integrated for general emission geometries (see Chapter 3); Karas et al. (1995) calculated line profiles associated with a self-gravitating disk; Fanton et al. (1997) gave an insightful description of how photon trajectories may be

quickly integrated for flat disks to determine line shapes; Martocchia et al. (2000) (drawing on previous work) gave a full relativistic treatment of illumination of the disk by a central source (the 'lamppost model'[5], see Chapter 6); Agol & Krolik (2000) performed detailed calculations of the effect of relaxing the stress-free inner boundary condition on both the intrinsic disk spectrum and the shape of the line profile, which was extended by Li et al. (2005), who included the effects of returning radiation. Finally, Dovčiak et al. (2004) have outlined an extended scheme for use within the XSPEC spectral fitting package (Arnaud, 1996) which enables the rapid analysis of fluorescent Iron Kα profiles in strong gravity.

Observational evidence for broad Iron Kα lines first came from the Seyfert 1 galaxy, MCG-6-30-15, which was the first Active Galactic Nucleus to exhibit X-ray reflection from predominantly neutral material (Nandra et al., 1989; Pounds et al., 1990). Subsequent studies of this object, driven by Yasuo Tanaka and Andy Fabian using the joint Japanese / American *Advanced Satellite for Cosmology and Astrophysics* (*ASCA*), revealed a significantly broadened Iron Kα line. As described by Tanaka et al. (1995), this feature could be well described by line emission from an accretion disk around a Schwarzschild black hole, viewed at an inclination of $\theta \approx 30°$, with the accretion disk extending down to the marginally stable orbit (which, for a Schwarzschild black hole, is located at $6r_g$).

The ASCA observations of MCG-6-30-15 revealed the line emission to be highly variable, associated with flaring events in the innermost regions of the accretion disk (see Figure 2.11). In one particular set of observations (the 1994 Deep Minimum state, Iwasawa et al., 1996), the broadening of the line was so significant as to exceed that allowed by the standard accretion disk model around a Schwarzschild black hole. Explanation of such extreme broadening requires the invocation of a disk extending deeper into the gravitational potential than allowed by the marginally stable orbit associated with a Schwarzschild black hole. Such an invocation can be accomplished in one of two ways, either the black hole rotates such that the marginally stable orbit moves deeper into the

[5]it should be noted, however, that the physical motivation for this model remains unclear and it is hard to reconcile the illumination geometry with the assumed dynamical properties of the accretion disk

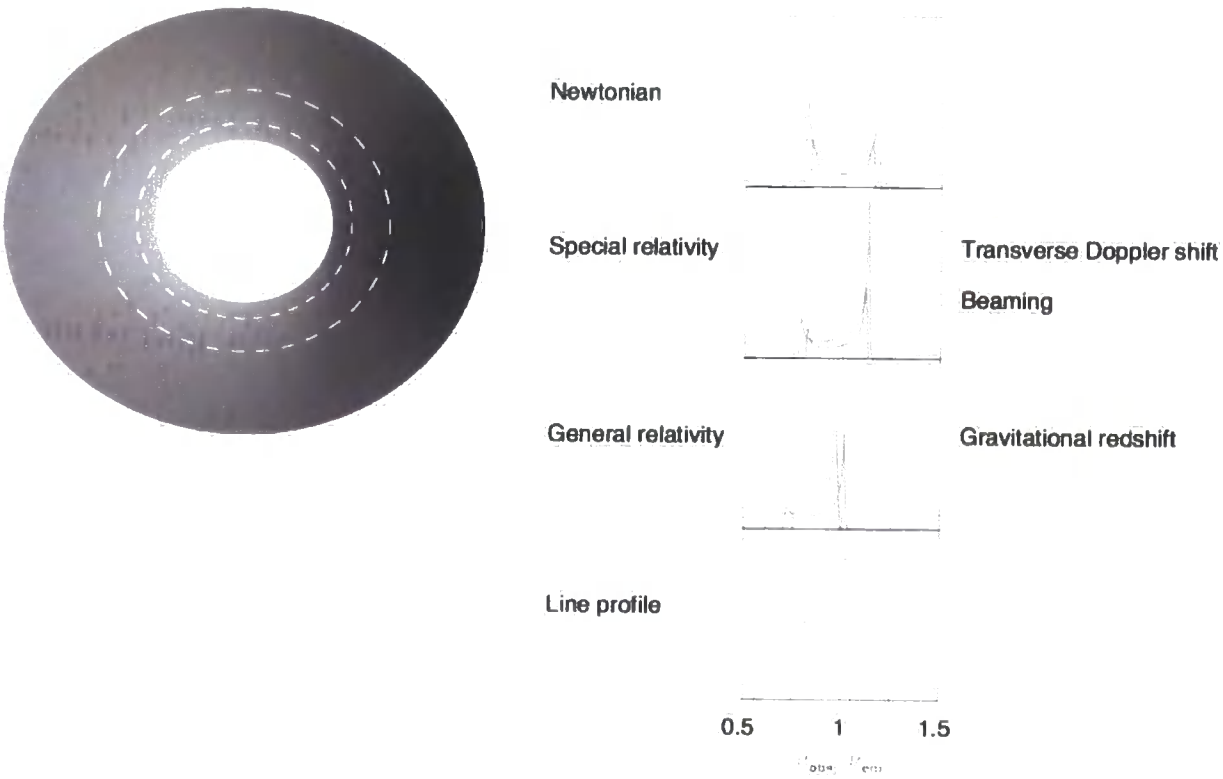

Figure 2.10: "The profiles of the broad iron line is caused by the interplay of Doppler and transverse Doppler shifts, relativistic beaming and gravitational redshift. The upper panel shows the symmetric double-peaked profiles from two narrow annuli on a nonrelativsitc disk. In the second panel the effects of transverse Doppler shifting and relativistic beaming have been included, and in the third panel gravitational redshifting has been included. These give rise to a broad, skewed profile, such as that shown in the lower panel." Taken from Fabian et al. (2000)

gravitational potential, or line fluorescence takes place below the marginally stable orbit (Reynolds & Begelman, 1997). In the former scenario, the observed Iron Kα width allows us to infer the rotation ('spin') of the central black hole through the assumption of the stress-free inner boundary condition in the standard accretion disk model. However, in the latter scenario, it is possible to produce arbitrarily broad emission lines, independent of black hole spin. Whilst the scenarios for line production in this circumstance are somewhat more contrived (requiring the formation of a powerful X-ray emitting corona in the plunging region), it is currently not possible to rule them out theoretically.

Serendipitously, the first observation of MCG-6-30-15 by the European Space Agency observatory *XMM-Newton* coincided with a re-occurrence of the Deep Minimum state first seen in the 1994 *ASCA* observation. Again, this particular state of MCG-6-30-15 appears to be associated with a robust, highly broadened Iron Kα line (see Figure 2.12, Wilms et al., 2001; Vaughan & Fabian, 2004; Reynolds et al., 2004). Detailed modelling of the line using the more sensitive detectors available on *XMM-Newton* reveals it to be associated with a rapidly rotating black hole (assuming the stress-free inner boundary condition), with a large amount of the fluorescence being generated in the very inner regions of the accretion disk. In the alternative scenario, where line fluorescence is produced within the plunging region associated with a Schwarzschild black hole, then the inner radius lies below $3r_g$, with virtually all of the emission being produced between this radius and the event horizon, which seems unlikely. In fact, if we assume that the illumination pattern generating Iron Kα fluorescence traces the underlying dissipation in the disk (i.e illumination by a hot corona, as opposed to by a lamppost, Martocchia et al., 2000), then the concentration of fluorescence towards the inner regions of the disk is somewhat larger than predicted by the standard accretion disk model, even for a rapidly rotating black hole. This can be accomplished if the accretion disk is able to extract energy from the black hole itself, possibly by explicit violation of the stress-free inner boundary condition, as outlined by Agol & Krolik (2000). This rather surprising result appears robust (Reynolds

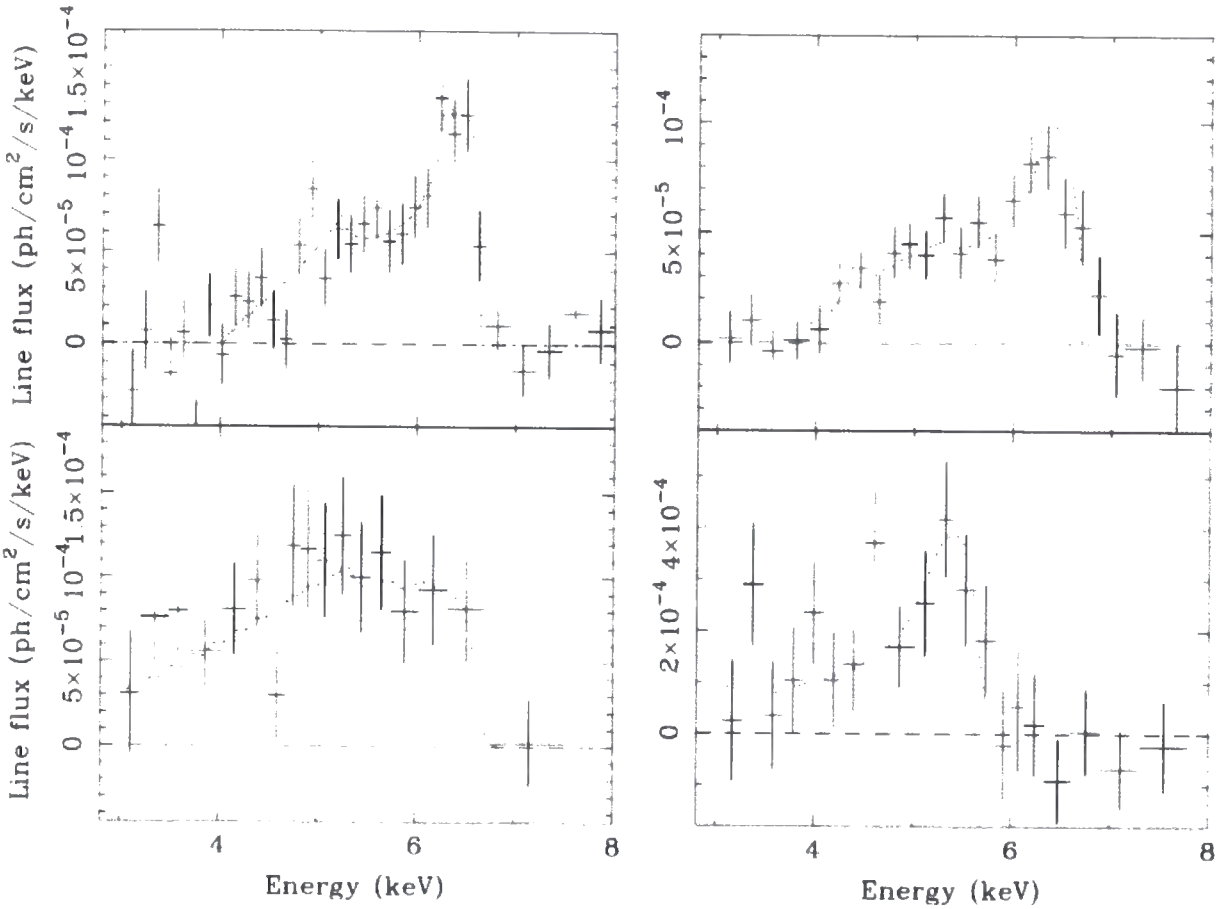

Figure 2.11: "Time-averaged (upper panels) and peculiar line profiles (lower panels) of the iron K emission from MCG6-30-15 seen in the two long ASCA observations in 1994 (left) and 1997 (right). In the 1994 observation, a very broad profile with a pronounced red-wing is seen during a period of Deep Minimum of the light curve (lower left), compared to the time-averaged line profile shown in the upper panel. In contrast, during a sharp flare in the 1997 observation, whole line emission is shifted to energies below 6 keV and there is no significant emission at the rest line-energy of 6:4 keV (lower right). Both peculiar line shapes can be explained by large gravitational redshift in small radii on the accretion disk." Taken from Reynolds & Nowak (2003)

et al., 2004), but remains a rather controversial topic within the community.

Fortunately, MCG-6-30-15 is not the only source that exhibits a broad spectral feature in the $2 - 10keV$ band. Approximately half of the known moderate-to-high luminosity AGN exhibit an Iron Kα line that has been broadened to some extent (see e.g. Nandra et al., 1997). Caution is necessary however, as seemingly broad lines can results from complex absorption (see, for example Schurch & Warwick, 2002; Schurch et al., 2003). By contrast, the widths of iron lines exhibited by BHBs seem correlated with spectra state (see e.g. Gilfanov et al., 2000). However, recent work by Miller et al. (2004) seems to indicate the existence of lines with widths comparable to that observed in MCG-6-30-15 in several sources. The robustness of these claims is untested however and their validity remains a source of intense controversy within the community.

High resolution spectroscopy of broad iron lines allows us test our understanding of both accretion and the underlying properties of the gravitational field. However, as we shall see in the remainder of this work, precision tests of strong gravity using these line profiles *relies* on our understanding of the (as yet unknown) properties of the accretion flow. We are not solely reliant on broad iron lines, however. In recent years, high resolution timing information available from the *Rossi X-Ray Timing Explorer* (*RXTE*) along with *GINGA* and *EXOSAT* has lead to the discovery of Quasi-Periodic Oscillations (QPOs) in the power spectra of many low mass accreting compact objects. In several BHBs, the QPOs occur in pairs related by small, well-defined, integer ratios ($3:2$, $5:3$, Strohmayer, 2001a,b; Abramowicz & Kluźniak, 2001), which has lead many authors to suggest that they originate from the coupling of the accretion flow to the gravitational potential (see e.g. Titarchuk et al., 1998; Stella et al., 1999; Psaltis & Norman, 2000). This yields the intriguing possibility of probing the black hole spacetime via the temporal variability of the source. However, the precise nature of this coupling is, as yet, not widely understood, limiting the current usefulness of this approach. In many other systems, the QPO frequency is variable, which is either attributed to a characteristic radius within

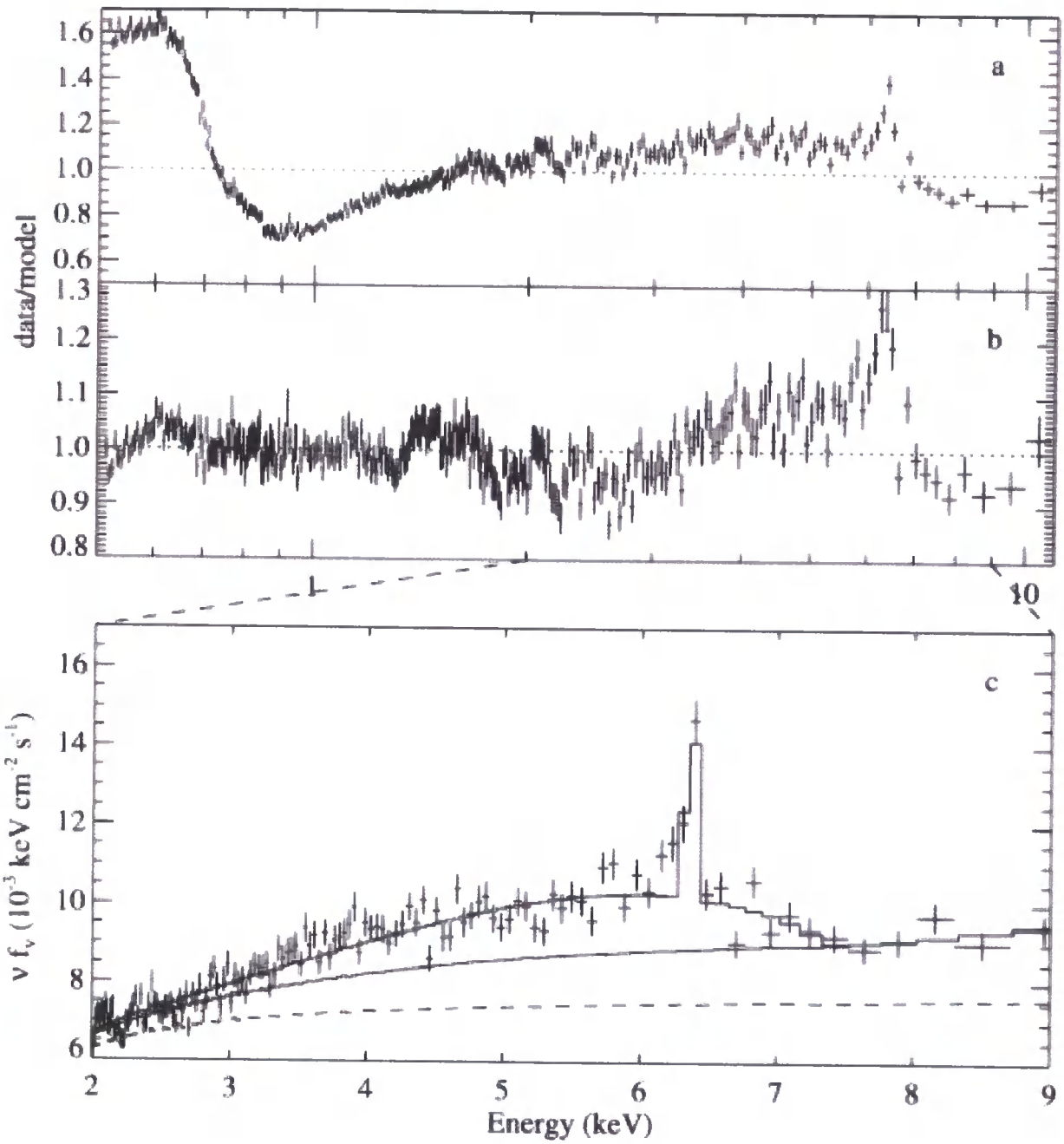

Figure 2.12: Results of the July 2000 XMM-Newton Observation of MCG-6-30-15 in the Deep Minimum State"(a) Ratio between data and model from fitting a power law to the data. (b) Ratio from fitting a power law and the empirical warm absorber model... (c) Deconvolved spectrum of the Fe K band, showing the total `laor` model and the continuum with and without (dashed) the reflection component for a model with reflection from an ionized disk. For clarity, the data have been rebinned and only the single-event data points are shown" Taken from Wilms et al. (2001)

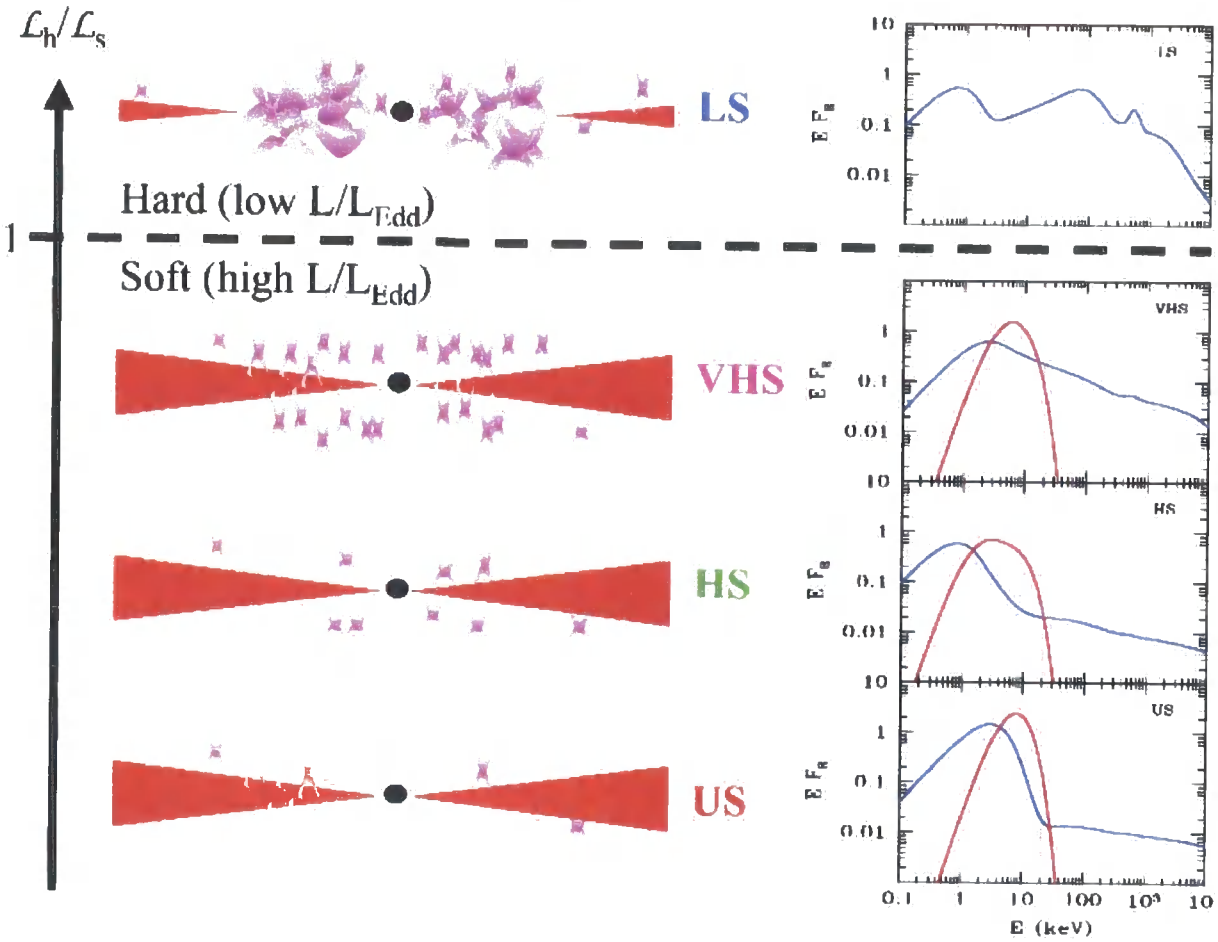

Figure 2.13: As in Figure 2.3 for BHBs and Neutron Stars in atoll sources. "At high L/L_{Edd} the identical accretion flow in atoll systems has an additional component from an optically thick boundary layer (red)." Taken from Done & Gierliński (2004).

the accretion flow for BHBs, or coupling to the stellar spin in the case of Neutron stars. Again, if these mechanism can be reliably identified, then QPOs will be able provide a remarkable insight into strong gravity.

More promising, however, is the idea of testing the existence of the event horizon. Alternatives to black holes with an event horizon (and hence no surface) are exotic compact stars, where the stellar surface is located just above the black hole event horizon.

The effect of material accreting onto this surface should be readily observable, despite its high-redshift. Firstly, Narayan & Heyl (2002) propose that if material were accreted onto such a surface, then eventually the density and temperature on the surface will increase to such a level that a Type 1 thermonuclear explosion would be inevitable, as is observed in systems containing Neutron Stars. Remarkably, no BHB has ever exhibited such behaviour, leading credence to the existence of the event horizon in these systems. Narayan et al. (1997) take this argument a stage further by the examination of the spectra of a selection of BHBs in quiescence. Quiescent accreting neutron stars tend to exhibit soft thermal emission from the stellar surface, which implies that a similar result should be found if black holes did posses a surface (where the heating mechanism would be either through deep crustal heating or accretion). Such emission is absent from the BHBs, indicating the absence of a stellar surface, the natural explanation of which is that the compact object possesses an event horizon (i.e. is a black hole). McClintock et al. (2004) examine a particularly suitable BHB, XTEJ1118+480 (due to lack of absorption along the line-of-sight), again in quiescence, again finding such a spectral component is absent, seemingly confirming (for XTEJ1118+480 at least) that black holes do indeed have event horizons. Finally, Done & Gierliński (2003) examine the spectra of both BHBs and accreting Neutron Stars when the sources are *bright*. Both types of sources can be explained in the context of the same spectral model, the difference being the presence of an additional component for the Neutron Stars, which is attributed to the presence of a surface / boundary layer (see Figure 2.13). The absence of such a component in the BHB spectra lends yet further support to the existence of the black hole event horizon.

Chapter 3

Mathematical Properties of Strong Gravitational Fields

Abstract

We introduce the relevant mathematical formalism for computing spectra in the strong gravitational field of rotating black holes. The properties of the spacetime of such a black hole are introduced, including the event horizon and ergosphere. The equations of geodesic motion for both time-like and null geodesics are derived through the explicit separation of the Hamilton-Jacobi equation. The null geodesic equations are reformulated to enable the fast computation of photon trajectories. The properties of the effective potentials governing these trajectories are discussed and it is demonstrated how these properties may be used to more effectively accomplish the calculation of the photon trajectories. The importance of multiple orbit photons to the observed properties of accretion flows is highlighted The tetrad formalism used to evaluate physical quantities in the rest frame of arbitrarily moving observers is introduced and several important physical quantities evaluated. Finally, we describe how we calculate spectra of optically thick, geometrically thin accretion disks.

3.1 The Spacetime of the Rotating Black Hole

Many stellar objects that are likely to undergo gravitational collapse to form black holes (i.e massive stars, neutron stars, etc.) possess some amount of angular momentum before collapse. It therefore seems likely that the black hole that remains after collapse must be in possession of some angular momentum. Complete studies of physical processes in strong gravitational fields must therefore consider the case of the rotating black hole, despite the complexities that this introduces into the calculations. In Section 2.5, we saw that there is increasing evidence that some Black Hole Candidate objects may be in possession of spin parameters as high as $a = 0.998$, so there is a clear astrophysical need to consider rotating black holes[1].

By contrast, it is almost certain that no astrophysical black hole can possess any significant amount of charge. Misner et al. (1973) provide a simple, concise argument for this, which we reproduce for completeness. Any Black Hole Candidate that had significant charge would exert attractive electrostatic forces on electrons and repulsive electrostatic forces on protons in the surrounding Interstellar Medium or Accretion Flow. The ratio between these forces and the gravitational force of the black would be $\approx 10^{20}$. It is therefore apparent that any net charge of the black hole will be rapidly neutralised and so any astrophysically realisable black hole can be considered to be uncharged. We can therefore characterise the source with the parameters:

$$M = \text{ Mass; } \quad a \equiv \frac{J}{M} = \text{ Angular Momentum per unit Mass;}$$

With this choice of parameters, the most general solution of the Einstein Field Equations describing a rotating black hole is given by the Kerr family of solutions (Chandrasekhar, 1983). Written in Boyer-Lindquist co-ordinates, using gravitational units

[1]In fact, Thorne (1974), working in the context of the standard accretion disk model, showed that $a = 0.998$ is the maximum obtainable black hole spin when one includes the effect torque exerted by captured photons on the evolution of the hole

$(G = M = c = 1)$, the line element takes the form:

$$ds^2 = e^{2\nu}dt^2 - e^{2\psi}\left(d\phi - \omega dt\right)^2 - e^{2\mu_2}dr^2 - e^{2\mu_3}d\theta^2 \tag{3.1}$$

Here, we have defined the metric functions:

$$e^{2\nu} = \frac{\rho^2\Delta}{\Sigma^2};\ \ e^{2\psi} = \frac{\Sigma^2\sin^2\theta}{\rho^2};\ \ e^{2\mu_2} = \frac{\rho^2}{\Delta};\ \ e^{2\mu_3} = \rho^2 \tag{3.2}$$

Finally, we have that:

$$\Delta = r^2 - 2r + a^2;\ \ \rho^2 = r^2 + a^2cos^2\theta;\ \ \Sigma^2 = \left(r^2 + a^2\right)^2 - a^2\Delta\sin^2\theta \tag{3.3}$$

The line element (Eqn. 3.1) is independent of both the t and ϕ coordinates and hence the metric is both stationary and axisymmetric. Note that, if we set $a = 0$ in the above equations, then our line element reduces to the Schwarzschild solution describing the external gravitational field of a non-rotating compact object, i.e.

$$ds^2 = \left(1 - \frac{2}{r}\right)dt^2 - \left(1 - \frac{2}{r}\right)^{-1}dr^2 - r^2\left(d\theta^2 + \sin^2\theta d\phi^2\right) \tag{3.4}$$

We shall now summarise some of the key results related to the line element (Eqn. 3.1) that will be relevant for future discussions, based on the concise account given by Bardeen et al. (1972). We begin with the observation that the event horizon ('one-way membrane') associated with the line element (Eqn. 3.1) is defined by the outer root of $\Delta(r) = 0$:

$$r_h = r_+ = 1 + \sqrt{1 - a^2} \tag{3.5}$$

This takes its familiar value of $r_h = 2r_g$ in the non-rotating (Schwarzschild) case (Eqn. 3.4). Note that r_+ is also a coordinate singularity, in that the radial component of the line element (Eqn. 3.1) is singular here, whilst we can change coordinate system and find trajectories that cross r_+ in an inwards direction (the converse not being possible). It is also important to note that, in general, the location of the null surface describing the event horizon does not coincide with the surface described by $g_{tt} = 0$, which is described by:

$$r_e(\theta) = 1 + \sqrt{1 - a^2\cos^2\theta} \tag{3.6}$$

Clearly, we have that $r_e(\theta) \geq r_h$ for all a. This stationary surface is knows as the 'static limit', with the region $r_h < r \leq r_e(\theta)$ known as the ergosphere. Within this region, all observers with fixed (r, θ) must rotate in the same direction as the black hole (the positive ϕ-direction). Observers within this region are able to access the negative energy orbits that extract energy from the black hole (see below).

The motion of geodesics in the Kerr geometry is completely described by three non-trivial constants of motion, which in Boyer-Lindquist co-ordinates are identified as the total energy, E; the component of the angular momentum parallel to the symmetry axis, L_z and Carters constant, Q, where (see Section 3.2.1):

$$Q = p_\theta^2 + \cos^2\theta \left[a^2 \left(\mu^2 - p_t^2 \right) + \frac{p_\phi^2}{\sin^2\theta} \right] \tag{3.7}$$

A fourth, trivial constant is the rest mass of the particle, μ. Note that $Q = 0$ is both a necessary and sufficient condition for motion initially in the equatorial plane to remain there for all subsequent times, whilst orbits crossing the equatorial plane must necessarily have $Q > 0$.

The four-momentum of a test particle can be obtained through solution of the above equation, recalling that $p^\mu \equiv dx^\mu/d\lambda$, where λ is related to proper time by $\lambda = \tau/\mu$, which is an affine parameter in the limit $\mu \to 0$. It is found that:

$$\begin{aligned} \Sigma \frac{dr}{d\lambda} &= \pm\sqrt{V_r}; \quad \Sigma \frac{d\theta}{d\lambda} = \pm\sqrt{V_\theta}; \\ \Sigma \frac{d\phi}{d\lambda} &= -\left(aE - \frac{L_z}{\sin^2\theta} \right) + \frac{aT}{\Delta}; \\ \Sigma \frac{dt}{d\lambda} &= -a\left(aE\sin^2\theta - L_z \right) + \frac{\left(r^2 + a^2\right) T}{\Delta}; \end{aligned} \tag{3.8}$$

Here, V_r, V_θ are effective potentials (see Sections 3.2.1, 3.2.2, 3.2.3):

$$\begin{aligned} T &\equiv E\left(r^2 + a^2\right) - L_z a; \\ V_r &\equiv T^2 - \Delta\left[\mu^2 r^2 + \left(L_z - aE\right)^2 + Q\right]; \\ V_\theta &\equiv Q - \cos^2\theta \left[a^2\left(\mu^2 - E^2\right) + \frac{L_z^2}{\sin^2\theta} \right]; \end{aligned} \tag{3.9}$$

Our interests lie in the study of optically thick accretion disks around Kerr black holes. In the standard accretion disk model (Page & Thorne, 1974, see Section 2.4), gas in the disk lies on circular orbits in the equatorial plane of the black hole spacetime. For a circular orbit of constant radius, r_0, we require that $dr/d\lambda$ must vanish both instantaneously and at all subsequent times (that is, the orbit exists at a perpetual turning point). We therefore have the conditions:

$$V_r(r_0) = 0; \quad \frac{dV_r(r_0)}{dr} = 0 \tag{3.10}$$

These two equations can be solved to yield conditions on E, L_z for the circular orbit, specifically:

$$\begin{aligned} \frac{E}{\mu} &= \frac{r^{3/2} - 2r^{1/2} \pm a}{r^{3/4}\sqrt{r^{3/2} - 3r^{1/2} \pm 2a}}; \\ \frac{L_z}{\mu} &= \frac{\pm\left(r^2 \mp 2ar^{1/2} + a^2\right)}{r^{3/4}\sqrt{r^{3/2} - 3r^{1/2} \pm 2a}}; \end{aligned} \tag{3.11}$$

Here (and throughout what follows), prograde and retrograde orbits are denoted by the upper and lower signs of $\pm$ and $\mp$, respectively. The (coordinate) angular velocity of circular orbits can be obtained by combination of Eqn. 3.11 with the latter two equations of Eqn. 3.8. We find:

$$v^\phi = \frac{d\phi}{dt} = \frac{1}{a \pm r^{3/2}} \tag{3.12}$$

Clearly, for circular orbits to be possible at a given radii, the denominator of Eqn's. 3.10 must be real, which is true only if:

$$r^{3/2} - 3r^{1/2} \pm 2a \geq 0 \tag{3.13}$$

The root of this equation, $r_{\rm ph}$, describes an orbit with infinite energy per unit rest mass, which corresponds physically to a photon orbit. Such an orbit is the innermost circular orbit for all particles for a given black hole spin. We find that:

$$r_{\rm ph} = 2 + 2\cos\left[\frac{2}{3}\cos^{-1}\left(\mp a\right)\right] \tag{3.14}$$

There are two key properties of the circular orbits for $r > r_{\rm ph}$. Firstly, not all of the circular orbits in this region are bound, i.e. they posses $E/\mu \geq 1$. If we subject a particle on such an orbit to an (infinitesimal) outward perturbation, then the particle will escape to infinity. The marginally bound radius, $r_{\rm mb}$ is found by considering the limiting case $E/\mu \geq 1$:

$$r_{\rm mb} = 2 \mp a + 2\sqrt{1 \mp a} \tag{3.15}$$

Bound circular orbits exist for $r > r_{\rm mb}$. This radius also represents the minimum perihelion of all parabolic orbits (that is orbits with $E/\mu = 1$). Parabolic orbits that fall within $r_{\rm mb}$ are necessarily captured by hole. This is important from an astrophysical perspective as particle infall from infinity can be described by a very nearly parabolic trajectory.

Not all of the bound circular orbits in the equatorial plane are stable. For such an orbit to be regarded as stable, we must have that:

$$\frac{d^2 V_r(r_0)}{dr^2} = 0 \tag{3.16}$$

Applying this condition to the relevant part of Eqn. 3.9, it is found that stable orbits must satisfy:

$$r^2 - 6r \pm 8ar^{1/2} - 3a^2 \geq 0 \tag{3.17}$$

We denote the root of this equation as the marginally stable orbit, $r_{\rm ms}$, which takes the form:

$$\begin{aligned} r_{\rm ms} &= 3 + Z_2 \mp \sqrt{(3 - Z_1)\,(3 + Z_1 + 2Z_2)}; \\ Z_1 &\equiv 1 + \sqrt{1 + a^2}\left(\sqrt[3]{1 + a} + \sqrt[3]{1 - a}\right); \\ Z_2 &\equiv \sqrt{3a^2 + Z_1^2} \end{aligned} \tag{3.18}$$

We show the behaviour of $r_+(a)$, $r_0(a)$ (evaluated in the equatorial plane), $r_{\rm ph}(a)$, $r_{\rm mb}(a)$ and $r_{\rm mb}(a)$ in Figure 3.1. In the case of the extreme Kerr black hole ($a = 1$), we find that all of these radii are equal, implying that the ergosphere along with the photon, marginally bound and marginally stable orbits intersect the horizon here. This is clearly

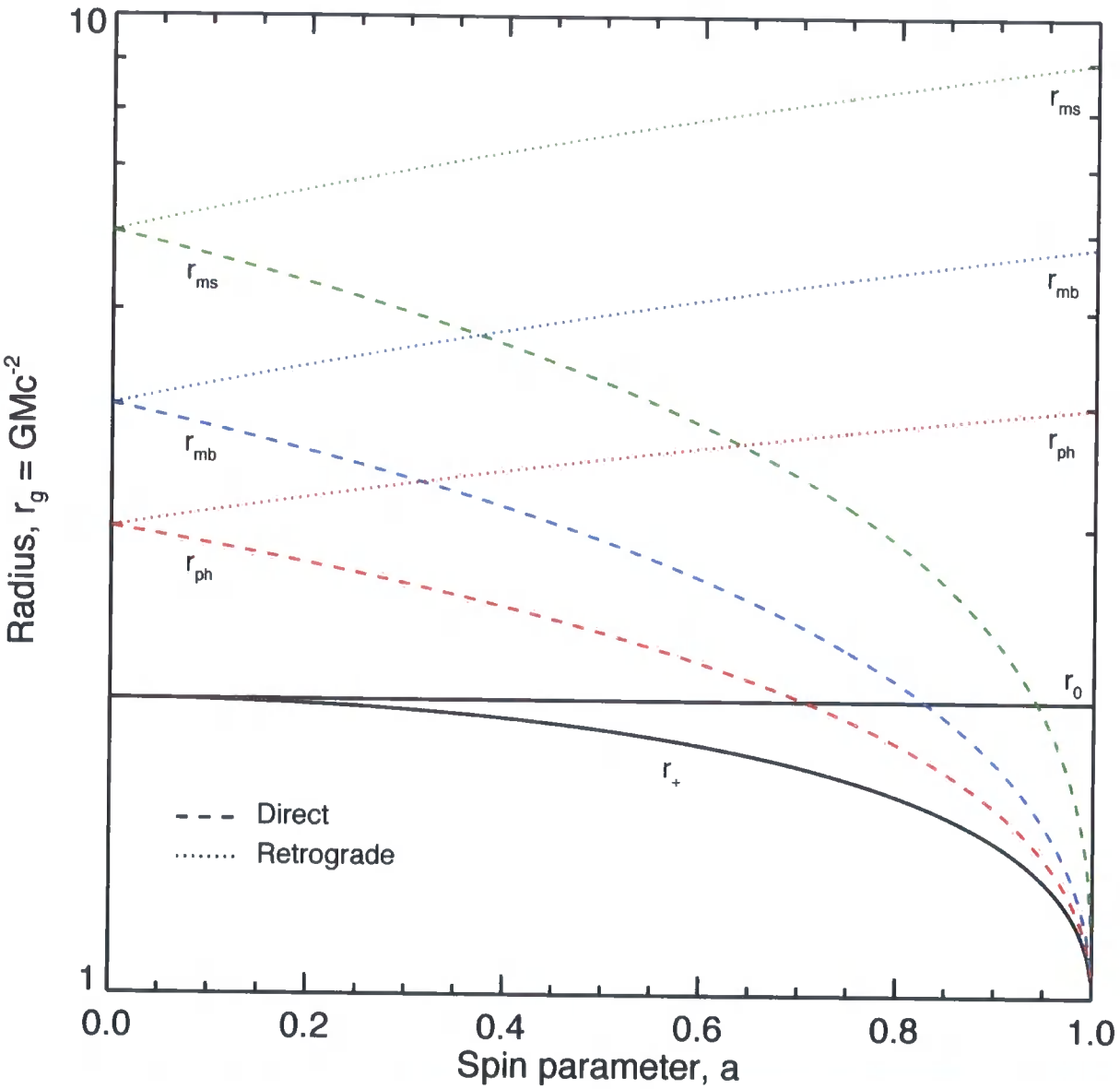

Figure 3.1: "Radii of circular equatorial orbits ... as functions of the hole's ... angular momentum [spin] a. Dashed and dotted curves (for direct and retrograde orbits) plot the Boyer-Lindquist coordinate radius of the innermost stable (ms), innermost bound (mb), and photon (ph) orbits. Solid curves indicated the event horizon (r_+) and the equatorial boundary of the ergosphere (r_0)." Taken from Bardeen et al. (1972)

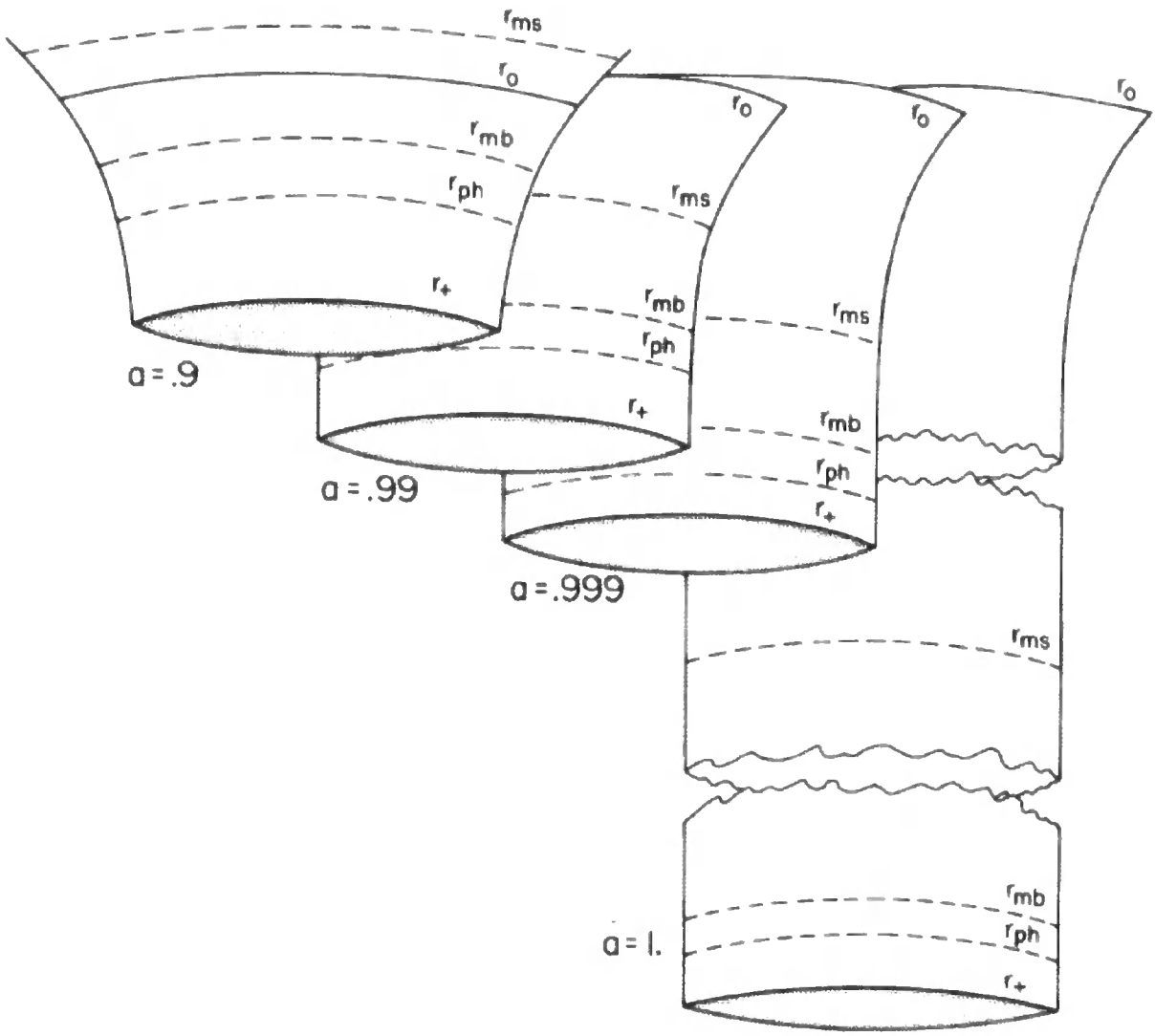

Figure 3.2: "Embedding diagrams of the 'plane' $\theta = \pi/2$, t = constant, for rotating black holes with near-maximum angular momentum. Here, a denotes the hole's angular momentum in units of M. The Boyer-Lindquist radial coordinate r determines only the circumference of the 'tube'. When $a \to M$, the orbits at $r_{\rm ms}$, $r_{\rm mb}$ and $r_{\rm ph}$ all have the same coordinate radius, although - as the embedding diagram shows clearly - they are in fact distinct." Taken from Bardeen et al. (1972)

a contradiction as no time-like curves can exist on the null-hypersurface describing the event horizon, which is due to a subtlety in the Boyer-Lindquist co-ordinate system. In fact, if we consider the proper radial distance between these points, then in the limit $a \rightarrow 1$ these separations remain physically well-behaved, as can be seen in Figure 3.2.

3.2 Calculating Photon Paths in Strong Gravity

3.2.1 Geodesics Around Rotating Black Holes

The separation of the geodesic equations in the Kerr metric was first performed by Carter (1968), in the process discovering the existence of a fourth quantity[2] that is conserved along the geodesic path (in addition to mass, energy and angular momentum). Carter accomplished this by explicitly demonstrating the separability of the Hamilton-Jacobi equation[3] governing geodesic motion, which in a spacetime with a metric tensor $g^{\alpha\beta}$ takes the form:

$$2\frac{\partial S}{\partial \tau} = g^{\alpha\beta}\frac{\partial S}{\partial x^{\alpha}}\frac{\partial S}{\partial x^{\beta}} \tag{3.19}$$

Here, τ is proper time. The contravariant form of the metric tensor, $g^{\alpha\beta}$ has components:

$$g^{\alpha\beta} = \begin{vmatrix} \frac{\Sigma^2}{\rho^2\Delta} & 0 & 0 & \frac{2ar}{\rho^2\Delta} \\ 0 & -\frac{\Delta}{\rho^2} & 0 & 0 \\ 0 & 0 & -\rho^{-2} & 0 \\ \frac{2ar}{\rho^2\Delta} & 0 & 0 & -\frac{\left(\Delta - a^2\sin^2\theta\right)}{\rho^2\Delta\sin^2\theta} \end{vmatrix} \tag{3.20}$$

[2]A physical interpretation of which has recently be given by de Felice & Preti (1999)

[3]The Hamilton-Jacobi description of motion originated out of Hamilton's' conviction that the 'particle world line' of mechanics is an idealisation analogous to the 'light ray' of geometric optics. In geometric optics, the localisation of the energy of the light ray is approximate only - Hamilton had the beginnings of the idea was that this was the same for particles as well - 'quantum physics before quantum physics'! Together with Jacobi, he developed a formalism by which the motion of the particle is analysed through the Hamilton-Jacobi Function, the details of which can be found in Misner et al. (1973),Goldstein (1950)

For completeness, we note that the covariant form of the metric tensor $g_{\alpha\beta}$ has components:

$$g_{\alpha\beta} = \begin{vmatrix} 1-\frac{2r}{\rho^2} & 0 & 0 & \frac{2ar\sin^2\theta}{\rho^2} \\ 0 & -\frac{\rho^2}{\Delta} & 0 & 0 \\ 0 & 0 & -\rho^2 & 0 \\ \frac{2ar\sin^2\theta}{\rho^2} & 0 & 0 & -\left[(r^2+a^2)+\frac{2a^2r\sin^2\theta}{\rho^2}\right]\sin^2\theta \end{vmatrix} \tag{3.21}$$

Substituting the contravariant form of the metric tensor into the Hamilton-Jacobi equation, we obtain:

$$\begin{aligned} 2\frac{\partial S}{\partial \tau} = \frac{\Sigma^2}{\rho^2\Delta}\left(\frac{\partial S}{\partial t}\right)^2 + \frac{4ar}{\rho^2\Delta}\frac{\partial S}{\partial t}\frac{\partial S}{\partial \phi} - \frac{\Delta - a^2\sin^2\theta}{\rho^2\Delta\sin^2\theta}\left(\frac{\partial S}{\partial \phi}\right)^2 \\ -\frac{\Delta}{\rho^2}\left(\frac{\partial S}{\partial r}\right)^2 - \frac{1}{\rho^2}\left(\frac{\partial S}{\partial \theta}\right)^2 \end{aligned} \tag{3.22}$$

We assume that the variables can be separated and seek a solution of the form

$$S = \frac{\delta^2\tau}{2} - Et + L_z\phi + S_r(r) + S_\theta(\theta) \tag{3.23}$$

Here, $\delta^2 = 1, 0$ for particles and photons respectively, E is the energy of the geodesic and L_z is the component of the geodesics angular momentum aligned with the spin axis of the black hole. With much algebra, it is found that the Hamilton-Jacobi equation can be written in the manifestly separable form:

$$\begin{aligned} &\left\{\Delta\left[\frac{dS_r(r)}{dr}\right]^2 - \frac{1}{\Delta}\left[\left(r^2+a^2\right)E - aL_z\right]^2 + \left(L_z - aE\right)^2 + \delta^2 r^2\right\} \\ &+\left\{\left[\frac{dS_\theta(\theta)}{d\theta}\right]^2 + \left(\frac{L_z^2}{\sin^2\theta} - a^2E^2\right)\cos^2\theta + \delta^2 a^2\cos^2\theta\right\} = 0 \end{aligned} \tag{3.24}$$

From this, it is inferred that:

$$\begin{aligned} \Delta\left[\frac{dS_r(r)}{dr}\right]^2 &= \frac{1}{\Delta}\left[\left(r^2+a^2\right)E - aL_z\right]^2 - \left[Q + \left(L_z - aE\right)^2 + \delta^2 r^2\right] \\ \left[\frac{dS_\theta(\theta)}{d\theta}\right]^2 &= Q - \left(\frac{L_z^2}{\sin^2\theta} - a^2E^2 + \delta^2 a^2\right)\cos^2\theta \end{aligned} \tag{3.25}$$

Here, Q is a separation constant ('Carters constant', Carter, 1968). We therefore see that the solution for the Hamilton-Jacobi function, S, is:

$$S = \frac{\delta^2 \tau}{2} - Et + L_z \phi + \int^r \frac{\sqrt{R(r)}}{\Delta} dr + \int^\theta \sqrt{\Theta(\theta)} d\theta \tag{3.26}$$

Here, we have introduced the effective potentials (c.f Eqn. 3.9):

$$\begin{aligned} R(r) &= \left[\left(r^2 + a^2\right) E - a L_z\right]^2 - \Delta \left[Q + (L_z - aE)^2 + \delta^2 r^2\right] \\ \Theta(\theta) &= Q - \left[a^2 \left(\delta^2 - E^2\right) + \frac{L_z^2}{\sin^2 \theta}\right] \cos^2 \theta \end{aligned} \tag{3.27}$$

The complete set of equations governing geodesic motion around a Kerr black hole can then be obtained by setting the partial derivative of the Hamilton-Jacobi function, S (Eqn. 3.26) with respect to the conserved quantities equal to zero. This procedure yields the set of integral equations:

$$\begin{aligned} \int^r \frac{dr}{\sqrt{R(r)}} &= \int^\theta \frac{d\theta}{\sqrt{\Theta(\theta)}} \\ \tau &= \int^r \frac{r^2}{\sqrt{R(r)}} dr + a^2 \int^\theta \frac{\cos^2 \theta}{\sqrt{\Theta(\theta)}} d\theta \\ t &= \tau E + 2 \int^r r \left[r^2 E - a (L_z - aE)\right] \frac{dr}{\Delta \sqrt{R(r)}} \\ \phi &= a \int^r \left[\left(r^2 + a^2\right) E - a L_z\right] \frac{dr}{\Delta \sqrt{R(r)}} + \int^\theta \left(\frac{L_z^2}{\sin^2 \theta} - aE\right) \frac{d\theta}{\sqrt{\Theta(\theta)}} \end{aligned} \tag{3.28}$$

This set of integral equations can be combined to yield the contravariant components of the four-momentum of the geodesic:

$$\begin{aligned} p^r &= \frac{dr}{d\lambda} = \rho^{-2} \sqrt{R(r)}; \quad p^\theta = \frac{d\theta}{d\lambda} = \rho^{-2} \sqrt{\Theta(\theta)}; \\ p^\phi &= \frac{d\phi}{d\lambda} = \rho^{-2} \Delta^{-1} \left[2arE + \frac{L_z}{\sin 2\theta} \left(\rho^2 - 2r\right)\right]; \\ p^t &= \frac{dt}{d\lambda} = \rho^{-2} \Delta^{-1} \left(\Sigma^2 E - 2arL_z\right) \end{aligned} \tag{3.29}$$

The covariant components of the geodesics four-momentum are then found via $p_\alpha = g_{\alpha\beta} p^\beta$,

yielding:

$$\begin{aligned} p_r = g_{rr}p^r = \frac{\sqrt{R(r)}}{\Delta};\ \ p_\theta = g_{\theta\theta}p^\theta = \sqrt{\Theta(\theta)}; \\ p_\phi = g_{\phi t}p^t + g_{\phi\phi}p^\phi = -L_z;\ \ p_t = g_{tt}p^t + g_{t\phi}p^\phi = E \end{aligned} \tag{3.30}$$

Finally, we note that the relation between Carter constant, Q and the covariant components of the photon four-momentum (Eqn. 3.7) can be found simply by rearranging the expression for p_θ in the above.

3.2.2 The Null Geodesic Equations

Material in an accretion flow near to a black hole emits radiation, which is received by a (possibly distant) observer. These photons enable the observer to form an image of the flow, which in turn determines the measured spectral properties (Beckwith & Done, 2004). Photons follow null geodesics, which are obtained from the general case described in the previous section by setting $\delta^2 = 0$ (i.e. photons are massless). For convenience, we reduce the number of parameters for the system by re-normalising L_z and Q with respect to E. We introduce[4]:

$$\lambda = \frac{L_z}{E}; \quad q = \frac{Q}{E} \tag{3.31}$$

The Kerr metric is both stationary and axisymmetric so the derived set of geodesic equations (3.28 - 3.30) are independent of both of the coordinates t and ϕ. The properties of a given geodesic path (specified by a λ, q pair) are therefore completely determined by the 'governing' equation:

$$\pm \int^{r} \frac{dr}{\sqrt{R_{\lambda,q}(r)}} = \pm \int^{\theta} \frac{d\theta}{\sqrt{\Theta_{\lambda,q}(\theta)}} \tag{3.32}$$

The effective potentials take the form:

$$\begin{aligned} R_{\lambda,q}(r) &= \left[\left(r^2 + a^2\right) - a\lambda\right]^2 - \Delta\left[q - (\lambda - a)^2\right] \\ \Theta_{\lambda,q}(\theta) &= q + a^2\cos^2\theta - \lambda^2\cot^2\theta \end{aligned} \tag{3.33}$$

Consider the radial motion of the geodesic, described by the left-hand side of the above. We fix the ends of the radial trajectories at r_e and r_o, which leads us to the general form for radial motion (see e.g. Agol, 1997):

$$I^{s_r^1, s_r^2}_{r,\lambda,q}(r_e, r_o) = \pm \int_{r_e}^{r_o} \frac{dr}{\sqrt{R_{\lambda,q}(r)}} = s_r^1 \left[\int_{r_e}^{r_t} \frac{dr}{\sqrt{R_{\lambda,q}(r)}} + s_r^2 \int_{r_o}^{r_t} \frac{dr}{\sqrt{R_{\lambda,q}(r)}} \right] \tag{3.34}$$

Here, we have denoted the radial turning point (either perihelion or aphelion) of the path motion by r_t and s_r^n $(n = 1, 2)$ can take the values $-1, +1$ dependent on the nature of the

[4] λ will now always denotes L_z/E and is completely unrelated to the affine parameter define in Section 3.1

path, where n is an index and not a power. From the discussion of Wilkins (1972), there are no bound null geodesics that terminate above the horizon, implying that at most there can be one radial turning point along the geodesic path. There are therefore three types of radial motion that we must consider:

1. From r_e to r_o with no radial turning point encountered, implying either $(s_r^1 = +1, s_r^2 = -1)$ if $r_e < r_o$ or $(s_r^1 = -1, s_r^2 = -1)$ if $r_e > r_o$.

2. From r_e inwards to perihelion at r_t, then outwards to r_o, implying that $(s_r^1 = -1, s_r^2 = +1)$ for $r_t < r_e$, $r_t < r_o$.

3. From r_e outwards to aphelion at r_t, then inwards to r_o, implying that $(s_r^1 = +1, s_r^2 = +1)$ for $r_t > r_e$, $r_t > r_o$.

For the latitudinal motion we can, in general, have an arbitrary number of turning points occur along the path (unlike in the radial case). This requires a more complex expression to describe the contribution of the latitudinal motion. We introduce the variable $m = \cos\theta$:

$$\begin{aligned} I_{m,\lambda,q}^{s_m^1,s_m^2,n_m}(m_e, m_o) &= \pm \int_{m_e}^{m_o} \frac{dm}{\sqrt{M_{\lambda,q}(m)}} \\ &= s_m^1 \left[\int_{m_e}^{m_+} \frac{dm}{\sqrt{M_{\lambda,q}(m)}} + s_m^2 \int_{m_o}^{m_+} \frac{dm}{\sqrt{M_{\lambda,q}(m)}} \right] \\ &\quad + \left[2n_m - s_m^1 s_m^2 \left(1 + s_m^2\right) \right] \int_{m_-}^{m_+} \frac{dm}{\sqrt{M_{\lambda,q}(m)}} \end{aligned} \tag{3.35}$$

The effective potential now takes the form $M_{\lambda,q}(m) = q + m^2\left(a^2 - \lambda^2 - q\right) - a^2 m^4$. In the above, $m_{+,-}$ denote the locations of the latitudinal turning points determined by solution of $M_{\lambda,q}(m) = 0$ (Rauch & Blandford, 1994), whilst n_m denotes the number of such turning points through which the path passes and $s_m^{1,2}$ can take the values $-1, +1$. Specifically, the case of s_m^1 is described by two possibilities:

1. If $m_+ = -m_-$, then $s_m^1 = +1, -1$ dependent on whether the path is initially directed towards the 'north' or 'south' poles of the hole respectively.

2. If $m_+ \neq -m_-$, then s_m^1 is in the direction of the closest of $m_{+,-}$ to m_e

The sign of s_m^2 is determined by the number of turning points, n_m through which the geodesic passes, $s_m^2 = -1^{n_m}$.

Geodesic paths are therefore described by:

$$I_{r,\lambda,q}^{s_r^1,s_r^2}(r_e, r_o) - I_{m,\lambda,q}^{s_m^1,s_m^2,n_m}(m_e, m_o) = 0 \tag{3.36}$$

This can be solved analytically in terms of elliptic functions, which is much more efficient than numerical solutions. Rauch & Blandford (1994) tabulate these functions to determine the observed coordinate latitude, θ_{obs} for photons with momenta (λ, q) emitted from a given radius and latitude which arrive at the observers' radial coordinate. Alternatively, Agol (1997), Čadež et al. (1998) fix one end of the radial path at infinity with some inclination and the coordinates at which the other end crosses the equatorial plane. An additional method, due to Viergutz (1993) fixes the ends of the photon paths at the required coordinates, and a minimisation technique is applied to determine valid (λ, q) pairs for a given number of orbits of the black hole.

Our approach combines aspects of those described by Rauch & Blandford (1994) and Viergutz (1993). We invert the reformulated governing equation to obtain the observed co-ordinate latitude of the geodesic, using the technique described by Rauch & Blandford (1994):

$$\begin{aligned}\int_{m_o}^{m_+} \frac{dm}{\sqrt{M_{\lambda,q}(m)}} = s_m^1 s_m^2 I_{r,\lambda,q}^{s_r^1,s_r^2}(r_e, r_o) - s_m^2 \int_{m_e}^{m_+} \frac{dm}{\sqrt{M_{\lambda,q}(m)}} \\ -s_m^1 s_m^2 \left[2n_m - s_m^1 s_m^2 \left(1 + s_m^2\right)\right] \int_{m_-}^{m_+} \frac{dm}{\sqrt{M_{\lambda,q}(m)}}\end{aligned} \tag{3.37}$$

We apply the properties of the effective potentials described by Viergutz (1993) to dramatically reduce the scale of the calculation by analytically restricting the range of λ and q to those which can escape to infinity. Then we search this range for those paths which contribute to a given image order at the required observed inclination. These geodesics are then projected to form an image of the system on the observers sky, which is then

used to determined the measured flux (described in Beckwith & Done, 2004, see Section 3.4). The code therefore allows the fast calculation of geodesics linking any two points in the spacetime that make a specified number orbits of the black hole.

3.2.3 The Zeroes of the Effective Potentials

To obtain solutions of the reformulated governing equation (3.37), we turn to the tables of elliptic integrals provided by Rauch & Blandford (1994), as modified by Agol (1997). These tables, when combined with appropriate numerical techniques allow us, in principal, to determine the geodesics that link an arbitrary emitter, (r_e, m_e) and observer, (r_o, m_o).

In practise, however, this calculation is far from trivial. By specifying the locations of the emitter and receiver, we have placed definite restrictions on the values of the angular momentum parameters, (λ, q) for which geodesic motion between these two locations is even possible. The geodesic motion is dependent on the square root of the two effective potentials, $R_{\lambda,q}(r)$, $M_{\lambda,q}(m)$, which requires that these functions remain positive definite at all points along the path. If, at any point on the geodesic, this requirement is broken, then a potential barrier is necessarily formed and no such motion is possible. Viergutz (1993) has shown that these requirements can be expressed in terms of the interplay of a set of algebraic functions, which we consider further here. Note that the application of these functions enables us to provide tight limits on the region of parameter space which must be considered in the calculation and hence hugely reduce the scale of the calculation.

We begin by introducing:

$$\underline{r} = \min(r_e, r_o); \quad \overline{r} = \max(r_e, r_o)$$
$$\underline{m} = \min(|m_e|, |m_o|); \quad \overline{m} = \max(|m_e|, |m_o|)$$

The condition that no potential barrier exists between the emitter and observer can be re-expressed mathematically as:

$$R_{\lambda,q}(\underline{r} \leq r \leq \overline{r}) \geq 0; \quad M_{\lambda,q}(\underline{m} \leq |m| \leq \overline{m}) \geq 0 \tag{3.38}$$

Since the effective potentials are linear in q, we can express these requirements as:

$$q \leq q_{r,a}(\lambda); \quad q \geq q_{m,a}(\lambda) \tag{3.39}$$

Here:

$$\begin{aligned} q_{r,a}(\lambda) &= \frac{\left[r^2 + a(a-\lambda)\right]^2}{\Delta} + (\lambda - a)^2 \\ q_{m,a}(\lambda) &= \frac{m^2}{1-m^2}\lambda^2 - a^2 m^2 \end{aligned} \tag{3.40}$$

Physically, these curves correspond to the locus of points on the (λ, q) plane for which the given co-ordinate, (r, m) is a zero of the associated effective potential. For the latitudinal motion, it is found that there are two cases that we must consider (taking $\underline{m}$ as the pericentre of the latitudinal motion and similarly $\overline{m}$ is the apocentre):

$$q \geq \begin{cases} q_{\underline{m},a}(\lambda) & |\lambda| < a\sqrt{1-\underline{m}^2}\sqrt{1-\overline{m}^2} \\ q_{\overline{m},a}(\lambda) & |\lambda| \geq a\sqrt{1-\underline{m}^2}\sqrt{1-\overline{m}^2} \end{cases} \tag{3.41}$$

The description of the radial motion is more complex, due to the existence of the unstable photon orbits (Chandrasekhar, 1983). These orbits are described by the existence of a further set of zeroes of the radial effective potential, $R_{\lambda,q}(r) = 0$ that is subject to the additional constraint $\partial_r R_{\lambda,q}(r) = 0$ (see Section 3.1. These conditions yield a pair of parametric equations describing a critical curve on the (λ, q) plane, which define the apparent angular size of the black hole:

$$\begin{aligned} \lambda_c &= \frac{1}{a(r_c - 1)}\left(r_c^2 - a^2 - r_c \Delta_c\right) \\ q_c &= \frac{r_c^3}{a^2 (r_c - 1)^2}\left[4\Delta_c - r_c (r_c - 1)^2\right] \end{aligned} \tag{3.42}$$

The range of values of r_c is given by considering the solutions of $4a^2 = r_c (r_c - 3)^2$ (corresponding to the radii of unstable photon orbits, either direct or retrograde, in the equatorial plane). Following Chandrasekhar (1983), we denote these radii by $r_{ph}^{(+)}$ and $r_{ph}^{(-)}$ and so $r_{ph}^{(+)} \leq r_c \leq r_{ph}^{(-)}$.

The second complication to this discussion stems from Wilkins (1972). Specifically, for any particle, orbits with $E^2 > \delta^2$ (where E^2 denotes particle energy; $\delta^2 = 1, 0$ particle mass), are unbound, whilst orbits with $E^2 < \delta^2$ are bound. Since photons are massless, this implies that the only bound orbits are those with negative E^2 (and so must terminate behind the horizon), whilst all others must be unbound (except for a set of unstable, circular orbits). We cannot therefore (unlike in the previous discussion) consider trajectories with $\underline{r}$ as pericentre and $\overline{r}$ as apocentre.

For our purposes, three particular cases describing the behaviour of the $q_{r,a}(\lambda)$ curve are of interest. To illustrate these, we consider an extreme Kerr ($a = 1$) hole, with the observer located at radial infinity and an inclination of $\theta_o = 30°$. We locate the emitter in the equatorial plane and begin by considering the case $r_{ph}^{(-)} \leq \underline{r}$ (Figure 3.3, left panel). Here, the region of the angular momentum (λ, q) plane for which no potential barrier is formed between the emitter and observer is bounded from below by $q_{m,a}(\lambda)$, as described by equation 3.41. The upper limit of this region is provided by $q_{\underline{r},a}(\lambda)$ and it can be shown that, independent of the locations of the emitter and observer, these curves are concave and convex functions of λ, respectively. This indicates that we can provide limits on the allowed range of λ via:

$$\lambda_{+,-}\left(\overline{m}, \underline{r}, a\right) = \frac{2a\underline{r}\left(1-\overline{m}^2\right) \pm \sqrt{\underline{\Delta}}\sqrt{1-\overline{m}^2}\left(\underline{r}^2+\overline{m}^2a^2\right)}{\underline{\Delta} - a^2\left(1-\overline{m}^2\right)} \tag{3.43}$$

The apparent angular size of the black hole is defined by the parametric curve $q_c\left(r_c\right), \lambda_c\left(r_c\right)$. Hence, photons whose angular momentum falls under this curve and are directed initially inwards towards the hole from $\underline{r}$ are inevitably captured. For $r_{ph}^{(-)} \leq \underline{r}$, this critical curve intersects the graph of $q_{m,a}(\lambda)$ at some $\lambda_c^{+,-}$ (the exact intersection being determined numerically) and so inwardly directed photons with $\lambda_c^- \leq \lambda \leq \lambda_c^+$, $q_{m,a}(\lambda) \leq q \leq q_c(r_c)$, where r_c is determined by inversion of $\lambda = \lambda_c(r_c)$, can be completely excluded from the calculation.

We now move the location of the emitter inwards such that $r_{ph}^{(+)} \leq \underline{r} \leq r_{ph}^{(-)} \leq \overline{r}$ (Figure 3.3, centre panel). We have that the valid region of the angular momentum plane

is bounded from below by $q_{m,a}(\lambda)$, as before. The behaviour of the upper bound to the angular momentum plane is, however, quite different. In this case, since $r_{ph}^{(+)} \leq \underline{r} \leq r_{ph}^{(-)}$, there exists some $r_c^* = \underline{r}$, which is associated with a (λ_c^*, q_c^*) pair, through equations (3.42). For $\lambda \leq \lambda_c^*$, we therefore have that the upper limit of the angular momentum plane is given by the critical curve and hence the lower limit on λ is determined by λ_c^+. Similarly, above λ_c^*, the upper limit on the plane is given, as in the previous case, by $q_{\underline{r},a}(\lambda)$ and so the upper limit on λ is given by $\lambda_+(\overline{m}, \underline{r}, a)$. Note that, for $\lambda \leq \lambda_c^*$ there are no photons that are emitted on radially inbound geodesics that reach the observer, whilst for $\lambda > \lambda_c^*$, only those initially in-going photons with values of q above the critical curve can reach the observer. Finally, we note that for the emitter located at $\underline{r} \leq 2r_g$ (Figure fig:2.1, right-hand panel), the graph of $q_{r,a}(\lambda)$ is now convex. However, the relationship between the various curves remains unchanged from that described in the previous case and the angular momentum plane remains bound.

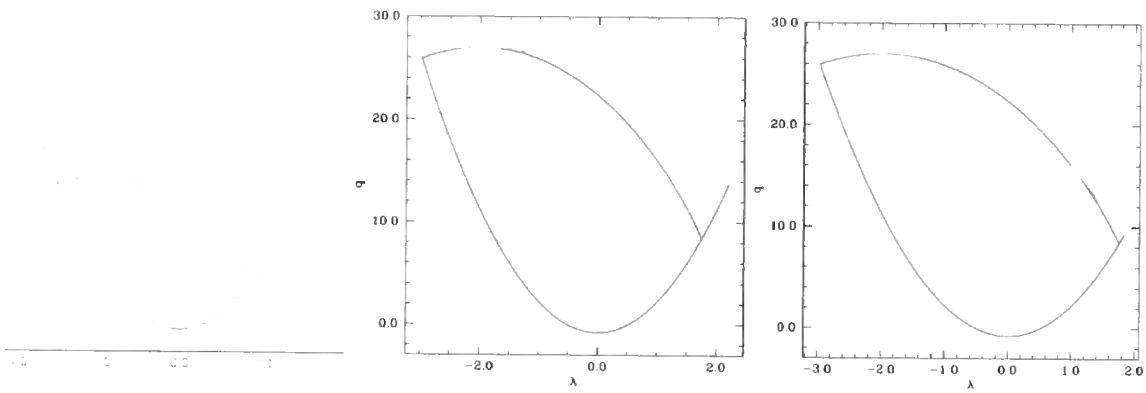

Figure 3.3: Boundary curves on the (λ, q)-plane for an extreme ($a = 1$) Kerr black hole with $r_o = \infty$, $\theta_e = \pi/2$ and $\theta_o = 30°$. The graph of $q_{m,a}(\lambda)$ is shown by the red curve, $q_{r,a}(\lambda)$ by the green and $q_c(r_c), \lambda_c(r_c)$ by the blue. On the left-hand panel, the emitter is located at $r_e = 6r_g$, such that $r_e > r_{ph}^{(-)}$ and hence the valid region is bounded by $q_{r,a}(\lambda)$ from above and $q_{m,a}(\lambda)$ from below, whilst the $q_c(r_c), \lambda_c(r_c)$ describes the line below which a photon directed radially inward is inevitably captured by the hole. In the central panel, the emitter is now located at $r_e = 3r_g$, such that $r_{ph}^{(+)} \leq r_e \leq r_{ph}^{(-)}$. The parameter space is again bounded by $q_{m,a}(\lambda)$ from below, however in this case, the upper limit is given by $q_c(r_c), \lambda_c(r_c)$ for $\lambda \leq \lambda_c(r_e)$ and by $q_{r,a}(\lambda)$ otherwise. Finally, we see that for $r_e = 2r_g$ (right-hand panel), these boundaries still apply, even though the graph of $q_{r,a}(\lambda)$ is now concave (true for all $r \leq 2r_g$).

3.2.4 Structure & Properties of Loops on the (λ, q) Plane

We begin by considering solutions to the 'governing' equation for a simple system where the emitter is located in the equatorial plane of an extreme Kerr ($a = 1$) hole ($\theta_e = \pi/2$) and takes the form of an infinitesimal ring located at radius r_e. For such an infinitesimal ring, the flux is undefined (since the ring subtends zero solid angle on the observers sky) and so we concentrate our attention on the behaviour of the solutions on the (λ, q)-plane and the reference frame of a distant observer, the (α, β)-plane[5] (Figure 3.4). To minimise the impact of gravitational lensing, we locate the observer at radial infinity and $\theta_o = 30°$ (as previously).

Initially, we locate the ring at $r_e = 8r_g$ (Figure 3.4, left-most panel) and catalogue the complete set of geodesics of zeroth ($N = 0$), first ($N = 1$) and second ($N = 2$) order. Each of these geodesic orders form a closed loop on both the (λ, q) and (α, β) planes. We note that the projections on both planes are asymmetric about the line $\lambda, \alpha = 0$ due to the breaking of spherical symmetry by the black hole spin and also (for the emitter located at $8r_g$) that the loops for each individual image order are completely detached. We now move the emitter inwards to $r_e = 6r_g$ (Figure 3.4, second from left panel), which causes the loops associated with the zeroth and first order images to overlap. The solutions to the geodesic equations are therefore multivalued at these points in (λ, q) space, breaking the statement by Cunningham (1975) that there are two geodesics linking a point on the accretion disc to an observer for each value of the redshift parameter, g, which (for the Keplerian disc considered by Cunningham), corresponds to two geodesics at each valid point in λ space. If we now move the emitter inwards to $r_e = 4r_g$ (Figure 3.4, third from left panel), we now see that the loops associated with the zeroth order geodesic now overlaps with both the first order loop and the second order loop.

We now move the emitter further inwards, so that $r_{ph}^{(+)} \leq r_e = 3r_g < r_{ph}^{(-)}$ (Figure 3.4, third from right panel). Here, the zeroth order loop still overlaps the first and second

[5] see Section 3.3.2

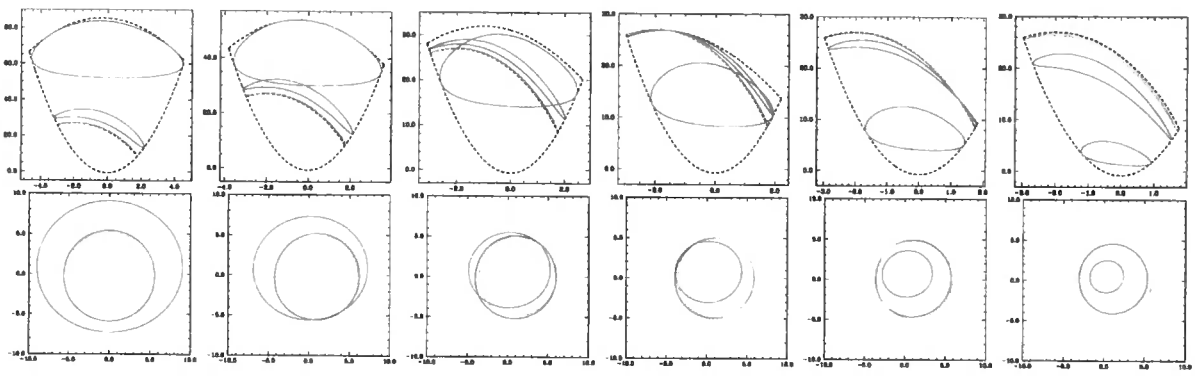

Figure 3.4: Closed loops on the (λ, q)-plane (top row) and their projection onto the observers sky (the α, β plane, bottom row) for an extreme ($a = 1$) Kerr black hole with $r_o = \infty$, $\theta_e = \pi/2$ and $\theta_o = 30°$. Geodesics with $N = 0$ are shown as red lines, those with $N = 1$ as blue lines and $N = 2$ as green lines. Also shown for references on the (λ, q)-plane representation are the parameter space boundaries (black lines). From left to right, the each panel has $r_e = 8, 6, 4, 3, 2, 1 r_g$. Note the change in the relative locations of the loops as the emitter moves inwards - for $r_e = 8r_g$, the loops for each image order are completely detached. However, as the emitter moves in to $6r_g$, the $N = 0, 1$ loops overlap and by the time the emitter reaches $4r_g$, the $N = 0$ loop overlaps both the $N = 1$ and $N = 2$ loop. At $3r_g$, the $N = 0$ loop again crosses the $N = 1, 2$ loops, however in this case the $N = 1$ and $N = 2$ loops now touch. Moving the emitter inward to $2r_g$, the $N = 0$ loop detaches itself and moves inside the $N = 1, 2$ loops, which cross. Moving the emitter still further inward, to just above r_+, we now see that $N = 1, 2$ loops have detached, with the $N = 1$ loop now occurring between the $N = 0, 2$ loops.

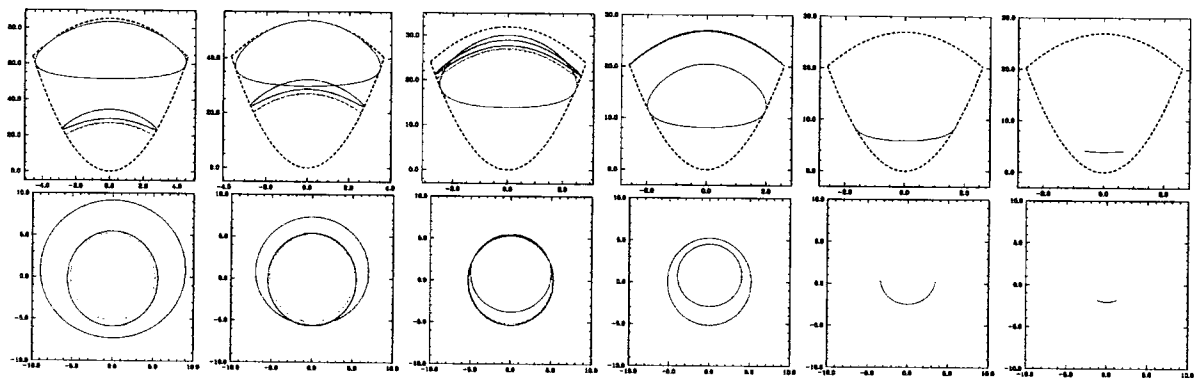

Figure 3.5: As in Figure 3.4 for a Schwarzschild ($a = 0$) black hole, with (from left to right) $r_e = 8, 6, 4, 3, 2.5, 2r_g$. The loops display a qualitatively similar behaviour to that described in the $a = 1$ case. We note that the restoration of spherical symmetry to the system (due to the absence of rotation) has removed the asymmetry of the loops on both planes and hence changed the points of overlap of the loops with respect to the $a = 1$ case. For $r_e \leq 3r_g$, there are no photons with $N = 2$ that propagate to infinity, furthermore for $r_e < 3r_g$, there are no $N = 1$ photons that can propagate to infinity either. More importantly, for $r_e < 3r_g$ a distant observer is unable to form a complete (that is $\phi = 0 \rightarrow 2\pi$) image of the ring even using direct ($N = 0$) photons.

order loops, however, in this case the first and second order loops now touch. Moving the emitter inwards still further to $r_e = 2r_g$ (Figure 3.4, second from right panel), the zeroth order loop now detaches itself from the first and second order loops and moves inside these loops on the (α, β) plane projection. The apparent angular size of the zeroth order loop, as measured by the distant observer, is now smaller than that of the first and second order loops, which has important consequences for the calculation of the emergent flux, as we shall shortly see. Finally, we move the emitter down to $r_e - r_g = 10^{-6}$ (Figure 3.4, right-most panel), the location of r_+ in Boyer-Lindquist coordinates (however, this is not the case in terms of proper distance, see Bardeen et al., 1972). All of the loops are again detached, however, in comparison to the case where $r_e = 8r_g$, the ordering of these loops is now reversed on the (α, β) plane, with the second order now subtending the greatest angular size of the observers sky.

We now replace the central extreme Kerr black hole with a Schwarzschild ($a = 0$) black hole and repeat the preceding calculation. From Figure 3.5, we see that the behaviour of the solutions on the two planes is qualitatively similar to that of the extreme Kerr case as we move the emitter from $8r_g$ down to $4r_g$. However, in this case we note that the loops are now symmetric about the line $\lambda, \alpha = 0$ due to the absence of rotation in the system and that this results in the quantitative locations of the overlap to change. Note that we can understand the existence of these overlaps by considering the meaning of the projection of these loops on the (λ, q) plane. Recall that, for given (λ, q) pair, there exists a set of roots (r_i, m_i) of the effective potentials $R_{\lambda,q}(r)$, $M_{\lambda,q}(m)$. Whether or not the geodesic path passes through selected members of these sets of roots depends on the initial direction taken by the geodesic, described by the s_r, s_m parameters in equation 3.41 and hence different geodesic paths can be described by a single (λ, q) pair.

Consider now the behaviour of these loops as we move the emitter to $r_e = 3r_g$ for the Schwarzschild hole (Figure 3.5, third from right panel). Here, we find that the zeroth and first order loops are now detached, but in this case the second order loop does not

exist. Moving the emitter in further to $2.5r_g$ (Figure 3.5, second from right panel), we find that not only does the first order loop disappears, but the zeroth order loop is no longer closed! Finally, if we move the emitter to $r_e - 2r_g = 10^{-6}$ (Figure 3.5, right-most panel), then we find that we are only able to image a small line segment from the ring. To understand this behaviour, we turn to the discussion given by Chandrasekhar (1983) regarding the 'cone of avoidance', describing the cone generated the photons that pass through the unstable circular orbits located at $3r_g$. We let ψ denote the half-angle of the cone (directed inward at large distances from the hole) and it can then be shown that:

$$\tan\psi = \frac{1}{r/3-1}\sqrt{\frac{r/2-1}{r/6+1}} \tag{3.44}$$

We therefore see that for $r \leq 3r_g$, $\psi \leq \pi/2$, which implies that below $3r_g$, the apparent angular size of the black hole is greater than that of the distant stars. This shows that the black hole obscures part of the region $\phi = 0 \rightarrow 2\pi$ for a distant observer when the emitter is located below $r = 3r_g$, which implies that the dynamics of the accretion flow in this region are extremely difficult to directly measure.

3.2.5 General Emission Geometries

In the standard picture of accretion onto a massive compact object, the emitting material is located in the equatorial plane in what is assumed to be a geometrically thin structure. As such, gravitational lensing effects only come into play for high inclination systems ($\theta_o > 60°$). However, if one wishes to consider emission from a non-equatorial geometry (the case of a geometrically thick, optically thin accretion flow, for example), then gravitational lensing effects can have important consequences even for low inclination observers. As an example, consider again two infinitesimal rings, located at $r_e = 6r_g$, with polar coordinates $\theta_e^a = 149°$ and $\theta_e^b = 151°$. We again locate the observer at radial infinity and initially take $\theta_o = 25°$ such that $|\theta_o| < |\theta_e^{a,b}|$ (Figure 3.6 left panel). The two rings form are mapped continuously onto the (α, β) plane for each individual image order in a similar

fashion to those considered previously. We now move the latitudinal coordinate of the observer to $\theta_o = 30°$, such that $|\theta_e^a| < |\theta_o| < |\theta_e^b|$ (Figure 3.6 centre panel). The image of the lower ring, θ_e^b is again mapped continuously onto the (α, β) plane for each individual image order, as would be expected as it's relationship to the latitudinal coordinate of the observer has remained unchanged. This is not true however of the image of the upper ring, θ_e^a, which is now mapped discontinuously onto the (α, β) plane, with the even image orders (zeroth and second) appearing from the southern hemisphere of the hole and the odd image orders (first) appearing from the northern hemisphere. It is therefore clear that, in order to generate a complete picture of the physical properties of such a system, we must include the contribution of the higher orders to the calculation. Finally, we again move the observer in the latitudinal direction to $\theta_o = 35°$, such that $|\theta_o| > |\theta_e^{a,b}|$ (Figure 3.6 right panel). Now the images of both rings are mapped discontinuously onto the (α, β) plane, which serves to further emphasise the importance of the inclusion of the higher order images in the calculation.

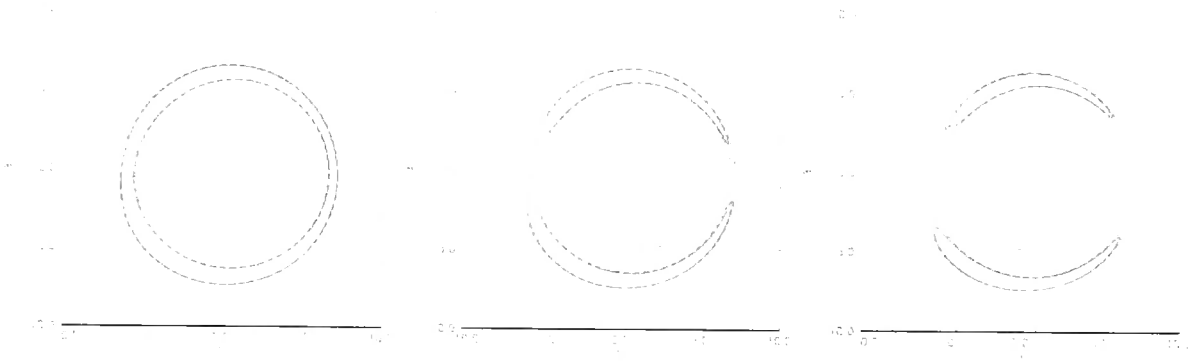

Figure 3.6: Two emitting rings around an extreme Kerr black hole located at $r_e = 6r_g$ and $\theta_e^a = 149°$ (solid lines), $\theta_e^b = 151°$ (dashed lines) with the direct, first and second order images denoted by red, blue and green lines respectively. The observer is located at radial infinity with polar coordinate $\theta_o = 25°$ (left panel), $\theta_o = 30°$ (centre panel) and $\theta_o = 35°$ (right panel). In the left panel, $|\theta_o| < |\theta_e^{a,b}|$, producing circular images of the emitting rings. In the centre panel, we now have that $|\theta_e^a| < |\theta_o| < |\theta_e^b|$ and the image of the θ_e^a ring has now separated such that the zeroth and second order images appear from the south pole of the hole, whilst the first order image appears from behind the north pole. Finally, in the right-hand panel, we have that $|\theta_o| > |\theta_e^{a,b}|$ and so images of both $\theta_e^{a,b}$ follow this behaviour.

3.3 Local Reference Frames

3.3.1 The Tetrad Formalism

Many of the problems that we shall encounter in calculating the spectral properties of accretion flows around rotating black holes will require the measurement of physical parameters (such as photon energy and direction of propagation) in the rest frame of some (arbitrarily) moving observer. We are fortunate that a formalism capable of providing such a description is well developed, so we are able to simply give an account of the principle characteristics and techniques required in such a calculation.

The approach to this problem that we shall adopt is that of the tetrad formalism, which we give a brief introduction to here (due to Chandrasekhar, 1983). Succinctly put, we generate a set of four basis vectors for the observers coordinate system. The required quantities are then determined by the projection of the relevant equations onto this basis.

Let us initially consider an observer who is at rest at some point within the spacetime of the black hole. For each such observer, we define a set of contravariant basis vectors $e^{\nu}_{(\alpha)}$, where the subscript (α) denotes the tetrad indices and the superscript ν denotes the tensor indices. Associated with this set of contravariant set of basis vectors, we have a set of covariant basis vectors:

$$e_{(\alpha)\mu} = g_{\mu\nu} e^{\nu}_{(\alpha)} \tag{3.45}$$

We require that the basis set be orthonormal, i.e

$$e^{\mu}_{(\alpha)} e^{(\beta)}_{\mu} = \delta^{(\beta)}_{(\alpha)}; \quad e^{\mu}_{(\alpha)} e^{(\alpha)}_{\nu} = \delta^{\mu}_{\nu} \tag{3.46}$$

As a consequence of these requirements, we see that $e^{\mu}_{(\alpha)} e_{(\beta)\nu} = \eta_{(\alpha)(\beta)}$, where $\eta_{(\alpha)(\beta)}$ is a constant, symmetric matrix, which we shall take to have the form (consistent with the

convention for $g_{\mu\nu}$):

$$\eta_{(\alpha)(\beta)} = \begin{vmatrix} 1 & 0 & 0 & 0 \\ 0 & -1 & 0 & 0 \\ 0 & 0 & -1 & 0 \\ 0 & 0 & 0 & -1 \end{vmatrix} \tag{3.47}$$

The frame described by the basis vectors, $\mathbf{e}_{(\alpha)}$ is therefore an inertial frame. As a further consequence of these definitions, the tetrad indices of the basis vectors are raised and lowered by application of this matrix and it's associated inverse, $\eta^{(\alpha)(\beta)}$, i.e.

$$e^{\mu}_{(\alpha)} = \eta_{(\alpha)(\beta)} e^{(\beta)}_{\mu}; \;\; e^{(\alpha)}_{\mu} = \eta^{(\alpha)(\beta)} e_{(\beta)\nu} \tag{3.48}$$

We can then measure physical quantities in the frame defined by the tetrad basis vectors by projecting the relevant tensor quantity onto the basis:

$$p_{(\alpha)} = p_{\mu} e^{\mu}_{(\alpha)} = p_{\mu} \eta_{(\alpha)(\beta)} e^{(\beta)}_{\mu} = p_{\mu} \eta_{(\alpha)(\beta)} g_{\mu\nu} e^{(\beta)\nu} \tag{3.49}$$

3.3.2 The Locally Non-Rotating Frame

The first of these inertial frames that we shall discuss is the Locally Non-Rotating Frame (LNRF) due to Bardeen et al. (1972). This is a frame that is locked to the rotation of the metric, i.e. the observer to whom the frame is attached rotates around the symmetry axis of the black hole with an angular velocity ω (such that the observers resultant angular angular momentum is zero). Throughout what follows, this observer is known as the locally non-rotating observer. Such a frame is useful as it allows the simple description of physical quantities - time-like directions remain time-like and the metric tensor is diagonal (indices can be raised and lowered freely, without the introduction of additional algebraic complexity).

Associated with the line element (Eqn. 3.1), we have the basis vectors (valid for any

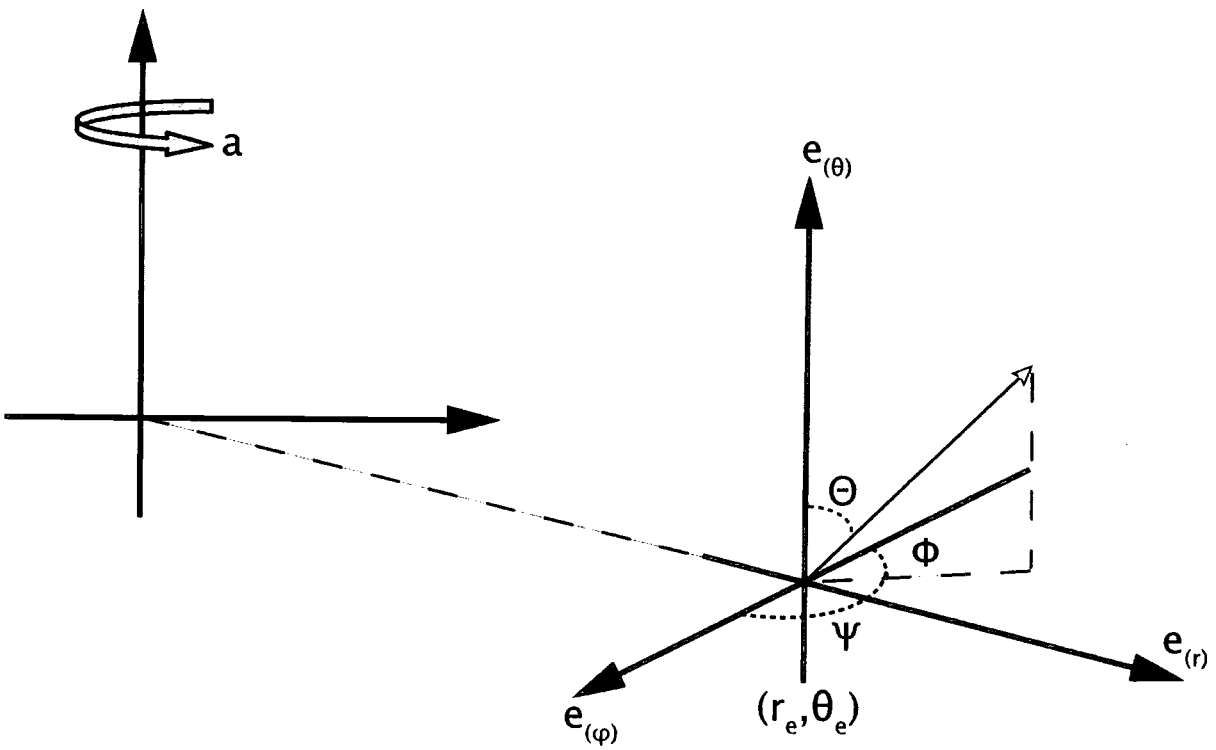

Figure 3.7: The co-ordinate system associated with the Locally Non-Rotating Frame. The components of the photons 4-momentum in this frame are evaluated through $p_{(\mu)} = p_\nu e^\nu_{(\mu)}$. From these we can define the angles formed by the spatial components of p_μ with the basis vectors of the LNRF through the relations $\cos\Theta = p_{(\theta)}/p_{(t)}$, $\sin\Theta\sin\Phi = p_{(r)}/p_{(t)}$, $\sin\Theta\cos\Phi = \cos\Psi = p_{(\phi)}/p_{(t)}$.

stationary, axisymmetric spacetime):

$$e_{(\alpha)\sigma} = \begin{vmatrix} e^{\nu} & 0 & 0 & 0 \\ 0 & -e^{\mu_1} & 0 & 0 \\ 0 & 0 & -e^{\mu_2} & 0 \\ \omega e^{\psi} & 0 & 0 & -e^{\psi} \end{vmatrix}; \quad e^{\sigma}_{(\alpha)} = \begin{vmatrix} e^{-\nu} & 0 & 0 & \omega e^{-\nu} \\ 0 & e^{\mu_1} & 0 & 0 \\ 0 & 0 & e^{\mu_2} & 0 \\ 0 & 0 & 0 & e^{\psi} \end{vmatrix} \tag{3.50}$$

We can use these basis vectors to assign directions to the photons four-momentum, p_a as measured by our locally non-rotating observer. We introduce (see Figure 3.7):

$$\cos\Theta = \frac{p_{(\theta)}}{p_{(t)}}; \quad \sin\Theta\sin\Phi = \frac{p_{(r)}}{p_{(t)}}; \quad \sin\Theta\cos\Phi = \cos\Psi = -\frac{p_{(\phi)}}{p_{(t)}}; \tag{3.51}$$

We choose Θ to run over the range $0 \rightarrow \pi$ and Φ to run over the range $0 \rightarrow 2\pi$, with the basis vectors orientated as shown in Figure 3.7. Note that, in the limit $r \rightarrow \infty$, these angles have simple relations to the impact parameters ('celestial coordinates') of the photon (Chandrasekhar, 1983, see Figure 3.8):

$$\alpha = \lim_{r\to\infty}(-r\cos\Psi) = \lim_{r\to\infty}\left[\frac{rp_{(\phi)}}{p_{(t)}}\right]; \quad \beta = \lim_{r\to\infty}(r\cos\Theta) = \lim_{r\to\infty}\left[\frac{rp_{(\theta)}}{p_{(t)}}\right] \tag{3.52}$$

Evaluating $p_{(\alpha)} = p_\mu e^{\mu}_{(\alpha)}$, we find:

$$p_{(\alpha)} = \left| \; e^{-\nu}(1-\lambda\omega) \quad -e^{\mu_1}\Delta^{-1}\sqrt{R_{\lambda,q}(r)} \quad -e^{\mu_2}\sqrt{\Theta_{\lambda,q}(\theta)} \quad -e^{-\psi}\lambda \; \right| \tag{3.53}$$

We can therefore express the angles formed by the photons four-momentum with the axes of the frame of the locally non-rotating observer in the form:

$$\cos\Theta = -\frac{e^{\mu_2}\sqrt{\Theta_{\lambda,q}(\theta)}}{e^{-\nu}(1-\lambda\omega)}; \quad \sin\Theta\sin\Phi = -\frac{e^{\mu_1}\Delta^{-1}\sqrt{R_{\lambda,q}(r)}}{e^{-\nu}(1-\lambda\omega)}; \quad \sin\Theta\cos\Phi = \cos\Psi = \frac{e^{-\psi}\lambda}{e^{-\nu}(1-\lambda\omega)}; \tag{3.54}$$

The impact parameters of the photon (for an observer located at radial infinity with polar coordinate θ_o are then found to be:

$$\alpha = -\frac{\lambda}{\sin\theta_o}; \quad \beta = \pm\sqrt{q + a^2 cos^2\theta_o - \lambda^2 \cot^2\theta_o} \tag{3.55}$$

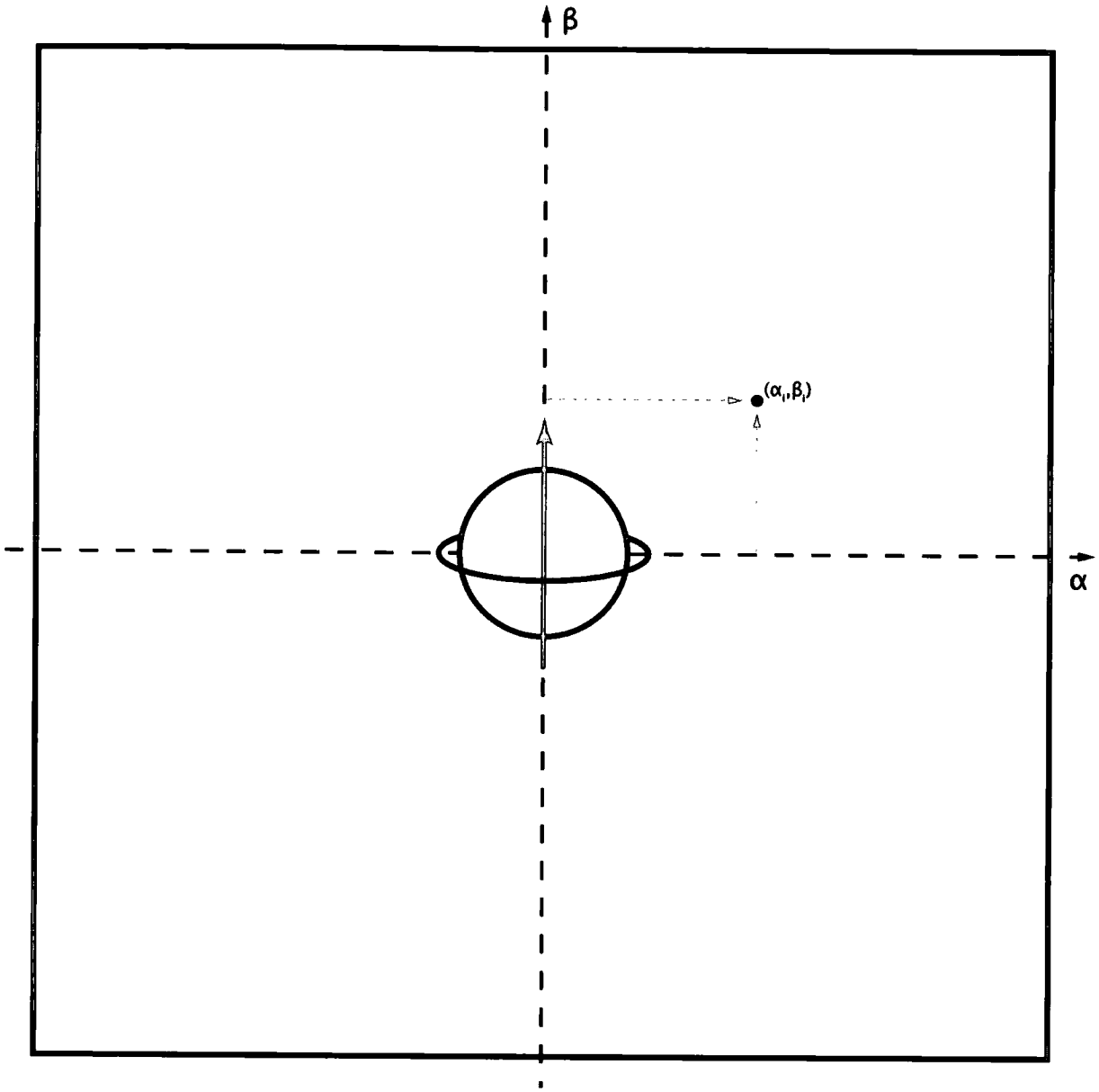

Figure 3.8: "A small patch on the celestial sphere of a distant observer at radius r_o. The black hole is represented by a circle of unit radius, centred about the inward radial direction." The red arrow indicates the symmetry axis of the hole. A geodesic specified by the conserved quantities (λ_i, q_i) appears on the celestial sphere with celestial co-ordinates (impact parameters) (α_i, β_i). Adapted from (Bardeen & Cunningham, 1973)

Finally, we can also find particularly simple expressions of the photons constants of motion in terms of the angles formed by the photons four-momentum and the basis vectors of the locally non-rotating frame:

$$\lambda = \frac{\cos\Psi}{1+\omega e^{\nu-\psi}\cos\Psi};\quad q = e^{2(\mu_2-\nu)}(1-\lambda\omega)^2\cos^2\Theta - \cos^2\theta\left[a^2 - \frac{\lambda^2}{\sin^2\theta}\right]; \tag{3.56}$$

3.3.3 The Local Disk Frame

Consider an arbitrary observer, X, moving with four-velocity u^μ in the global Boyer-Lindquist coordinate system:

$$u^\mu = \begin{vmatrix} u^t & u^r & u^\theta & u^\phi \end{vmatrix} = u^t \begin{vmatrix} 1 & v^r & v^\theta & v^\phi \end{vmatrix};\ v^i = \frac{u^i}{u^t} \tag{3.57}$$

As viewed by a locally non-rotating observer, Y, the observer X will have four-velocity:

$$\begin{aligned} u^{(\alpha)} = u^{(t)} \begin{vmatrix} 1 & v^{(r)} & v^{(\theta)} & v^{(\phi)} \end{vmatrix} &= u^\sigma e^{(\alpha)}_\sigma = u^\sigma \eta^{(\alpha)(\beta)} e_{(\alpha)\sigma} \\ &= e^\nu u^t \begin{vmatrix} 1 & e^{\mu_1-\nu}v^r & e^{\mu_2-\nu}v^\theta & e^{\psi-\nu}(v^\phi-\omega) \end{vmatrix} \end{aligned} \tag{3.58}$$

From Chandrasekhar (1983), Bardeen et al. (1972), we see that if the observer, X moves on a circular orbit angular velocity v^ϕ, then the locally non-rotating observer assigns them the angular velocity $v^{(\phi)} = e^{\psi-\nu}(v^\phi - \omega)$. Similarly, the locally non-rotating observer, who is at rest in their inertial frame, $v^{(r)} = v^{(\theta)} = v^{(\phi)} = 0$ will, in the global frame, be assigned the four-velocity:

$$u^\sigma = u^{(\alpha)} e^\sigma_{(\alpha)} = e^{-\nu} \begin{vmatrix} 1 & 0 & 0 & \omega \end{vmatrix} \tag{3.59}$$

The inertial frame therefore rotates with angular velocity ω, known as the 'dragging of the inertial frame'. Now, since the observer X moves with respect to the inertial frame of the locally non-rotating observer, Y with three-velocity v^i, then the reference frame of X differs from the reference frame of Y by means of a standard Lorentz transformation

(Misner et al., 1973):

$$\Lambda^{(\alpha)}_{[\beta]} = \begin{vmatrix} \gamma & \gamma v^{(r)} & \gamma v^{(\theta)} & \gamma v^{(\phi)} \\ \gamma v^{(r)} & 1+(\gamma-1)|v|^{-2}[v^{(r)}]^2 & (\gamma-1)|v|^{-2}v^{(r)}v^{(\theta)} & (\gamma-1)|v|^{-2}v^{(r)}v^{(\phi)} \\ \gamma v^{(\theta)} & (\gamma-1)|v|^{-2}v^{(\theta)}v^{(r)} & 1+(\gamma-1)|v|^{-2}[v^{(\theta)}]^2 & (\gamma-1)|v|^{-2}v^{(\theta)}v^{(\phi)} \\ \gamma v^{(\phi)} & (\gamma-1)|v|^{-2}v^{(\phi)}v^{(r)} & (\gamma-1)|v|^{-2}v^{(\phi)}v^{(\theta)} & 1+(\gamma-1)|v|^{-2}[v^{(\phi)}]^2 \end{vmatrix}$$

Here, $\gamma = (1-|v|^{-2})^{-1}$ and $|v|^2 = [v^{(r)}]^2 + [v^{(\theta)}]^2 + [v^{(\phi)}]^2$. The basis vectors of the inertial frame associated with the observer X are then given by $e^{\sigma}_{[\beta]} = e^{\sigma}_{(\alpha)}\Lambda^{(\alpha)}_{[\beta]}$, with the corresponding components of the photon four-momenta given by $p_{[\beta]} = p_{\sigma}e^{\sigma}_{[\beta]} = p_{\sigma}e^{\sigma}_{(\alpha)}\Lambda^{(\alpha)}_{[\beta]}$ (which are far too lengthy to be written down here!). Note that it is no longer possible to provide simple expressions of the photons constants of motion λ, q in terms of the angles made with the basis vectors of the co-moving frame of the observer.

In the case of one dimensional motion ($v^{(r)} = v^{(\theta)} = 0$, say), $\Lambda^{(\alpha)}_{[\beta]}$ reduces to the familiar form:

$$\Lambda^{(\alpha)}_{[\beta]} = \begin{vmatrix} \gamma & 0 & 0 & \gamma v^{(\phi)} \\ 0 & 1 & 0 & 0 \\ 0 & 0 & 1 & 0 \\ \gamma v^{(\phi)} & 0 & 0 & \gamma \end{vmatrix} \tag{3.60}$$

In this case, which we shall refer to as the Local Disk Frame (LDF), the basis vectors of the co-moving frame take the form (Martocchia, 2000):

$$e^{\sigma}_{[\alpha]} = \begin{vmatrix} e^{-\nu}\gamma & 0 & 0 & (\omega e^{-\nu}+e^{-\psi})\gamma v^{(\phi)} \\ 0 & e^{-\mu_1} & 0 & 0 \\ 0 & 0 & e^{-\mu_2} & 0 \\ (\omega e^{-\nu}+e^{-\psi})\gamma v^{(\phi)} & 0 & 0 & e^{-\psi}\gamma \end{vmatrix} \tag{3.61}$$

The photons four-momentum therefore has LDF components:

$$\begin{aligned} p_{[t]} &= \gamma e^{-\nu}\left(1-\lambda v^{\phi}\right); \quad p_{[r]} = -e^{\mu_1}\Delta^{-1}\sqrt{R_{\lambda,q}(r)} \\ p_{[\theta]} &= -e^{\mu_2}\sqrt{\Theta_{\lambda,q}(\theta)}; \quad p_{[\phi]} = -e^{-\psi}\lambda[v^{(\phi)}\omega e^{\psi-\nu}+v^{(\phi)}+1] \end{aligned} \tag{3.62}$$

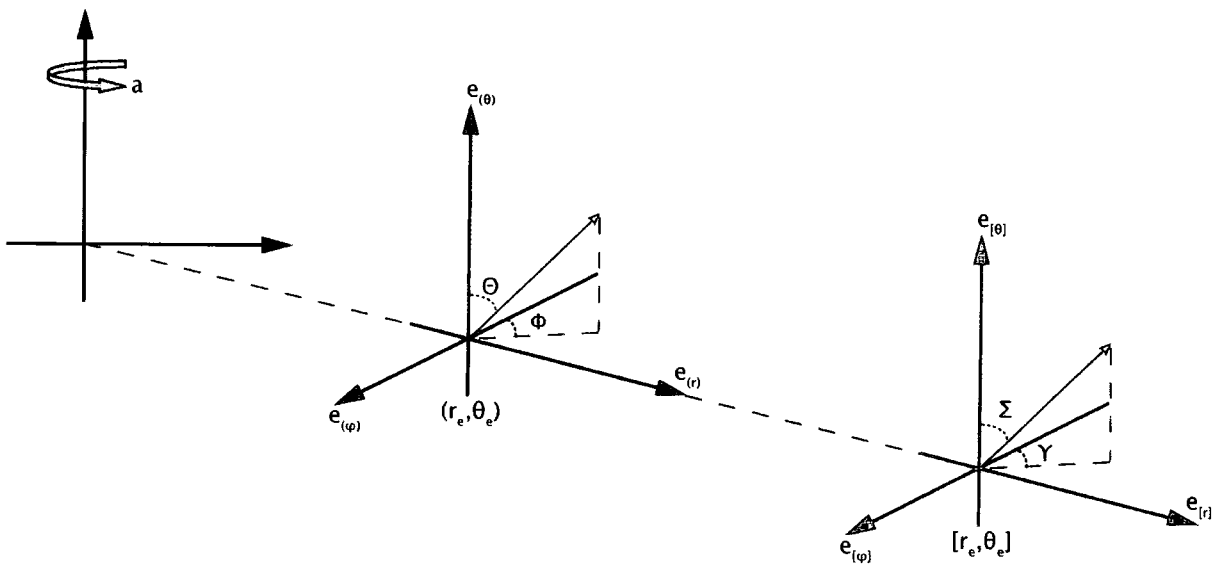

Figure 3.9: The co-ordinate system associated with the Local Disk Frame (LDF), moving with velocity u^{ϕ} (denoted by green lines) and its relation to the Locally Non-Rotating Frame (LNRF), which moves with velocity ω (denoted by blue lines). The LDF moves with respect to the LNRF with velocity $u^{(\phi)} = u^{\mu}e^{(\phi)}_{\mu}$. The basis vectors of the LDF can therefore be obtained via a simple Lorentz transformation, $e^{\sigma}_{[\beta]} = e^{\sigma}_{(\alpha)}\Lambda^{(\alpha)}_{[\beta]}$. The components of the photons 4-momentum in this frame are evaluated through $p_{[\mu]} = p_{\nu}e^{\nu}_{[\mu]}$. From these we can define the angles formed by the spatial components of p_{μ} with the basis vectors of the LDF through the relations $\cos\Sigma = p_{(\theta)}/p_{(t)}$, $\sin\Sigma\sin\Upsilon = p_{(r)}/p_{(t)}$, $\sin\Sigma\cos\Upsilon = \cos\Xi = p_{(\phi)}/p_{(t)}$.

As in the LNRF case, we define the angles that the photons four-momentum makes with the basis vectors of the LDF to be (see Figure 3.9):

$$\begin{aligned}
\cos\Sigma &= \frac{p_{[\theta]}}{p_{[t]}} = -\frac{e^{\mu_2}\sqrt{\Theta_{\lambda,q}(\theta)}}{\gamma e^{-\nu}\left(1-\lambda v^{\phi}\right)} \\
\sin\Sigma\sin\Upsilon &= \frac{p_{[r]}}{p_{[t]}} = -\frac{e^{\mu_1}\Delta^{-1}\sqrt{R_{\lambda,q}(r)}}{\gamma e^{-\nu}\left(1-\lambda v^{\phi}\right)} \\
\sin\Sigma\cos\Upsilon = \cos\Xi &= -\frac{p_{[\phi]}}{p_{[t]}} = \frac{e^{-\psi}\lambda[v^{(\phi)}\omega e^{\psi-\nu}+v^{(\phi)}+1]}{\gamma e^{-\nu}\left(1-\lambda v^{\phi}\right)}
\end{aligned} \tag{3.63}$$

Subsequent calculations of the spectral properties of accretion flows around rotating black holes will require us to determine the change in energy of a photon between the rest frame of the emitter and the rest frame of the observer. We characterise this change in energy using the redshift parameter, g:

$$g = \frac{E_{\text{observed}}}{E_{\text{emitted}}} = \frac{(p_{[t]})_{\text{observed}}}{(p_{[t]})_{\text{emitted}}} \tag{3.64}$$

In the case where the observer is located at radial infinity, their four-velocity takes the form $u^{\mu} = \left| \begin{array}{cccc} 1 & 0 & 0 & 0 \end{array} \right|$, the redshift parameter, g is expressed as:

$$g_{\infty} = \frac{E_{\text{observed}}}{E_{\text{emitted}}} = \frac{1}{\gamma e^{-\nu}\left(1-\lambda v^{\phi}\right)} \tag{3.65}$$

We can therefore express the photons constants of motion in terms of g_{∞} and $\cos\Theta$:

$$\lambda = \frac{1}{v^{\phi}}\left(1-\frac{e^{\nu}}{\gamma g}\right); \quad q = e^{2\mu_2}g^{-2}\cos^2\Sigma - \cos^2\theta\left[a^2 - \frac{\lambda^2}{\sin^2\theta}\right]; \tag{3.66}$$

3.4 Calculating Spectra in Strong Gravitational Fields

The discussion contained in this chapter thus far has been concentrated on the calculation of photon trajectories in curved spacetime and how physical quantities may be evaluated in the strong gravitational field of a rotating black hole. Whilst such discussions are interesting from a purely theoretical standpoint, we cannot compare these results directly with observations. Instead, we must combine our discussions to date into predictions that can be compared directly with observations. Current state-of-the-art observations can only provide us with *spectral* and *timing* information about the inner regions of the accretion flow, direct *imaging* remains some way off (see Chapter 5). The subsequent chapters of this work will focus on describing the combined effects of general relativity and the properties of the accretion flow on the observed spectra from accretion flows in strong gravity, in particular fluorescent Iron Kα profiles. Here, we describe the formalism that we have developed to perform these calculations.

Consider a detector with area dA_o, which is exposed to radiation for a time dt_o (where subscript o denotes evaluation in the frame of the detector). The amount of energy, dE_o, received by the detector is then proportional to $dA_o dt_o$, which we write as:

$$dE_o = F_o dA_o dt_o \tag{3.67}$$

Here, F_o is the constant of proportionality known as *flux* and has units of [Energy][Area]$^{-1}$ [Time]$^{-1}$. Flux measures the energy carried by all rays that pass through the detector, however, for our purposes it is necessary to introduce a rather more detailed description, where we consider the properties of a set of rays that differ infinitesimally. Choose a ray characteristic of the set and construct an infinitesimal area, dA_o, normal to the direction of the ray and consider rays within the set that fall within the infinitesimal solid angle, $d\Omega_o$ (see Figure 3.10, left-hand panel). The energy, dE_o crossing the area dA_o in a time dt_o in the frequency range $d\nu_o$ is then given by:

$$dE_o = I_o(\nu) dA_o dt_o d\Omega_o d\nu_o \tag{3.68}$$

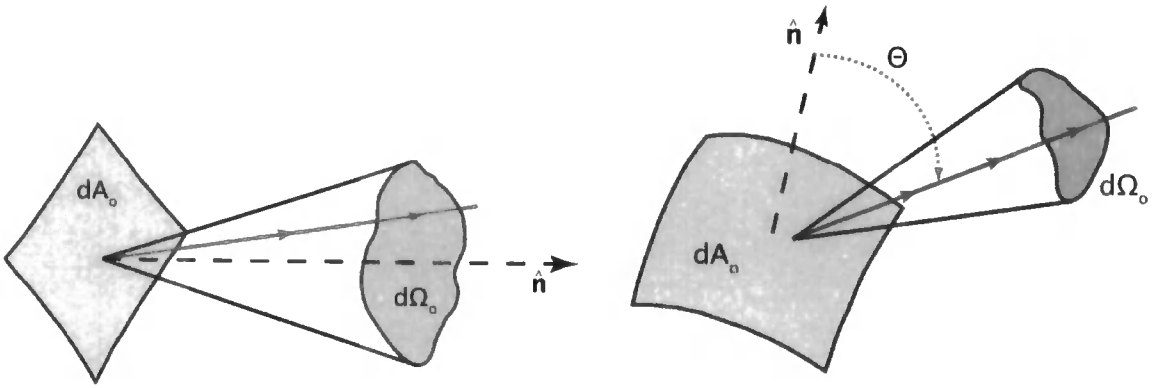

Figure 3.10: Geometry's for normally incident (left-hand panel) and obliquely incident rays (right-hand panel). Both panels adapted from Rybicki & Lightman (1979)

Here, $I_o(\nu)$ is the constant of proportionality known as the *specific intensity* and has units of [Energy][Area]$^{-1}$[Time]$^{-1}$[SolidAngle]$^{-1}$[Frequency]$^{-1}$.

Suppose now that the unit normal to the surface of the detector is orientated in some arbitrary direction and rays are incident on the detector from all directions (see Figure 3.10, right-hand panel). The *differential flux* received by the detector (normalised to the lowered effective area of the detector, $\cos\Theta dA$) is then defined to be:

$$dF_o(\nu_o) = I_o(\nu_o)\cos\Theta d\Omega_o \tag{3.69}$$

We therefore see that $dF_o(\nu_o)$ has units of [Energy][Area]$^{-1}$[Time]$^{-1}$[Frequency]$^{-1}$. From Quantum Mechanics, we know that $E = h\nu$, so we are able write the above in terms of the differential flux received in the energy range dE_o (different from that introduced in Eqns. 3.45 and 3.68).

$$dF_o\left(E_o\right) = I_o\left(E_o\right)\cos\Theta d\Omega_o \tag{3.70}$$

In the case where the observer is located at large distances from the hole, then photons arriving at the detector will be incident with $\cos\Theta$ = constant. We arbitrarily choose $\cos\Theta = 1$ and so:

$$dF_o\left(E_o\right) = I_o\left(E_o\right)d\Omega_o$$

This is the standard starting point for relativistic line calculations followed by (e.g. Cunningham, 1975; Fabian et al., 1989; Fanton et al., 1997), which defines an an infinitesimal amount of differential flux, dF_o observed at energy, E_o due to a patch on the disk which subtends a solid angle $d\Omega_o$ on the image of the disc at the observer (see Figure 3.11).

All of the quantities contained in Eqn. 3.70 are evaluated in the rest frame of the observer. However, descriptions of how energy is released within the accretion flow (see Section 2.4) are defined in the reference frame of the disk. We must therefore related the specific intensity measured by the observer, $I_o(E_o)$ to that measured in the rest frame of the emitting material, $I_e(E_e)$, which is accomplished by application of Liouville's theorem (Lindquist, 1966). Consider a distribution function, $f(x, p^\mu)$ describing the number, dN of particles crossing a volume element dV at x, whose four-momentum p^α occur within a corresponding element, dP in momentum space. The number of particles, dN is given by:

$$dN = f(x, p^\alpha)(-p^\alpha u_\alpha) dV dP \tag{3.71}$$

Transform to the co-moving, locally inertial frame at x such that:

$$dV = dxdydz; \quad dP = pdEd\Omega_o \tag{3.72}$$

In this frame, the number of particles, dN is therefore given by:

$$dN = f(x, p^\alpha) E p dV dE d\Omega_o \tag{3.73}$$

Classically, we have that (by definition) $dN = I_o(E_o) E^{-1} dV dE d\Omega$, from which we see that

$$f(x, p^\alpha) = \frac{I_o(E_o)}{E_o^2 p} = \frac{I_o(E_o)}{E_o^2 \sqrt{E_o^2 - m^2}} = \lim_{m \to 0} \frac{I_o(E_o)}{E_o^3} = \frac{I_o(\nu_o)}{\nu_o^3} \tag{3.74}$$

Therefore, since $F(x, p^\mu)$ is invariant, we therefore see that $E_o^{-3} I_o(E_o)$ is also conserved. We can therefore relate the specific intensity received by the observer to that emitted in the rest frame of the disc via:

$$\frac{I_o(E_o)}{E_o^3} = \frac{I_e(E_e)}{E_o^3} \quad \Rightarrow \quad I_o(E_o) = g^3 I_e(E_e) \tag{3.75}$$

Therefore:

$$dF_o\left(E_o\right) = g^3 I_e\left(E_e\right) d\Omega_o \tag{3.76}$$

For an emission line with rest energy E_{int}, then $I_e\left(E_e\right) = \varepsilon\left(r_e, \mu_e\right) \delta\left(E_e - E_{int}\right)$, where $\varepsilon\left(r_e, \mu_e\right)$ is the emissivity, which can be a function of the radius, r_e and angle, $\mu_e = \cos\Sigma$ at which the photon is emitted (see Figure 3.9). The infinitesimal flux becomes

$$dF_o\left(E_o\right) = g^4 \varepsilon\left(r_e, \mu_e\right) \delta\left(E_o - gE_{int}\right) d\Omega_o \tag{3.77}$$

The total flux can be obtained by integrating over all the entire image of the disk in the observers sky. We can write $d\Omega_o = r_o^{-2} d\alpha d\beta$ where α, β are the x, y coordinates of the image of the disc at the observer with coordinates (r_o, θ_o) (see Figure 3.11), such that

$$F_o\left(E_o\right) = \frac{1}{r_o^2} \int\int g^4 \varepsilon\left(r_e, \mu_e\right) \delta\left(E_o - gE_{int}\right) d\alpha d\beta \tag{3.78}$$

The α, β position of the image of the disc section is related to the conserved quantities, λ, q which describe the contributions to the photons angular momentum from the radial, polar and azimuthal directions (de Felice & Preti, 1999), via:

$$\alpha = -\frac{\lambda}{\sin\theta_o}; \quad \beta = \pm\sqrt{q + a^2 cos^2\theta_o - \lambda^2 \cot^2\theta_o} \tag{3.79}$$

For a thin, Keplerian disc, these constants of motion can be written in terms of the redshift factor of the photon, g and the radius of emission, r_e and angle of emission, μ_e of the photon (as previously defined):

$$\lambda = \frac{1}{v^\phi}\left(1 - \frac{e^\nu}{\gamma g}\right); \quad q = \frac{r_e^2 \mu_e^2}{g^2} \tag{3.80}$$

Here, v^ϕ describes the azimuthal velocity profile of the emitting region and $\gamma e^{-\nu}$ is the 'redshift function' (Fanton et al., 1997; Martocchia et al., 2000), which for a geometrically thin, Keplerian disc located in the equatorial plane are given by:

$$v^\phi = \frac{1}{a + \sqrt{r_e^3}}; \quad \gamma e^{-\nu} = \left[1 - \frac{2}{r_e}\left(1 - a\Omega\right)^2 - \left(r_e^2 + a^2\right)\Omega^2\right]^{-\frac{1}{2}} \tag{3.81}$$

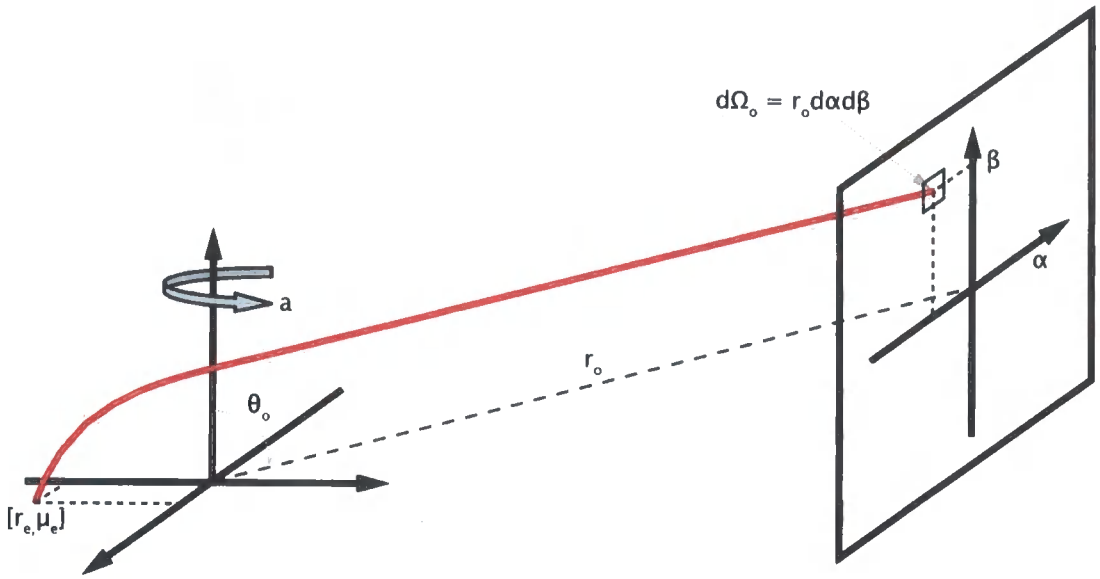

Figure 3.11: Diagram showing the link between the observers frame of reference and the global coordinate system defined by the black hole. Photons that are emitted from the disc at some distance r_e from the hole are seen at coordinates α, β on the image of the disc at the observer.

Thus the problem reduces to finding the area on the observers sky subtended by all parts of the disc which contribute to a given E_o.

The photons (null geodesics) that link the accretion disc with the observer can only be found by determining the full general relativistic light travel paths which link the disc to the observer. These null geodesics are given by solutions of the geodesic equations (Carter, 1968; Misner et al., 1973; Chandrasekhar, 1983), which can be obtained numerically (e.g. Karas et al., 1992), but can also be given in terms of analytic functions (Rauch & Blandford, 1994; Agol, 1997; Čadež et al., 1998), which enable them to be solved quickly and with arbitrary accuracy.

We develop a technique based solely on the image of the accretion disc in the α, β plane, which defines the flux received by the observer, similar to that employed by Čadež

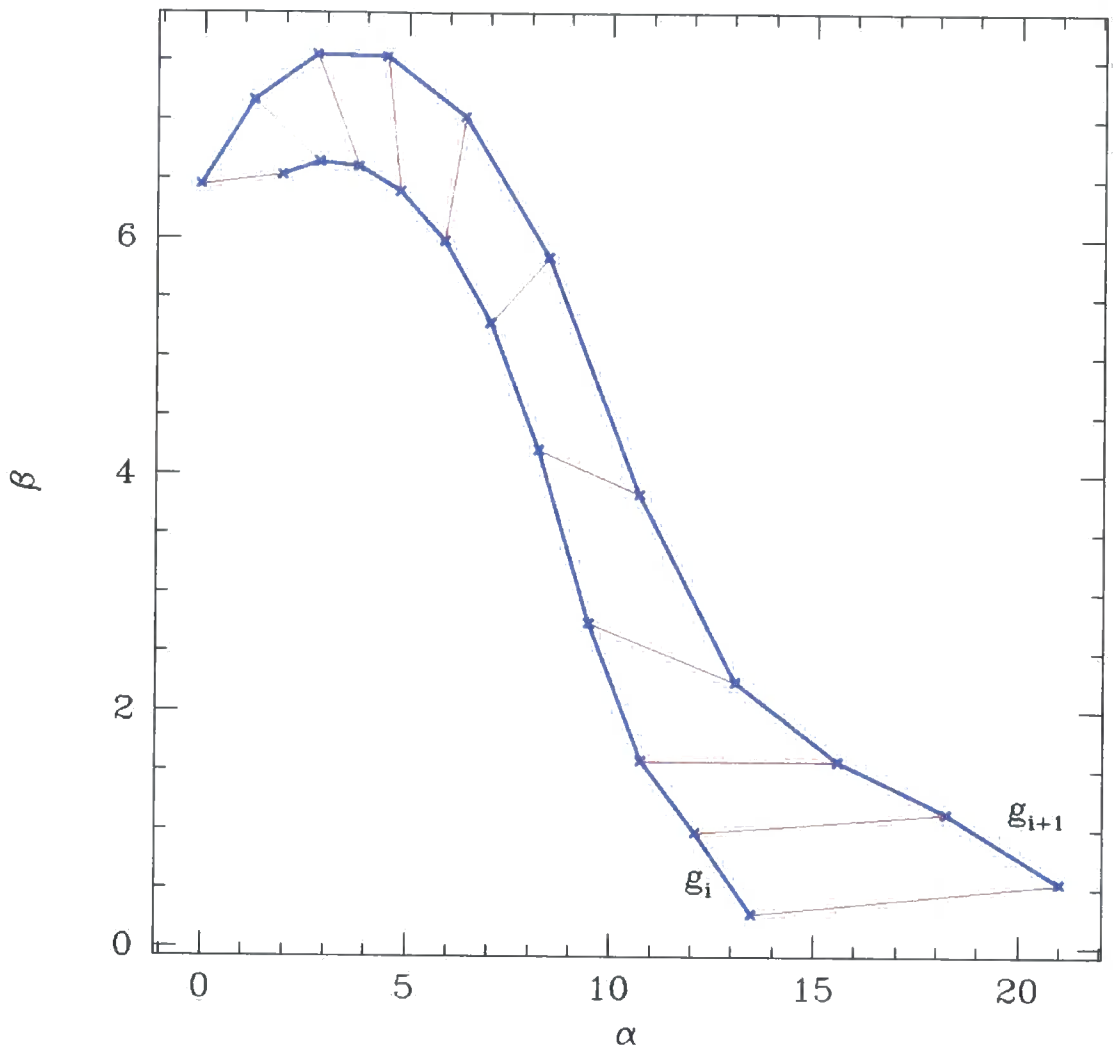

Figure 3.12: Heavy blue lines denote adjacent contours of constant redshift, $g_i < g_{i+1}$ on the observers sky (the α, β-plane) that define the area of the redshift bin $g = g_i + \frac{1}{2}(g_{i+1} - g_i)$ with width $dg = g_{i+1} - g_i$. Red narrow lines show examples of the divisions used to create a set of meshed trapezoids that enable the area of the redshift bin to be determined. For the purposes of clarity, this mesh is far coarser than that used in the calculations.

et al. (2003). This allows us to generate high resolution, accurate line profiles numerically while avoiding the issues surrounding the partial derivatives of the geodesic equations (Viergutz, 1993). We use the analytic solutions of the geodesic equations as tabulated by Rauch & Blandford (1994) to find the complete set of light travel paths that link the accretion disk and the observer at (r_o, θ_o). We sort these by redshift factor, and use adaptive griding to find the boundaries on the (α, β)-plane for all lines of constant g.

Two adjacent boundaries, g_i and g_{i+1}, therefore define the area of the redshift bin $g = g_i + \frac{1}{2}(g_{i+1} - g_i)$ with width $dg = g_{i+1} - g_i$ when projected onto the (α, β)- plane (as is shown in Figure 3.12). We can simply determine the area of this region by dividing it up into a set of tessellating trapezoids, as shown in Figure 3.12, the area of each of which can be determined by a simple geometric formula. The final area of the redshift bin is determined by summing together the contributions from all such trapezoids internal to (g_i, g_{i+1}). Each individual trapezoid is small, so that there is no significant change in r_e or μ_e (though this is not necessarily true across the total area $d\alpha d\beta$). The emissivity law can be convolved into the calculation using the emission coordinates at the centre of each trapezoid to weight its area before performing the summation over all trapezoids. This approach allows us to calculate line profiles at high spectral resolution on timescales of a few minutes on a 2GHz desktop PC.

We have extensively tested the routines that calculate the null geodesic paths against those supplied by Eric Agol (Agol, 1997) and have found them to be indistinguishable. We have also compared the line profiles generated by our code to those presented previously in the literature, in particular those generated from the codes described by Fanton et al. (1997); Dovčiak et al. (2004) and have again found them to be indistinguishable.

Chapter 4

Iron Line Profiles in Strong Gravity

Abstract

We present results from a new code which can accurately calculate the relativistic effects which distort the emission from an accretion disc around a black hole. We compare our results for a disk which extends from the innermost stable orbit to $20r_g$ in both Schwarzschild and maximal ($a = 0.998$) Kerr spacetimes with the two line profile codes which are on general release in the XSPEC spectral fitting package. These models generally give a very good description of the relativistic smearing of the line for this range of radii. However, these models have some limitations. In particular we show that the assumed form of the *angular* emissivity law (limb darkening or brightening) can make significant changes to the derived line profile where light bending is important. This is *always* the case for extreme Kerr spacetimes or high inclination systems, where the observed line is produced from a very large range of different emitted angles. In these situations the assumed angular emissivity can affect the derived *radial* emissivity. The line profile is not simply determined by the well defined (but numerically difficult) physical effects of strong gravity, but is also dependent on the poorly known astrophysics of the disc emission.

4.1 Introduction

Material in an accretion disk around a black hole is orbiting at high velocity, close to the speed of light, in a strong gravitational potential. Hence its emission is distorted by Doppler shifts, length contraction, time dilation, gravitational redshift and light bending. The combined impact of these special and general relativistic effects was first calculated in the now seminal paper of Cunningham (1975), where he used a *transfer function* to describe the relativistic effects. The observed spectrum from an accretion disc around a Kerr black hole is the convolution of this with the intrinsic disc continuum emission.

While such models have been used to try to determine the gravitational potential from the observed accretion disk spectra (e.g. Laor & Netzer, 1989; Ebisawa et al., 1991, 1993; Makishima et al., 2000; Gierliński et al., 2001) these attempts suffer from our limited knowledge of the spectral shape of the intrinsic accretion disk emission (see e.g. the review by Blaes, 2004). It is much easier to determine the relativistic effects from a *sharp* spectral feature, such as the iron fluorescence line expected from X-ray illumination of an accretion disc (Fabian et al., 1989). An originally narrow atomic transition is transformed into broad, skewed profile whose shape is given *directly* by the transfer function.

Observationally, evidence for a relativistically smeared iron line first came from the ASCA observation of the active galactic nuclei (AGN) MCG-6-30-15 (Tanaka et al., 1995). Further observations showed evidence for the line profile being so broad as to require a maximally spinning black hole (Iwasawa et al., 1996). More recent data from XMM are interpreted as showing that the line is even wider than expected from an extreme Kerr disk, requiring direct extraction of the spin energy from the central black hole as well as the immense gravitational potential (Wilms et al., 2001).

Such results are incredibly exciting, but X-ray spectral fitting is not entirely unambiguous. There is a complex reflected continuum as well as the line (Nayakshin et al., 2000; Ballantyne et al., 2001). For an ionised disk (as inferred for MCG-6-30-15) the current models in general use (`pexriv` in the XSPEC spectral fitting package) are prob-

ably highly incomplete (Ross et al., 1999). Complex ionised absorption also affects AGN spectra (e.g. Kaspi et al., 2002) and the illuminating continuum itself can have complex curvature rather than being a simple power law.

However, in MCG-6-30-15 these issues have been examined in detail, and the results on the dramatic line width appear robust (Fabian & Vaughan, 2003; Reynolds et al., 2004). Thus there is a clear requirement that the extreme relativistic effects are well modelled. There are two models which are currently widely available to the observational community, within the `XSPEC` spectral fitting package, `diskline` (based on Fabian et al., 1989) and `laor` (Laor, 1991). The analytic `diskline` code models the line profile from an accretion disc around a Schwarzschild black hole (so of course cannot be used to describe the effects in a Kerr geometry). Also, it does not include the effects of light bending (although Fabian et al., 1989, outline a scheme for incorporating this) and hence does not accurately calculate all the relativistic effects for $r < 20r_g$ (where $r_g = GM/c^2$). By contrast, the `laor` model numerically calculates the line profile including light bending for an extreme Kerr black hole, but uses a rather small set of tabulated transfer functions which limit its resolution and accuracy (see Section 3.3.3).

While there are other relativistic codes in the literature which do not suffer from these limitations, these are not generally readily and/or easily available for observers to use. There is a clear need for a fast, accurate, high resolution code which can be used to fit data from the next generation of satellites. In this paper we describe our new code for computing the relativistic iron line profile in both the Schwarzschild and Kerr metrics. We compare this with the `diskline` and `laor` models in `XSPEC` for discs which extend down to the last stable orbit in their respective spacetimes, and highlight both the strengths and limitations of these previous models.

4.2 Iron Kα Diagnostics of Thin, Keplerian Accretion Disks

4.2.1 Introduction

We have taken a disc from r_{ms} to $r_{max} = 20r_g$ (beyond which strong gravitational effects become of diminishing importance) for both the Schwarzschild ($a = 0$, $r_{ms} = 6r_g$) and maximal Kerr ($a = 0.998$, $r_{ms} = 1.235r_g$) cases for $\theta_o = 5°, 30°, 60°$ and $85°$.

We first consider the extent of light bending effects in a Schwarzschild spacetime. Figure 4.1 shows the three-dimensional surface in (μ_e, r_e, g) for the complete set of light travel paths connecting the accretion disc to the observer. There is a considerable range of μ_e contributing to the observed emission at all inclinations. For low inclinations the effect is fairly uniform, with each radius contributing a similar range in μ_e, but with a systematic shift to larger emission angles (smaller μ_e) with smaller radii. By contrast, at higher inclinations the light bending is strong enough to gravitationally lens the far side of the disc. This leads to a much larger range of μ_e which contribute to the disc image at small radii. In all cases, light bending means there *is* a range of μ_e which contribute to the observed disc emission, so that in general, the line profile *will* depend on the angular distribution of the emitted flux.

Fig. 4.2 shows the corresponding surfaces for the extreme Kerr case. The disc now extends down to $1.235r_g$, far closer to the corresponding event horizon than in the Schwarzschild case. This introduces a greater complexity to the geodesic surfaces. The range of emission angles is from zero to unity in all cases, including the nearly face on disc at 5°, which has important consequences for the calculation of the line profile.

To construct the relativistic line profile, we map these surfaces on to the (α, β) plane as discussed in the previous section, forming images of the accretion disc, as have been previously calculated by e.g. Bardeen & Cunningham (1973); Luminet (1979); Hollywood & Melia (1997); Fanton et al. (1997); Falcke et al. (2000). In Figure 4.3 we present images

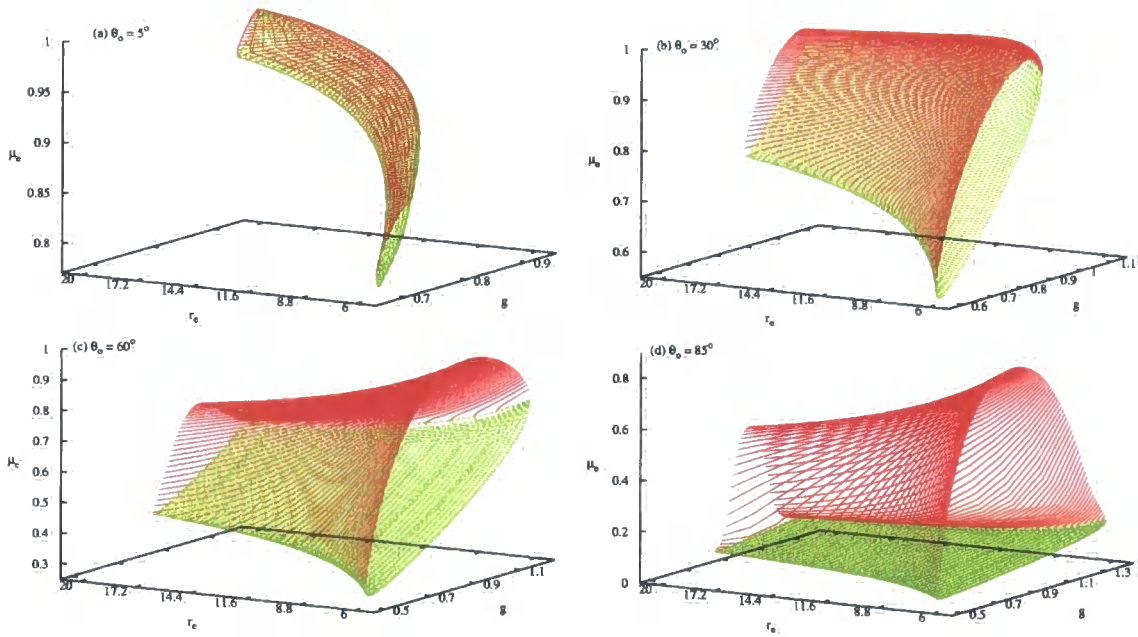

Figure 4.1: Surfaces in the (μ_e, r_e, g) parameter space describing geodesics that reach an observer at a given inclination for a standard accretion disk around a Schwarzschild black hole. Notice that, for every (r_e, g) pair, there are two geodesics that reach any given observer, corresponding respectively to geodesics that are emitted from the side of the disc closest to the observer (lower surface) and geodesics that are emitted from the opposite side of the disc to the observer (upper surface). These are the two geodesics referred to by Cunningham (1975).

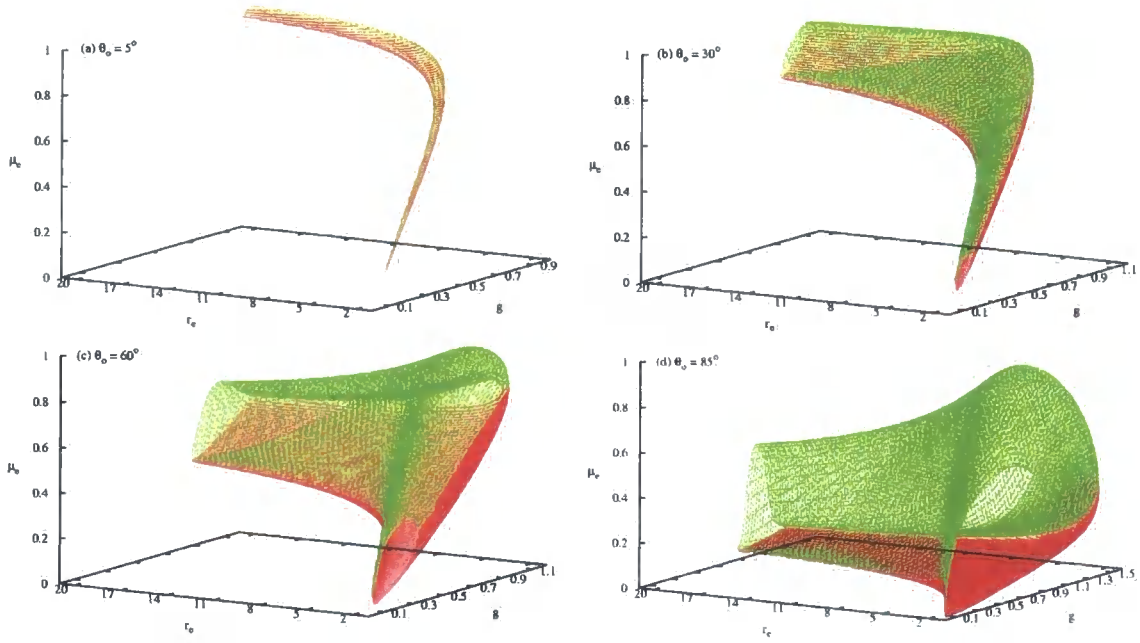

Figure 4.2: As in Figure 4.1 for a maximal ($a = 0.998$) Kerr black hole. These surfaces are exhibit a far greater complexity than those in the Schwarzschild case. The range of accessible redshift is increased for a given disc-observer system, whilst the range of emission angles is from zero to unity for all inclinations.

of the Schwarzschild disc for the 30° (top row) and $\theta_o = 85°$ (bottom row) cases (others provide no new information qualitatively). Images on the left-hand side of the figure are coloured by values of the redshift factor, g, as defined by the scale at the top of each image. By contrast, images on the right-hand side of the figure has each redshift bin coloured by its area on the observers sky, i.e. $g^4 d\alpha d\beta$, again with the scale defined at the top of each image. Strong gravitational lensing effects can now clearly be seen in the high inclination images. Photons from the far side of the disc pass close to the black hole, so the disc image is strongly distorted (Matt et al., 1993b; Zakharov & Repin, 2003). Since the area of the disc is magnified, its contribution to the observed flux should be large. However, we stress that the low inclination images *are* also affected by light bending (see Figure 4.1a and 4.2a), though they are not magnified by gravitational lensing.

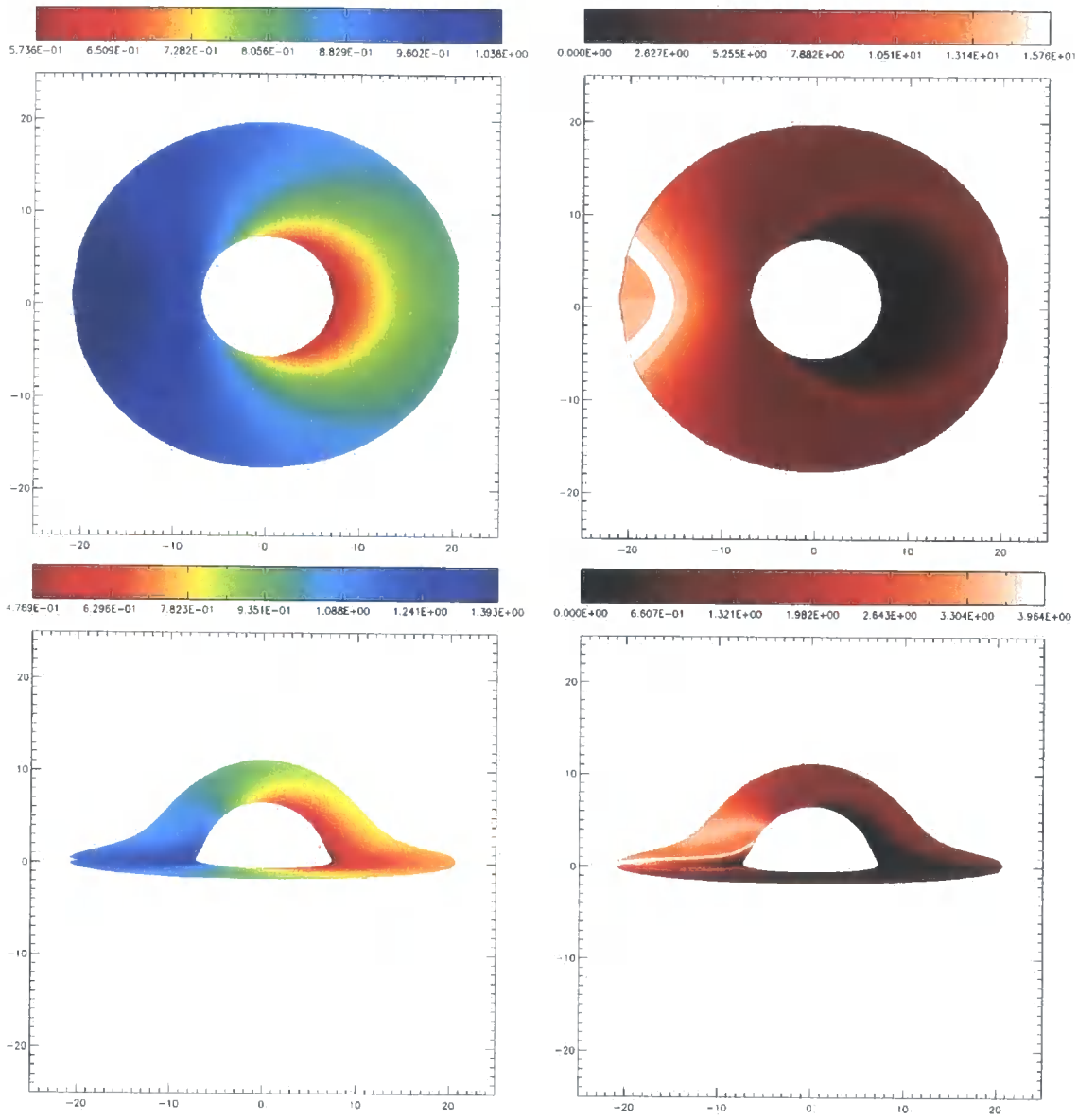

Figure 4.3: Redshift images (left hand panels) and flux image (right hand panels) of the accretion disc on the (α, β) plane for a Schwarzschild black hole, for the $\theta_o = 30°$ (top row) and $\theta_o = 85°$ (bottom row) cases. Redshift images are coloured by the associated values of g as measured by the distant observer. Flux images coloured by the $g^4 r_o^2 d\Xi = g^4 d\alpha d\beta$ component of the relativistic line profile. Note the appearance of strong light bending effects in the $\theta_o = 85°$ case, as previously reported by Matt et al. (1993b); Zakharov & Repin (2003).

The form of the line profile is now determined from the flux image (representing the effects of strong gravity), together with the assumed form for the emissivity (determined by the energy release and radiative transfer processes), which is generally taken as (ignoring azimuthal dependence):

$$\varepsilon\left(r_e, \mu_e\right) = \epsilon\left(r_e\right) f\left(\mu_e\right) \tag{4.1}$$

While the flux image is a difficult numerical problem, it depends on well known *physics*. By contrast, the emissivity laws considered have rather simple forms, but are determined by the poorly known *astrophysics* of the disc. Of course, there are many other outstanding theoretical issues that can produce a substantial impact on the line profile, including (but not limited to) returning radiation or light bending that can enhance the emissivity of the inner part of the disc (Cunningham, 1975; Laor et al., 1990; Martocchia et al., 2000), emission from the plunging region (Reynolds & Begelman, 1997) and azimuthal dependence of the emissivity (Čadež et al., 2003; Karas et al., 2001). However, these are outside the scope of the current work.

4.2.2 Comparison with the Diskline Model

The `diskline` code assumes a Schwarzschild metric ($a = 0$) and additionally that light travels in straight lines (so the angular emissivity term is irrelevant). In its `XSPEC` implementation it allows both arbitrary power law $\epsilon\left(r_e\right) \propto r^q$ and point source illumination. However, its analytic structure means that any radial emissivity law is easy to incorporate. We choose to use $q = -3$, as this is approximately the form of the gravitational energy release per unit disc area (see e.g. Życki et al., 1999).

Figure 4.4 shows our line profiles assuming $f(\mu_e) = 1$ (no angular dependence of the emissivity) compared with those from the `diskline` code. We see that our new model matches very closely to the `XSPEC diskline` model for a nearly face on disk. Whilst the key difference between our model and `diskline` is the inclusion of light-bending effects,

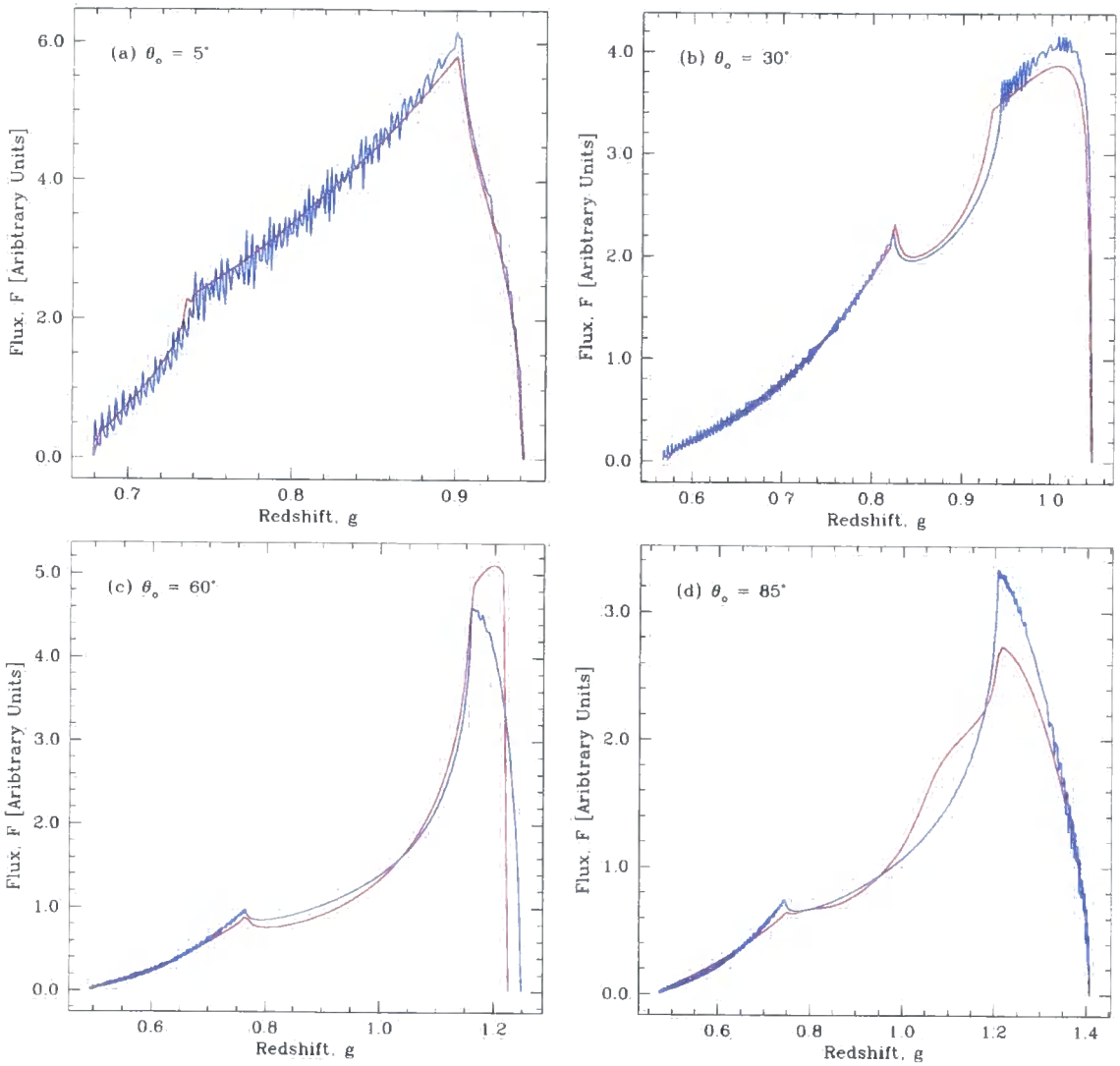

Figure 4.4: Comparison of the relativistic line profile computed by our model (red solid line) with that computed by the **XSPEC diskline** model (blue dashed line) for $\epsilon(r_e) \propto r^{-3}$ and $f(\mu_e) = 1$. At inclinations of $< 30°$, the profiles match to within $\sim 10\%$, but the increasing importance of light bending (which is not included in the **diskline** code) gives a 40% discrepancy in the profile shapes for inclinations $> 60°$. In this and all subsequent figures the line profiles are normalised such that they contain one photon, and all our results are unsmoothed.

the impact of this is small at low inclinations if there is no angular dependence to the emissivity (but see Section 3.4).

By contrast, at high inclinations, light bending not only means that the line is formed from many different μ_e, but gravitational lensing enhances the flux from the far side of the disc. This lensing effect gives clear differences between our model and `diskline`. The lensing magnifies the image of the far side of the disc, which has velocity mostly tangential to the line of sight, so is not strongly Doppler shifted. This boosts the line profile at $g \sim 1$ (see Matt et al., 1993b). Since the line profiles are all normalised to a single photon, then this also makes the blue peak smaller.

In summary, the `diskline` model as incorporated into XSPEC produces line profiles which are accurate to $\sim 10\%$ for inclinations of less than 30°. Obviously, if the inner disc edge $r_{min} > r_{ms}$ then the light bending effects become correspondingly smaller and the match between the two codes becomes even closer. At higher inclinations the differences between `diskline` and our code become larger due to the effects of gravitational lensing, which leads to an effective redistribution in flux between the blue peak and the centre of the line compared to that predicted from straight light travel paths.

4.2.3 Comparison with the Laor Model

By contrast, the `laor` code describes the line shape expected in the maximal Kerr case, assuming a standard limb darkening law $f(\mu_e) \propto (1 + 2.06\mu_e)$. The code is based on a series of photon trajectory calculations, where the disk is split up into a set of rings of width dr_e at r_e. Each part of the ring radiates with total emissivity (radial plus angular) given simply by the limb darkening law (i.e. no radial dependence, $q = 0$) and the line profile from that ring is built up from many light travel paths which connect the disc to the observer. This produces a series of *transfer functions* $T(r_e, E_o - gE_{int})$ at each radius, analogous to Figure 4.3a–d but including the limb darkening law. These tabulated transfer functions are read by the `laor` code in XSPEC and used to build a total line profile for

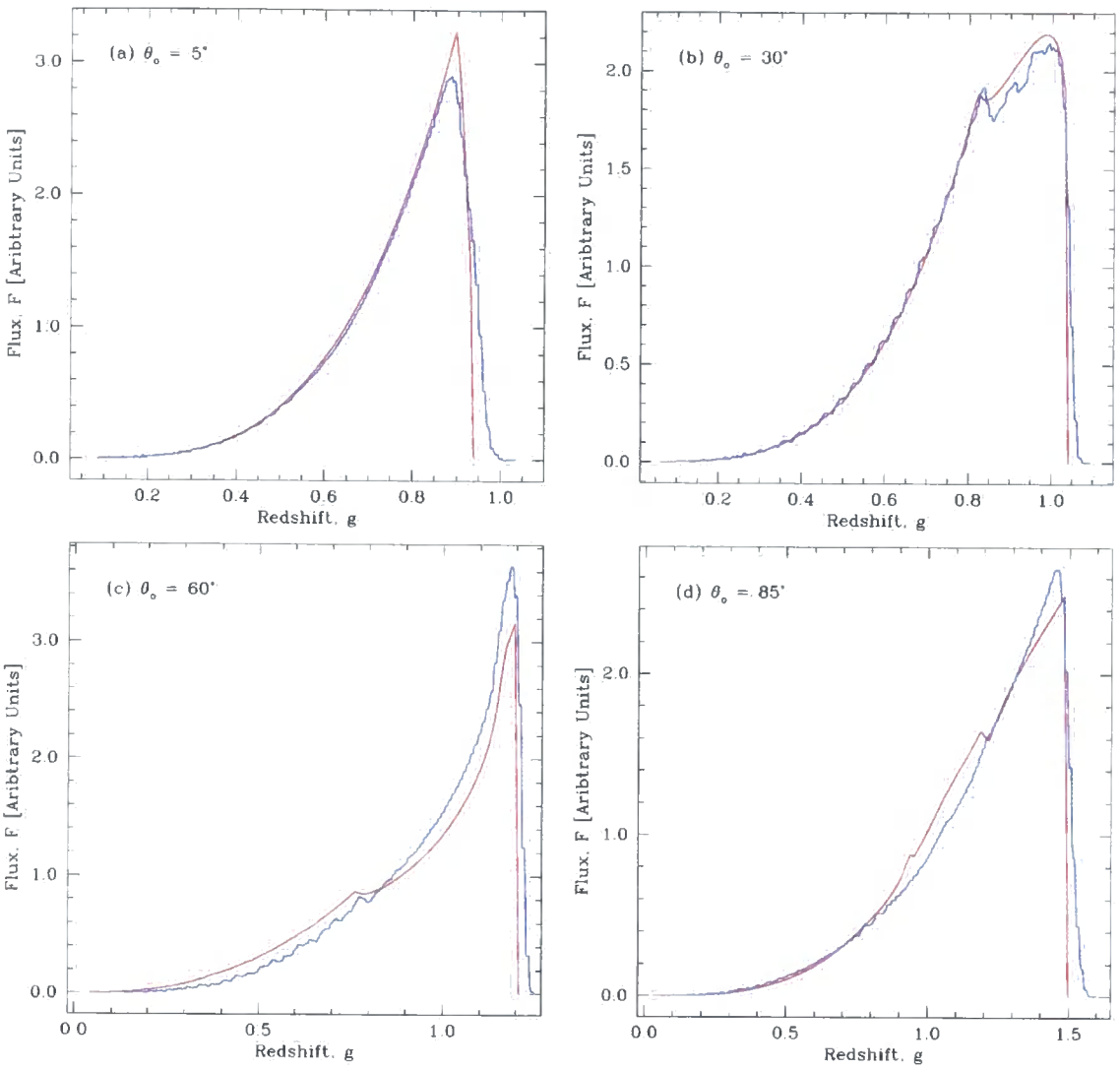

Figure 4.5: Comparison of the relativistic line profile computed by our model (red solid line) with that computed by the `XSPEC laor` model (blue dashed line) for $\epsilon(r_e) \propto r^{-3}$ and $f(\mu_e) \propto (1 + 2.06\mu_e)$. The profiles produced by the two models match to within $5 - 10\%$.

any given radial emissivity:

$$F_o(E_o) = \int \varepsilon(r_e) T(r_e, E_o - gE_{int}) r_e dr_e dg \tag{4.2}$$

We compare this with our code, using a $q = -3$ emissivity for both as in the `diskline` comparisons above. We include the same limb darkening law as used by `laor` and the results (Figure 4.5) show that the overall match between our code and `laor` is good to $\sim 5 - 10\%$.

4.3 The Role of the Disk Inner Edge and Inclination of the Observer

The greatest shortcoming of the currently available relativistic line models for `XSPEC` is that they only allow the treatment of either Schwarzschild (the `diskline` model) or maximal Kerr (the `laor` model) black holes. Our model is capable of calculating the relativistic line profile for arbitrarily spinning black holes and so removes this limitation.

The principle effect of changing black hole spin is alter the value of the marginally stable orbit, $r_{ms}(a)$, in particular, the higher the black hole spin, the closer this orbit is to the event horizon, $r_h(a)$ (in terms of co-ordinate distance, see e.g. Bardeen et al., 1972). In the standard relativistic accretion disk models, the disk extends down to this orbit (Page & Thorne, 1974), so if we are able to infer the location of the inner edge of the accretion disk, then in principle (assuming that the inner edge truncates at $r_{ms}(a)$), we can determine the spin parameter of the central black hole (see Section 2.5).

In terms of the relativistic line profile, Laor (1991) demonstrated that the principle effect of considering a maximally rotating black hole was the addition of a low energy tail to the line in comparison to the Schwarzschild case, as can be seen by comparison of Figures 4.4 and 4.5. In Figure 4.6 we show maps of the relativistic line profile for arbitrary black hole spin, which we denote using the associated value of $r_{ms}(a)$ for the

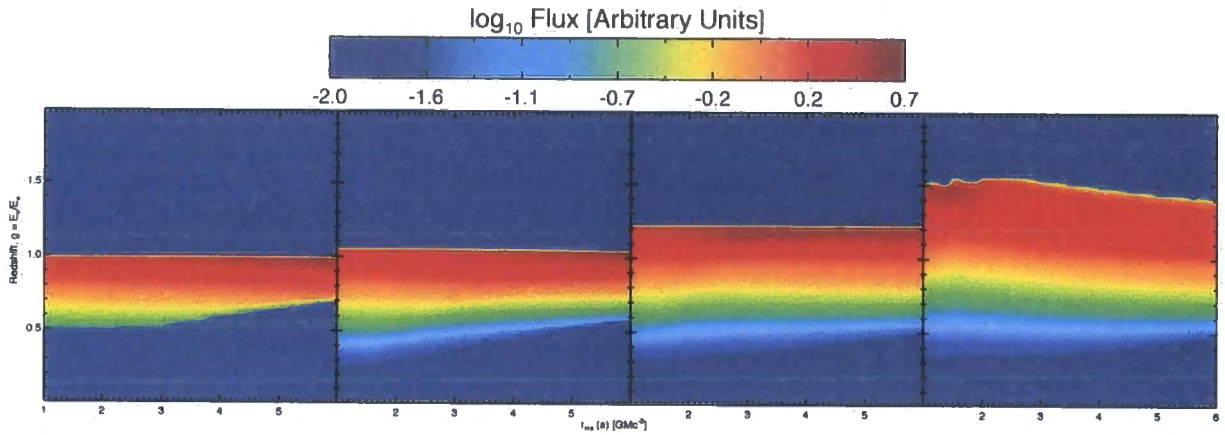

Figure 4.6: Maps of the relativistic line profile for arbitrarily spinning black holes, as denoted by the marginally stable orbit, $r_{ms}(a)$. From left to right, we show maps associated with $\theta_o = 5°, 30°, 60°, 85°$. The outer edge of the disk is taken to be at $100r_g$ in all cases and we have taken $\epsilon(r_e) \propto r^{-3}$, $f(\mu_e) = 1$. Each line profile in the map (corresponding to a slice along constant $r_{ms}(a)$ is normalised such that it contains one photon. For inclinations $\lesssim 60°$, the lower limit of the line shows a clear correlation with r_{ms} and hence is anti-correlated with spin, whereas the upper limit of the line is approximately independent of r_{ms}. For inclinations $\gtrsim 60°$, this dependence is complicated by the effects of gravitational lensing.

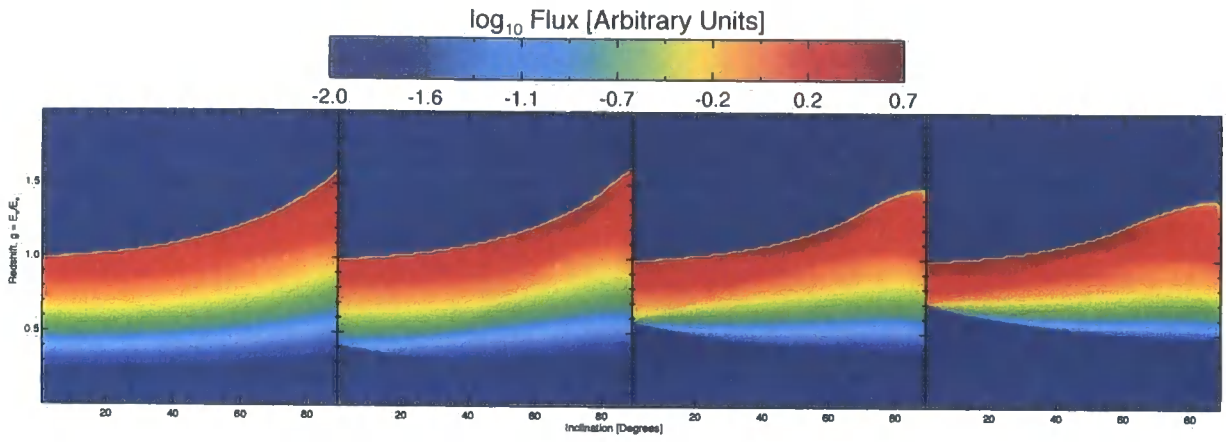

Figure 4.7: Maps of the relativistic line profile for distant observers with arbitrary inclination. From left to right, we show maps associated with $r_{ms} = 1, 2, 4, 6r_g$ ($a = 1.0, 0.94, 0.56, 0.0$). The inner and outer edges of the disk are taken to be at $r_{ms}(a)$ and $100r_g$ in all cases and we have taken $\epsilon(r_e) \propto r^{-3}$, $f(\mu_e) = 1$. Each line profile in the map (corresponding to a slice along constant θ_o is normalised such that it contains one photon. The lines become broader as the observer approaches the equatorial plane, independent of spin. However, the details of this dependence are markedly more complex for the slower rotating black holes, due to the effects of gravitational lensing.

four inclinations shown in Figures 4.4, 4.5. For a given inclination, the lower edge of the line shows a strong correlation with r_{ms} (and hence is anti-correlated with black hole spin) for inclinations $\lesssim 60°$, whilst at inclinations $\gtrsim 60°$ this dependence is far less pronounced. Generally, for the standard relativistic accretion disk model, we associate broader lines with faster rotating black holes.

It is interesting to note however that the upper edge of the lines shown in Figure 4.6 is approximately *independent* of spin, again for inclinations $\lesssim 60°$. In Figure 4.7, we show maps of the relativistic line profile for distant observers with arbitrary inclination for four selected black hole spins corresponding to $r_{ms} = 1, 2, 4, 6r_g$ ($a = 1.0, 0.94, 0.56, 0.0$). From these maps, it is clear that the dependence of the line shape on inclination shows a marked

difference for the rapidly rotating holes in comparison to the slowly rotating holes. For the rapidly rotating holes, the lower edge of the line is approximately independent of inclination, whilst the upper edge exhibits a power law like behaviour. For these holes, the internal shape of the line is roughly independent of spin, with a strong concentration of flux in the blue wing of the line, approximately independent of inclination (i.e. the distinctive triangular shape exhibited by the lines in Figure 4.5).

However, the behaviour of the lines associated with the slowly rotating holes is more complex. Here, the lower edge of the line exhibits a marked decrease with increasing inclination, whilst the upper edge takes the form of a modified power law. In these cases, the internal shape of the line is determined by both the radial emissivity law and gravitational lensing effects. This is in contrast to the rapidly rotating cases, where the radial emissivity law strongly weights the emission to the very inner regions of the disk ($\lesssim 6r_g$). All of the flux that is emitted in this region is subject to strong lensing effects in its transit to the observer (Laor, 1991) and hence we obtain the characteristic wedge shape. However, for the slowly rotating black holes, emission is only possible from regions where there is a strong dependence of gravitational lensing on radius and hence the shape of the line is strongly modified.

4.4 The Role of the Angular Emissivity and Black Hole Spin

The effect of applying a radial emissivity is straightforward. The transfer function describing all the relativistic effects from a given radial ring of the disc is unaffected, so the effect is simply to change the weighting of the line profile from each radial ring of the disc.

By contrast, the effect of the angular distribution is far more subtle. A given radial ring on the disc can contribute to the line profile from a range of emission angles (see Figures 4.1, 4.2). The relative weighting of these is determined by the angular emissivity, so it forms part of the calculation of the transfer function itself.

Different angular emissivity laws can have striking effects on the form of the relativistic line profile, which we illustrate in Fig. 4.8 (left-hand panel) for a maximal Kerr geometry (a=0.998) with the disc extending (as previously) from $1.235 - 20r_g$ and $\theta_o = 30°$. The line profiles here all implement the standard radial emissivity law of r^{-3}. However, we now compare a range of angular emissivity laws, these being (from top to bottom at the blue peak in Fig. 4.8) the standard limb darkening law (as discussed in Section 4.2.3), followed by the constant angular emissivity case (as used in `diskline`, see Section 4.2.2). An ionised disc could also be limb *brightened*, with the probable limiting case of $f(\mu) \propto 1/\mu$ as expected from optically thin material, shown as the bottom line in Fig. 4.8 (left-hand panel). There is a $\sim 35\%$ difference in the height of the blue peak depending of the form of the angular emissivity used.

However, such a limited range of radii is probably not very realistic. The disc should extend out to much greater distances from the black hole, where the relativistic effects (including light bending) are less extreme. However, realistic emissivities strongly weight the contribution from the innermost regions, so the effective dilution of the relativistic effects by including the outer disc is not overwhelming. Fig. 4.8 (centre panel) shows the line profiles generated using the same angular emissivity laws for a disc extending

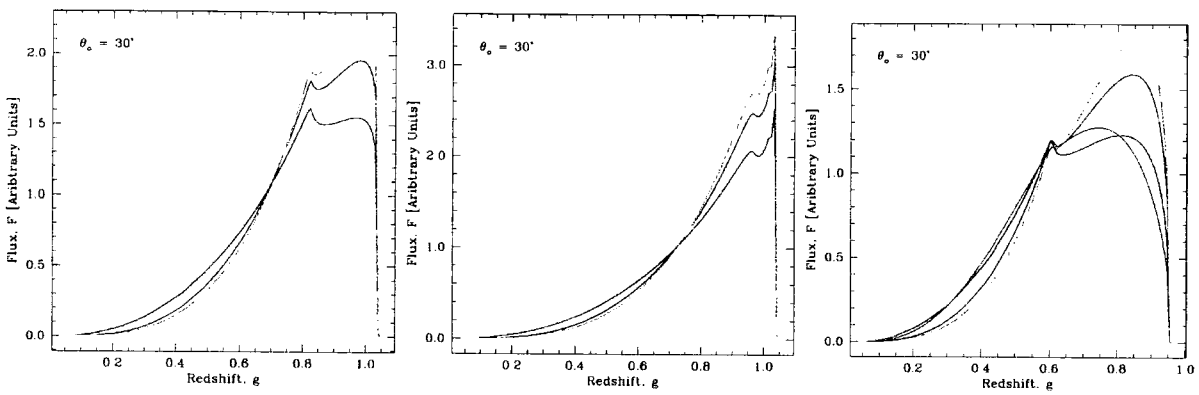

Figure 4.8: Comparison of the relativistic line profiles generated by our model with (a) $\epsilon(r_e) \propto r_e^{-3}$, $f(\mu_e) = 1$ (red lines), (b) $\epsilon(r_e) \propto r_e^{-3}$, $f(\mu_e) \propto \mu_e^{-1}$ (blue lines), (c) $\epsilon(r_e) \propto r_e^{-3}$, $f(\mu_e) \propto (1 + 2.06\mu_e)$ (green lines) for a maximal Kerr black hole with the disc extending from $1.235 - 20r_g$ (left-hand panel), $1.235 - 400r_g$ (centre panel) and $1.235 - 6r_g$ (right-hand panel). In the left-hand panel, the relative height of the blue wing changes by $\sim 35\%$ for different angular emissivity laws, anti-correlated with the slope of the red wing. For the more extended disk shown in the centre panel, there is still a $\sim 25\%$ change in the blue wing height and significant change in red wing slope for the different angular emissivities, despite the inclusion of the outer disc. Finally, in the right-hand panel, the additional magenta line is for a limb darkened angular emissivity with more centrally concentrated radial emissivity, $\propto r_e^{-4.5}$. This is very similar to the blue line profile derived from a very different radial emissivity, $\propto r_e^{-3}$, with a limb brightened angular emissivity.

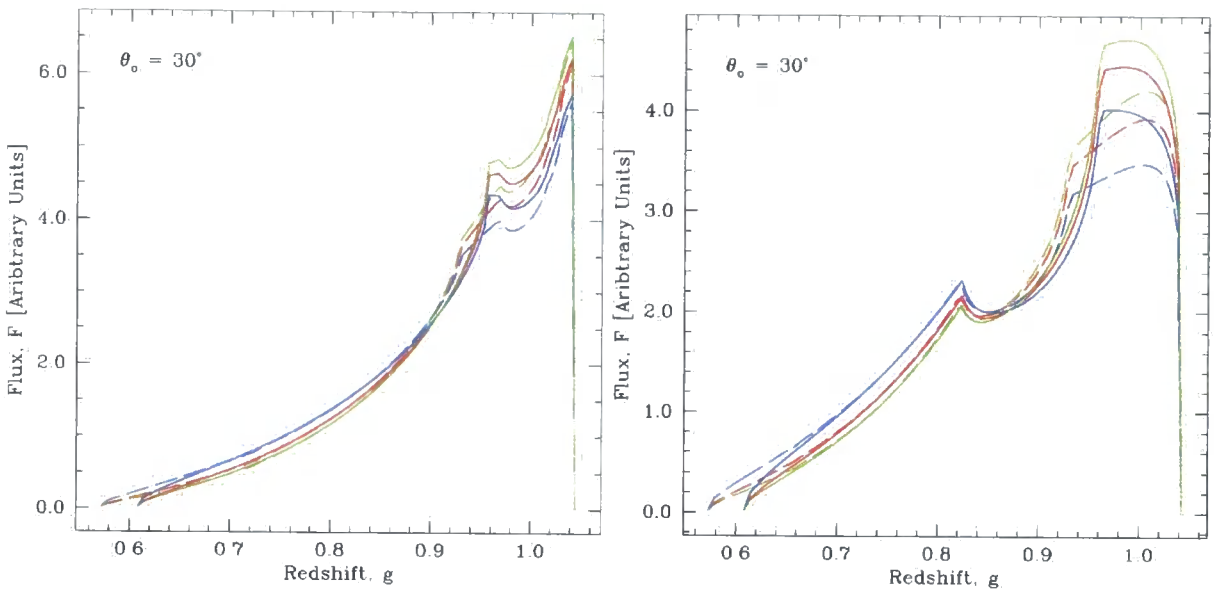

Figure 4.9: As in Fig. 4.8 but with the disc extending from $6 - 400r_g$ (left-hand panel) and $6 - 20r_g$ (right-hand panel) in a maximal Kerr (solid line) and Schwarzschild (dashed line) spacetime. In the left-hand panel, the differences between the line profiles produced for the same sized disc in different assumed spacetimes is of order $\sim$ 5% for a given angular emissivity. The effect of changing the angular emissivity is also similarly small ($\sim 5 - 10\%$). This contrasts with the much larger effects seen in the extreme Kerr metric for a disc extending down to $1.235r_g$, where lightbending is much more important (Fig. 4.8). In the right-hand panel, the differences are now of order $15 - 20\%$.

from $1.235 - 400r_g$, again with $\theta_o = 30°$. There are still significant differences in the line profiles, with a $\sim 25\%$ difference in the height of the blue peak while the red wing slope changes from $F_o(E_o) \propto E_o^{3.5}$ (limb darkened) to $\propto E_o^{2.5}$ (limb brightened).

Despite the expectation of an extended disc, some recent observational studies (e.g. Reynolds et al., 2004) have tentatively suggested that the disc is very small, from $\sim 1.235 - 6r_g$. This enhances the importance of light bending. Fig. 4.8 (right-hand panel) shows the line profiles for a disc extending from 1.235–$6r_g$, using the different angular emissivity described in the preceding discussion. The blue peak height differences are $\sim 40\%$, and the red wing slopes are different. For comparison we also show a limb darkened profile obtained from a very different *radial* emissivity of $r^{-4.5}$. This is very similar to the extreme limb brightened profile obtained from the r^{-3} radial weighting. We caution that uncertainties in the angular distribution of the line emissivity can change the expected line profile due to light bending effects even at low/moderate inclinations, and that this can affect the derived radial emissivity. This has important consequences for interpretation of the highly broadened lines observed in MCG-6-30-15, in particular conclusions regarding extraction of spin energy from the black hole.

Currently, the only available models in `XSPEC` have either zero or maximal spin. A zeroth order approximation to spacetimes with different spins is to use the maximal Kerr results but with a disc with inner radius given by the minimum stable orbit for the required value of a (e.g. Laor, 1991). We test this for the most extreme case of $a = 0$ modelled by a maximal Kerr spacetime with $r_{min} = 6r_g$. Fig. 4.9 (left-hand panel) compares this with a true Schwarzschild calculation for a disc extending from $6 - 400r_g$ with $\theta_o = 30°$ for a range of angular emissivities. The differences between the spacetimes (for a given angular emissivity) are at most $\sim 5\%$. This is roughly on the same order as the effect of changing the angular emissivity, which is much reduced here compared to Fig. 4.8 (left-hand panel) due to the larger r_{min}. Assumptions about both spin and angular emissivity become somewhat more important for smaller outer disc radii. Fig. 4.9 (right-hand panel)

shows this for a disc between $6 - 20r_g$ (directly comparable to Fig. 4.4).

4.5 Conclusions

Recent observational studies have provided evidence for highly broadened fluorescent iron Kα lines. While there are a variety of line profiles seen (e.g. Lubiński & Zdziarski, 2001), there are some objects where the line implies that there is material down to the last stable orbit in a maximally spinning Kerr spacetime (most notably MCG-6-30-15: Wilms et al., 2001; Reynolds et al., 2004). However, the strong gravity codes generally used to model these effects are now over a decade old. Increased computer power means that it is now possible to improve on these models. We describe our new code to calculate these effects, which uses uses fully adaptive gridding to map the image of the disc at the observer using the analytic solutions of the light travel paths. This is a very general approach, so the code can easily be modified to incorporate different emission geometries.

We compare the results of our new code with those from `diskline` and `laor` (publicly available in the XSPEC spectral fitting package) for Schwarzschild and extreme Kerr spacetimes. These previous models are accurate to $\sim 10\%$ with realistic ($\propto r^{-3}$) radial emissivities. However, they make specific assumptions regarding the angular dependence of the emitted flux, which may or may not be valid. Light bending is *always* important for a disc which extends down below $20r_g$, in that the image of the disc at the observer *always* consists of a range of different emission angles. This can produce significant changes to the derived line profile, especially in extreme Kerr spacetimes. Whilst calculating strong gravitational effects is a difficult numerical problem, the underlying physics is well known. By contrast, the *angular* emissivity is an astrophysical problem, and is not at all well known as it depends on the ionisation state of the disc as a function both of height and radius. Before we can use the line profiles to provide a sensitive test General Relativity and probe the underlying physics, we will need to have a much better understanding of the astrophysics of accretion.

The results of the code are available as both a convolution and an additive model in the XSPEC spectral fitting package. Principle features include the ability to fit to arbitrary black hole spin, both inner and outer disk radius along with allowing arbitrary angular and radial emissivities to be applied. Further information is available from the model webpage.

Chapter 5

Extreme Gravitational Lensing near Rotating Black Holes

Abstract

We apply the strong gravity code described in Chapter 3 of the work to explore both the imaging and spectral properties of photons emitted from an accretion disc which perform multiple orbits of the central mass before escaping to infinity. Viewed at large inclinations, these higher order photons contribute $\sim 20\%$ of the total luminosity of the system for a Schwarzschild hole, whilst for an extreme Kerr black hole this fraction rises to $\sim 60\%$. In more realistic models these photons will be re-absorbed by the disc at large distances from the hole, but this returning radiation could provide a physical mechanism to resolve the discrepancy between the predicted and observed optical/UV colours in AGN. Conversely, at low inclinations, higher order images re-intercept the disc plane close to the black hole, so need not be absorbed by the disc if this is within the plunging region. These photons form a bright ring carrying approximately 10% of the total disc luminosity for a Schwarzschild black hole. The spatial separation between the inner edge of the disc and the ring is similar to the size of the event horizon. This is resolvable for supermassive black holes with proposed X-ray interferometry missions such as MAXIM, so has the potential to provide an observational test of strong field gravity.

5.1 Introduction

Calculations of the relativistic corrections to photon properties have been ongoing for nearly three decades, starting with the classic work of Cunningham (1975) who calculated the distortions expected on the spectrum of a geometrically thin, optically thick, Keplerian accretion disc orbiting a Kerr black hole. Interest in these calculations dramatically increased with the realisation that the accretion disc could emit *line* as well as continuum radiation. Iron Kα fluorescence resulting from X-ray irradiation of the accretion disc can give a narrow feature, on which the relativistic distortions are much more easily measured than on the broad accretion disc continuum (Fabian et al., 1989). Since then, several groups have developed numerical codes that are capable of determining these effects both for standard discs (Dovčiak et al., 2004, and references therein) and alternative emission geometries, such as optically thin discs (Bursa et al., 2004).

While the problem is well-defined, there are many technical and numerical issues which arise in calculating the effects of strong gravity. Light bending can result in lensing which strongly amplifies the emission, so a very small area of the accretion flow can make a large contribution on the observed flux. In Chapter 3, we saw how to efficiently calculate the effects of strong light bending, which was applied in Chapter 4 to investigate the properties of Iron Kα line shapes in strong gravitational fields. Here we illustrate the effectiveness of this approach by using the code to compute the most extreme light bending possible, the higher order images and spectra of an accretion disc (Viergutz, 1993; Bao et al., 1994; Fanton et al., 1997).

The first order image is from photons from the underside of the disc which are bent back into the observers line of sight, while second order images are produced by photons from the upper side of the disc which complete a full orbit around the black hole before reaching the observer. Obviously such paths must cross the equatorial plane, so are likely to re-intercept the disc. For an optically thick disc then this returning radiation adds to the intrinsic disc emission, and can enhance the emissivity at small radii for extreme Kerr

black holes though it has little effect for Schwarzschild (Cunningham, 1976; Laor et al., 1990; Agol & Krolik, 2000; Li et al., 2005).

Nonetheless, the first order image of the disc can dominate the flux at high inclinations if the optically thick disc has rather limited radial extent. Even if it does not, some of the higher order image flux can escape to the observer through the inner 'hole' in the disc below the radius of the minimum stable orbit, assuming that the plunging region is optically thin (but see Reynolds & Begelman, 1997). The fraction escaping through this inner 'hole' is rather larger for Schwarzschild than for Kerr, as the size of the gap between the innermost stable orbit and horizon is larger for the non-spinning black hole. Obviously, such paths are exquisitely sensitive to the gravitational potential, being close to the true photon orbit point which is the (unstable) crossover between capture by the black hole, and escape to infinity. This makes them potentially an excellent test of strong gravity, and they could be observable in nearby luminous AGN with micro-arcsecond imaging X-ray interferometers such as MAXIM (Gendreau et al., 2001).

Such instruments could also observe the *spin* of a nearby supermassive black hole simply from the size of the *direct* image (Fukue, 2003; Takahashi, 2004), assuming that the mass and distance are known. A disc down to the last stable orbit extends down to 6 r_g in Schwarzschild but only 1.23 r_g in maximal Kerr ($a = 0.998$). Light bending is stronger in Kerr than in Schwarzschild, but the apparent size of the 'hole' in the disc still changes by a factor of ~ 3. This contrasts with the case where the accretion flow has emission down below the last stable orbit, where the size of the true black hole shadow is rather similar for both Schwarzschild and Kerr (Falcke et al., 2000; Takahashi, 2004). Observations of the galactic black hole binaries support to the idea that there is a disc down to the minimum stable orbit in certain, fairly high luminosity spectral states (Ebisawa et al., 1993; Koratkar & Blaes, 1999; Gierliński & Done, 2004). However, at lower luminosities this is probably replaced by a more complex accretion flow which may have continuous energy release down to the horizon (Narayan & Yi, 1995; Agol & Krolik,

2000; Krolik & Hawley, 2002; Afshordi & Paczyński, 2003). While the stellar remnant black holes require nano-arcsecond imaging to resolve, nearby luminous AGN also should have a 'hole' in the disc from the minimum stable orbit which is accessible to MAXIM.

5.2 Images of Thin Keplerian Accretion Discs

The contribution of higher order images to the observed flux is dependent both on the location of the observer and the angular momentum of the hole itself, together with the assumed geometry and emissivity of the accretion flow. For an optically thick accretion disc then any photons which re-intersect the disc after emission will be either absorbed (and then re-emitted) or reflected by the material. Figure 5.1 shows the contributions of both the direct ($N = 0$)and higher order ($N = 1, 2$) images of a geometrically thin disc extending from r_{ms} to $20r_g$, viewed at $\theta_o = 15°$ for both Schwarzschild and extreme Kerr black holes. The principal effect of black hole spin for the accretion disk dynamics is to move the location of the marginally-stable orbit, r_{ms} and hence the location of the inner edge of the accretion disc. In the case of the Schwarzschild hole the apparent location (as measured by a distant observer, see Figure 5.1 top row) of the direct image of the accretion disc is *further* from the origin than the higher order images, resulting in a distinct 'gap' where no photons are received by the observer. By contrast for an extreme Kerr black hole, the apparent location of the inner edge of the direct image coincides with that of the higher order images and so this gap is no longer present. Hence for high spin black holes a large fraction of the higher order image flux returns to the inner regions of the accretion disc. Note that the range of accessible redshifts is far narrower for the Schwarzschild disk than for the extreme Kerr case, due to the inner edge of the accretion disk (the marginally stable orbit) being located far deeper in the gravitational potential in the latter.

Figure 5.2 shows the same systems viewed at a range of large inclination angles, $\theta_o = 75° - 87.5°$. As in the previous discussion for the Schwarzschild hole, the inner edge of the accretion disc is located above the location of the photon orbits and hence the

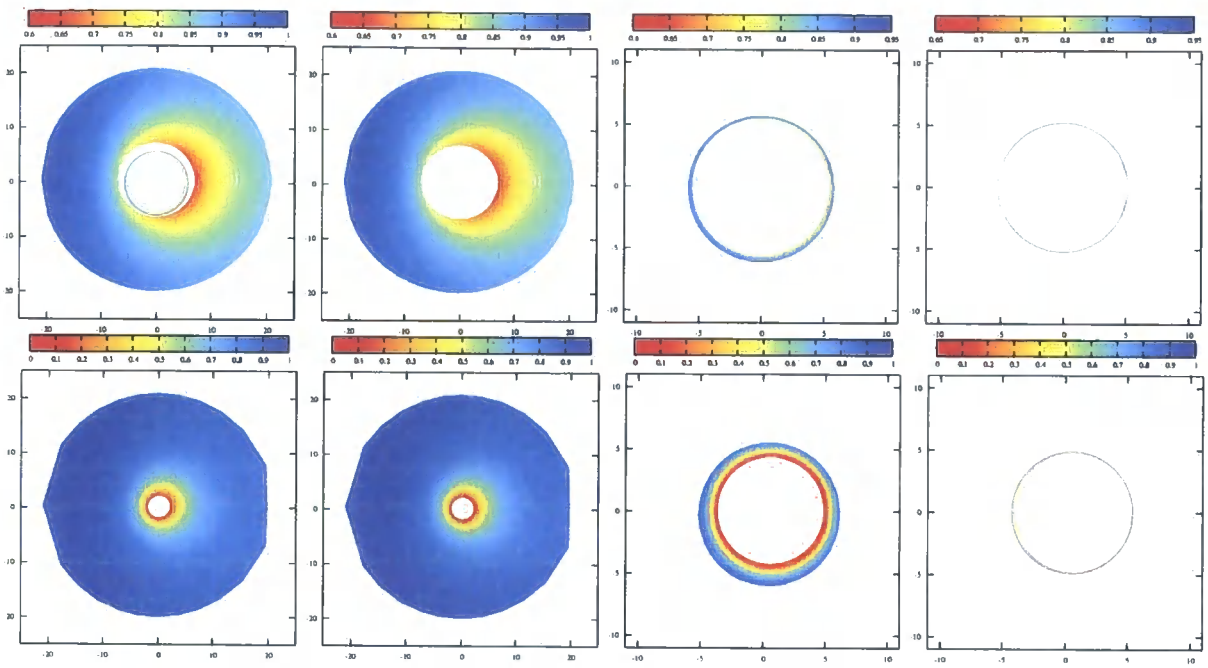

Figure 5.1: The contribution of orbiting photons (higher order images) to a distant observers image of a geometrically thin, optically thick, Keplerian accretion disc around Schwarzschild (top row) and extreme Kerr (bottom row) black holes. In both cases the observer is located at radial infinity with $\theta_o = 15°$, the disc extends from the marginally stable orbit ($6r_g$ for Schwarzschild, $1r_g$ for extreme Kerr) to $20r_g$ and the images are coloured by the associated value of the redshift parameter, $g = E_o/E_e$. From left to right, the panels show the contributions from (a) all image orders ($N = 0 \cdots 2$), (b) the direct ($N = 0$) image, (c) the first order ($N = 1$) image and (d) the second order ($N = 2$) image. Note that in the Schwarzschild case whilst the orbiting photons are not obscured from the observer by the accretion disc, the total flux (integrated area) measured by the observer from the photons is negligible. Additionally, for the Kerr case, the increased radial extent of the disc completely obscures the contribution of the photons.

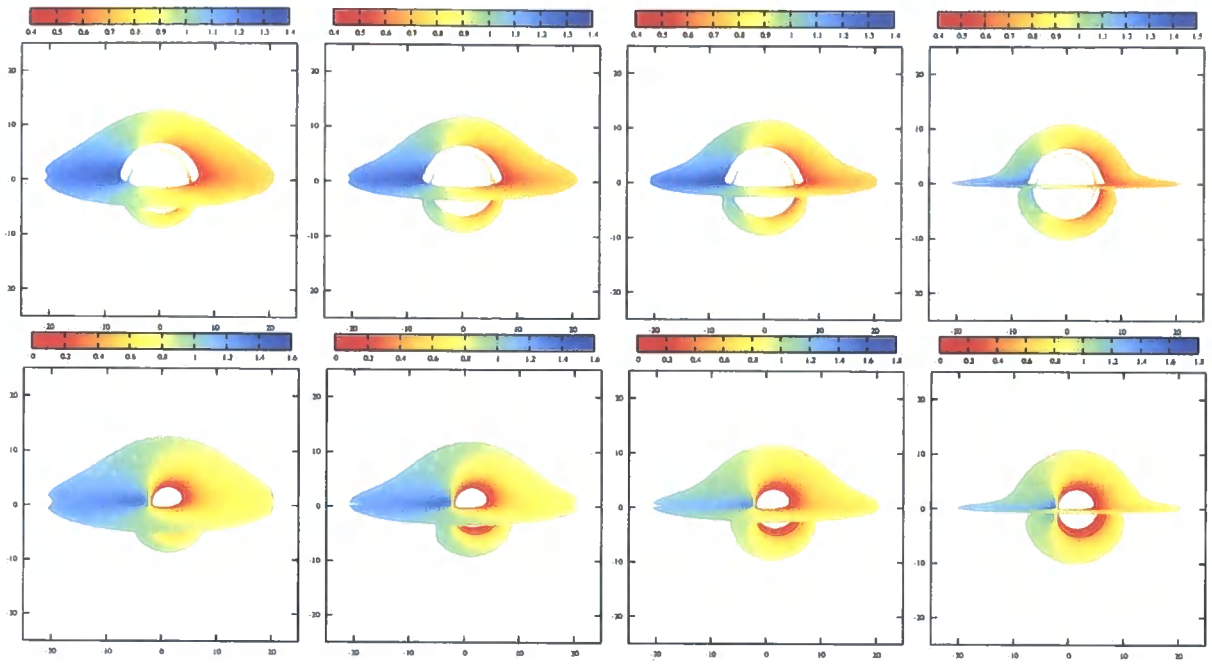

Figure 5.2: As in Figure 5.1 showing the contribution of photons with $N = 0 \cdots 2$. From left to right, the panels are for $\theta_o = 75.0, 77.5, 80.0, 87.5°$. As the inclination of the system increases, the contribution from photons emitted from the near side of the accretion disc directly to the observer is suppressed, reducing the obscuration of the higher order images by the disc as measured by the observer. The total area subtended by the unobscured first order ($N = 1$) image increases independently of this effect, due to lensing of photons that are emitted from the underside of the far side of the accretion disc, relative to the observer. In the case of the Schwarzschild hole (top row), we note that the (total) area of the second order image remains approximately constant with inclination. For the extreme Kerr hole (bottom row), photons forming the second order image are completely absorbed by the disc, removing their contribution from the overall image received by the observer. Additionally, in contrast to the Schwarzschild case, the images are asymmetric about the $\alpha = 0$ axis due to the effect of black hole spin, particularly noticeable for the higher order cases. For the most extreme inclination, the total area subtended by the first order image is on the same order as that from the direct image.

majority of the orbiting photons are able to propagate freely to the observer. However, photons in the first order image of the far side of the disc now have paths which pass rather closer to the hole than at lower inclination, so the importance of lensing is increased, strongly amplifying this part of the image. Most of these photons cross the equatorial plane at $r \geq 20r_g$, so can be seen in our simulation, but would be obscured by a more physically realistic disc which is not entirely flat and has outer edge $r \gg 20r_g$. These photons instead would illuminate a large region of the underside of the disc as the direct image of the disc, adding to its intrinsic emission. By contrast, the area on the sky of the second order image remains approximately constant with increasing inclination, reflecting the sensitivity (i.e. instability) of the two-loop photon orbits.

The high inclination extreme Kerr images are shown in Figure 5.2, bottom row. The disc itself blocks all the higher orbit images close to the black hole, similar to the $\theta_o = 15°$ case. Part of the first order image where the geodesic crosses the equatorial plane at $r \geq 20r_g$ can be seen, and this fraction increases with increasing inclination of the observer. Indeed, for the highest inclination system considered in this work, the apparent angular size of the first order image is approximately equivalent to that subtended by the direct image. By contrast to the Schwarzschild case, we note that the images of the extreme Kerr system are strongly asymmetric about the horizontal axis due to the effect of the black hole spin, with the degree of this asymmetry increasing with the inclination of the observer. This asymmetry is most pronounced for the (unobscured) first and second order images generated from the highest inclination system (see Figure 5.3). Here, the effect of the range of radii for orbiting photons can be seen most clearly in the second order image. The image is offset from zero as the ones on the left are the photons which are emitted from the side of the disc approaching the observer, so go with the spin of the black hole and orbit at r_g, while photons on the right are the retrograde ones at $4r_g$. The hole in the inner disc is symmetric at r_g, so it (just) obscures all the pro-grade photons and easily obscures the retrograde ones. A small decrease in spin (e.g. to a=0.998, the

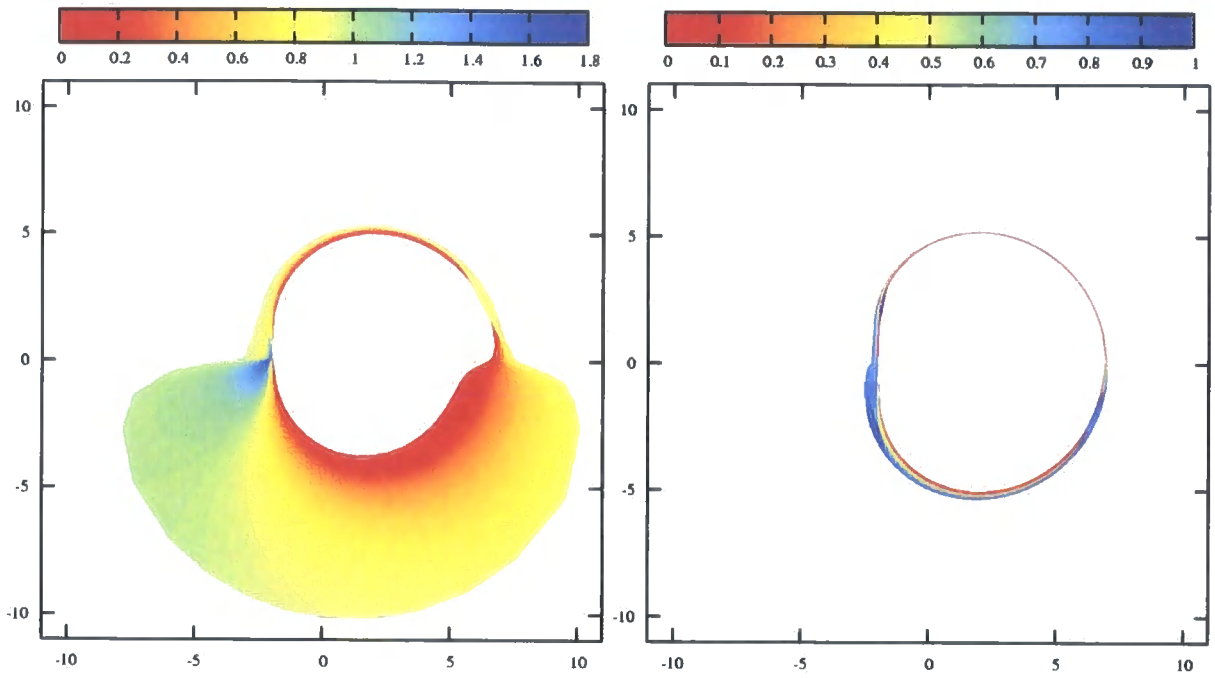

Figure 5.3: Unobscured $N = 1$ (left-hand panel) and $N = 2$ (right-hand panel) images of a thin, Keplerian accretion disc around an extreme Kerr black hole, with the disc extending from r_{ms} to $20r_g$. The observer is located at radial infinity with an inclination of $\theta_o = 87.5°$. The images are highly asymmetric, indicating the strong coupling of these photons to the black hole spin

equilibrium spin for thin disc accretion) increases r_{ms} to 1.23, while the photon orbits span $1.07 - 3.998r_g$, so a small part of the prograde higher order image can be seen. The fraction of higher order photons which can escape through the 'hole' decreases with increasing spin until $a \lesssim 0.65$, where the apparent location of the photon orbits is above that of the inner edge of the accretion disc (Bardeen et al., 1972).

5.3 Spectral Properties of Higher Order Images

To understand how the astrophysical properties of the accretion flow couple to the gravitational field of the black hole, we generate relativistically smeared line profiles as described in Beckwith & Done (2004) (see Section 3.4). For clarity, we briefly recap this method here. We consider an intrinsically narrow emission line with rest energy, E_e, for which the flux distribution measured by a distant observer at an energy E_o is given by:

$$F_o\left(E_o\right) = \frac{1}{D_o^2}\int\int g^4 \varepsilon\left(r_e, \mu_e\right)\delta\left(E_o - gE_{int}\right) d\alpha d\beta \tag{5.1}$$

Here, $\varepsilon\left(r_e, \mu_e\right)$ is the local emissivity of the accretion disc, which we take to have the form $\varepsilon\left(r_e, \mu_e\right) = \epsilon\left(r_e\right) f\left(\mu_e\right)$, where μ_e describes the initial direction of the photon relative to the local z-axis of the emitting material. The flux at each redshift in each image order is then calculated directly from the area subtended on the observers sky, together with the intrinsic disc emissivity (both radial and angular). This gives the transfer function for monochromatic flux, so the observed emission is the convolution of this with the intrinsic disc spectrum. In the case of intrinsically monochromatic radiation, e.g. the iron Kα fluorescence line which can be produced by X-ray illumination of cool, optically thick gas, then this transfer function directly gives the expected line profile. Photons produced by this emission process in regions close to the black hole enable us to examine the properties of the multiple orbit photons considered in the preceding section from a spectroscopic perspective.

To generate the line profiles, we apply a radial emissivity of the form $\epsilon(r_e) \propto r_e^{-3}$ (consistent with gravitational energy release within the disc (Życki et al., 1999) and consider three possible angular emissivity laws: (i) $f(\mu_e) \propto$ cons., corresponding to an optically thick disc (red lines); (ii) $f(\mu_e) \propto \mu_e^{-1}$, corresponding to an optically thin, limb brightened disc (blue lines) (Matt et al., 1993b) and (iii) $f(\mu_e) \propto (1 + 2.06\mu_e)$ corresponding to an optically thick, limb darkened disc (green lines) (Laor et al., 1990). Figure 5.4 shows the line profiles generated for the low inclination Schwarzschild disc discussed in the preced-

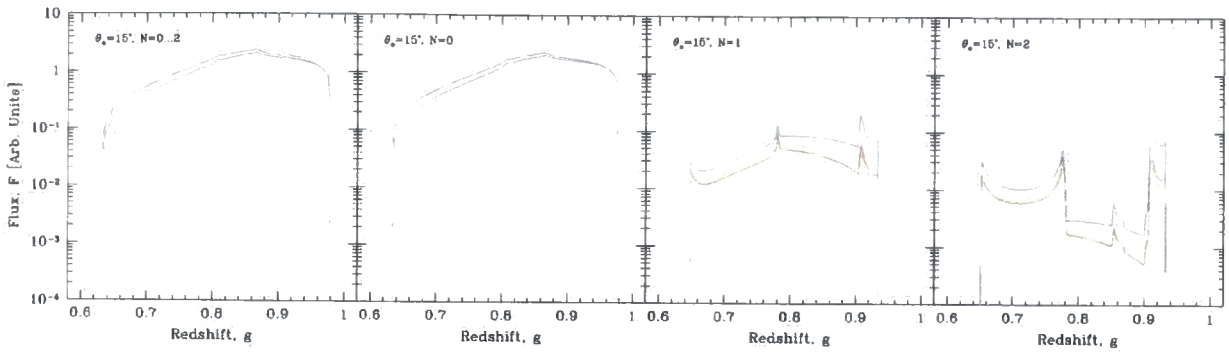

Figure 5.4: Relativistic line profiles generated from images (Figure 5.1, top row) of a geometrically thin, Keplerian accretion disc around a Schwarzschild ($a = 0$) black hole. The observer is located at $\theta_o = 15°$ and the disc extends from r_{ms} to $20r_g$. All profiles are normalised such that they contain one photon and are unsmoothed. From left to right, the panels show the contributions from (a) photons with $N = 0 \cdots 2$, (b) $N = 0$, (c) $N = 1$, (d) $N = 2$. In all cases a $\epsilon(r_e) \propto r_e^{-3}$ radial emissivity has been applied to the line profile. We consider three different types of angular component (i) $f(\mu_e) \propto$ cons. (red lines), (ii) $f(\mu_e) \propto \mu_e^{-1}$ (green lines) and (iii) $f(\mu_e) \propto (1 + 2.06\mu_e)$ (blue lines). The principal effect of the higher order images is to boost the overall flux in the system by $\sim 4\%$, whilst leaving the overall shape of the line approximately unchanged.

ing section. Whilst in the case of the extreme Kerr black hole (Figure 5.1, bottom row), all orbiting photons returned to the inner region of the disc, for the Schwarzschild hole (Figure 5.1, top row) these photons cross the equatorial plane below r_{ms} and can freely propagate to the observer (although see Reynolds & Begelman, 1997). Examination of their spectral properties shows that these photons play a limited role in forming the overall spectral shape measured by a distant observer, which is completely dominated by the contribution from the direct image.

Figure 5.5 shows the line profiles generated for a Schwarzschild hole, with the accretion disc now viewed at high inclination (ignoring the effect of obscuration). For the direct

image, limb darkening boosts the effects of gravitational lensing, enhancing the flux from the far side of the hole. This is because these photons are strongly bent, i.e. are emitted from a lower inclination angle than that at which they are observed, so a limb darkening law means that the flux here is higher (Beckwith & Done, 2004). The Doppler shifts are rather small for this material, so this lensing enhances the flux in the middle of the line. Since the line profiles are normalised to unity, this means that the blue wing is less dominant.

The first order spectra are shown in Figure 5.5, middle row. The transfer functions mostly retain the characteristic double peaked and skewed shape, and again the principal effect of the different angular emissivities is to alter the balance between the blue wing and leased middle of the line. However, there is some new behaviour for the limb brightened emissivity. This has the largest change in emissivity with angle, and this combined with the exquisite sensitivity of lensed paths means that this picks out only a small area on the disc, leading to a discrete feature in the spectrum. These profiles also show enhancement of the extreme red wing of the line, as the photons which orbit generally are emitted from the very innermost radii of the disc.

The discrete features are completely dominant for all emissivities at second order (Figure 5.5, bottom row). These are images of the top of the disc where the photons have orbited the black hole, so the paths are even more sensitive to small changes than first order. Thus the profiles are significantly more complex in structure, being dominated by lensing. There are blue and red features at the extreme ends of the line profile which are picking out the maximum projected velocity of the innermost radii of the disc. These have the standard blue peak enhancement. However, the two strong features redward of this are a pair of lensed features, from the near and far side of the disc.

Figure 5.6 shows the line profiles generated for the extreme Kerr hole at high inclinations, again ignoring the effect of obscuration. For the direct image (Figure 5.6, top row), the lines exhibit the characteristic triangular shape previously reported by (e.g)

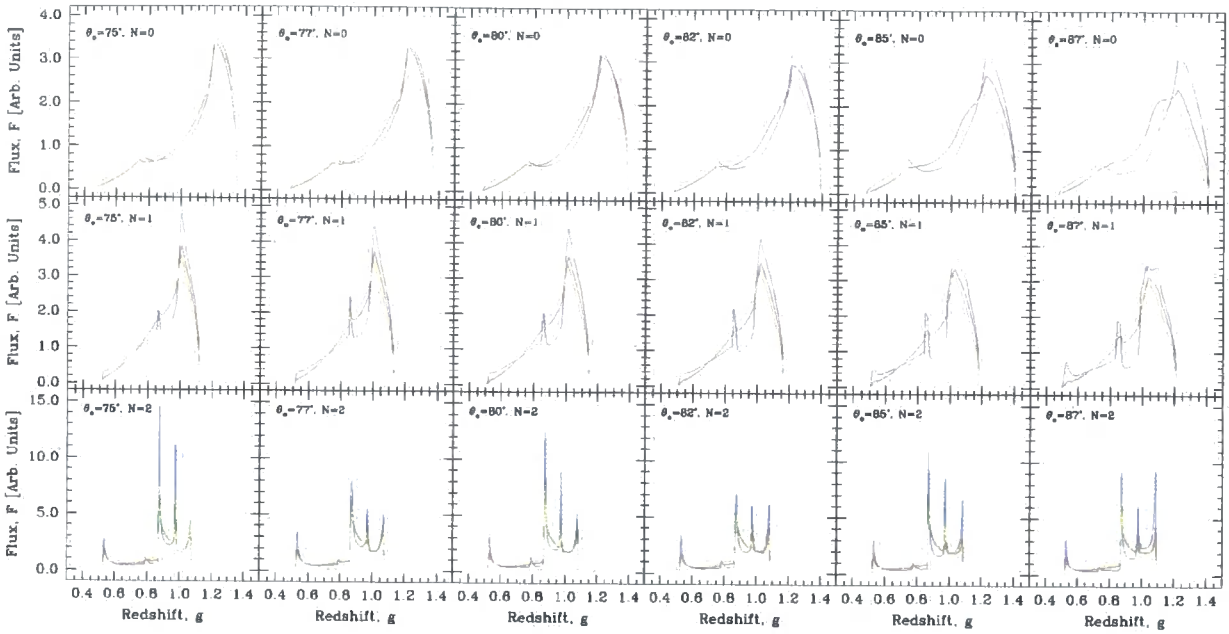

Figure 5.5: The contribution of orbiting photons (higher order images) to the Iron Kα line profiles for a geometrically thin, Keplerian accretion disc around a Schwarzschild black hole. In all cases, the inner edge of the accretion disc is located at the innermost stable orbit, which occurs at $6r_g$ and the outer edge of the disc is located at $20r_g$. The observer is located at radial infinity with inclination (from left to right) $\theta_o = 75° \cdots 87.5°$ in 2.5° steps. All profiles are normalised to the apparent area on the observers sky and are unsmoothed. The line profiles are generated by photons in (a) the zeroth order (direct) image (top row), (b) the first order image (middle row) and (c) the second order image (bottom row). Obscuration by the disc is ignored. In all cases a $\epsilon(r_e) \propto r_e^{-3}$ radial emissivity has been applied to the line profile. We consider three different types of angular component (i) $f(\mu_e) \propto$ cons. (red lines), (ii) $f(\mu_e) \propto \mu_e^{-1}$ (green lines) and (iii) $f(\mu_e) \propto (1 + 2.06\mu_e)$ (blue lines). Line profiles generated by the zeroth order photons have the standard skewed, double peaked structure. Those generated by the first order photons have a similar structure, whilst those from the second order photons are far more complex. As the observer moves towards higher inclinations, gravitational lensing effects become apparent in the line profile generated from zeroth order photons. There is a corresponding increase in the complexity of the profile generated from the first order photons. Note however, that the structure of the profile generated from the second order photons remains approximately constant with increasing inclination.

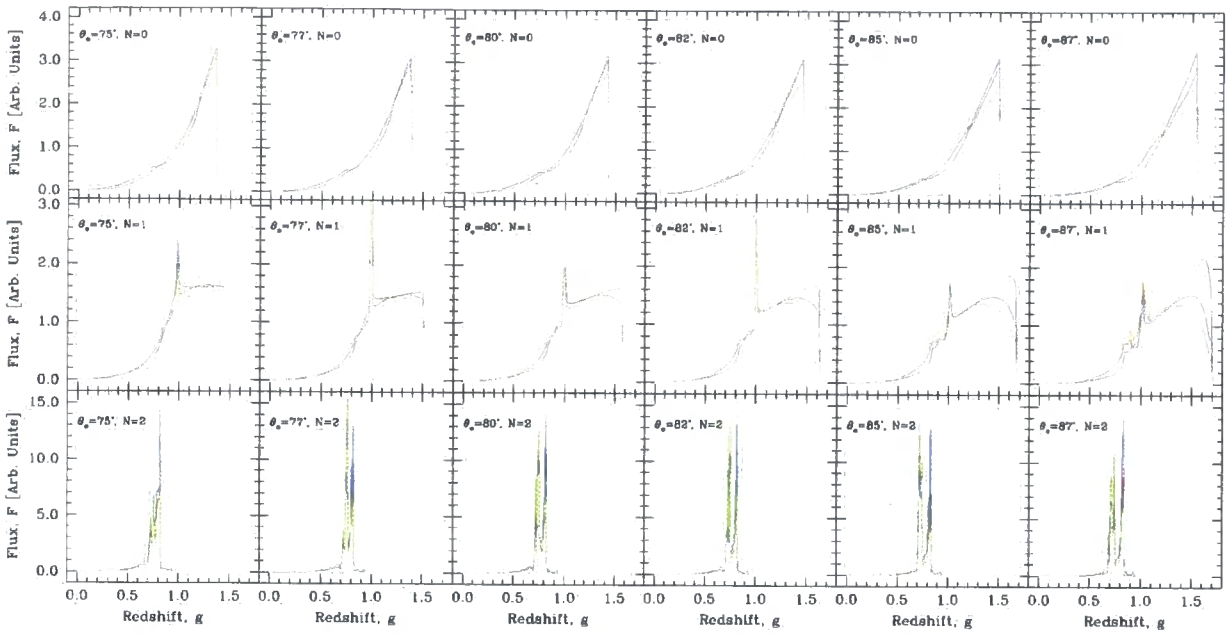

Figure 5.6: As in Figure 5.5 for accretion discs around an extreme Kerr black hole. By contrast to the Schwarzschild case, the lines extend down to lower energies due to the reduced separation between the inner edge of the disc (at the marginally stable orbit) and the black hole event horizon. Additionally, the line due to the first order photons extends to higher energies than that due to the zeroth order photons, with the upper edge of the line occurring at $g \approx 1.8$ in the most extreme case. Both the first and second order line profiles have significantly increased structure compared to the zeroth order profile. The shape of the zeroth and second order line profiles remain approximately constant with increasing inclination. However, the internal structure of the first order profile shows a distinctive change, with the fraction of radiation in the blue wing of the profile exhibiting a marked increase compared to that in the red wing as the observer moves towards the equatorial plane.

Laor (1991), with the variation in angular emissivity acting to alter the balance between the different regions of the line on a $\sim 5\%$ level. The lines associated with the first order image (Figure 5.6, middle row) exhibit a marked difference in comparison to those associated with the Schwarzschild black hole. In general, they are broader that those associated with the direct image and resemble a skewed Gaussian combined with a narrow line (due to caustic formation) at $g \approx 1.0$. Here the principal effect of changes in the angular emissivity is to alter the height of the blue wing, relative to the rest of the line. Again, the line profiles associated with the second order image (Figure 5.6, bottom row) are completely dominated by discrete features, as in the Schwarzschild case.

5.4 Image Luminosities

To understand the relative roles played by each (unobscured) image order, we consider the variation of the luminosity of each image as a fraction of the total luminosity of the system as a function of inclination, again for both Schwarzschild and extreme Kerr black holes (Figure 5.7). These luminosities are generated from the integral in redshift space of the line profiles considered in the preceding section and hence we consider systems with identical properties to those previously discussed. In the case of the Schwarzschild hole, we see that, for inclinations $< 80°$, the first order image can be regarded as a $\leq 10\%$ correction to the emergent flux from the system. For inclinations $\geq 80°$, this image contains $10 - 20\%$ of the emergent flux, i.e. even at these high inclinations, the first order image can still be regarded as a correction to the direct image. For the second order image, we see that it plays a $\leq 1\%$ role independent of inclination. Third and higher order images will have correspondingly smaller fluxes, so can safely be neglected.

There is a larger fraction of flux in the higher order images for the Kerr black hole. At low inclinations, the first and second order images contain 10% and 1% of the total flux, respectively. The variation of the luminosity fraction for the three image orders displays an approximately power law like behaviour for inclinations $\leq 60°$, where a distinct break

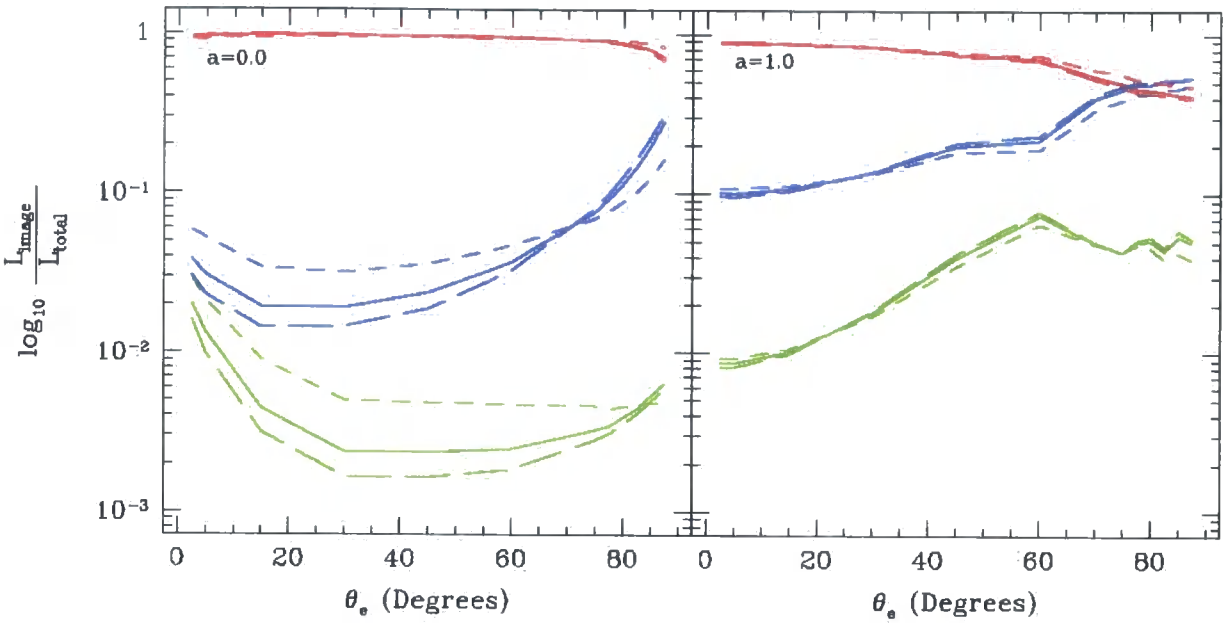

Figure 5.7: Variation of (unobscured, integrated) luminosity associated with each image as a fraction of the total luminosity of the system with inclination for a thin, Keplerian accretion disc around a Schwarzschild black hole (left panel) and extreme Kerr (right panel). In both cases, the disc extends from r_{ms} to $20r_g$ and the observer is located at radial infinity. We show the contributions from (a) the direct image (red lines), (b) the first order image (blue lines) and (c) the second order image (green lines). In all cases, we have applied a $\epsilon(r_e) \propto r_e^{-3}$ radial emissivity and have considered angular emissivities of the form (i) $f(\mu_e) \propto$ cons. (solid lines), (ii) $f(\mu_e) \propto \mu_e^{-1}$ (short dashed lines) and (iii) $f(\mu_e) \propto (1 + 2.06\mu_e)$ (long dashed lines). In the case of the Schwarzschild hole, the contribution from the higher order images is $\leq 20\%$ of the total luminosity, even at high inclinations. However, in the case of the extreme Kerr black hole, at inclinations of $\geq 75°$, the first order image can dominate the luminosity of the system, due to the formation of caustics within the image.

occurs, due to the appearance of a caustic in the first order image, whose luminosity is therefore significantly enhanced. It is at this point that the peak luminosity of the second order image occurs, which here is on the level of 10%, approximately an order of magnitude higher than in the Schwarzschild case. Remarkably, for inclinations $> 75°$, the luminosity of the first order image produced by the optically thick discs is *greater* than that produced by the direct image.

However, most of the higher image order flux is expected to re-intercept the disc plane, and hence be absorbed and re-radiated. This is especially the case for realistic discs around an extreme Kerr black hole, where the whole of the equatorial plane is covered by the disc from r_g to large radii. However, for Schwarzschild, the existence of a central 'hole' means that the flux from higher order images can escape. A realistic disc around a Schwarzschild black hole when viewed *face on* has 10% of its flux in a higher order image ring (dropping to $\sim 7\%$ for a more extended disk ranging from $r_{ms} \rightarrow 400r_g$). Essentially, a spatial resolution equivalent to $2r_g$ is required to resolve these features, which for typical nearby Active Galactic Nuclei corresponds to an angular resolution of 0.01 micro-arcseconds. This is obviously extremely technically difficult, but is feasible for an X-ray interferometer imaging supermassive black holes in nearby galaxies (Gendreau et al., 2001).

5.5 Conclusions

Photons orbiting a black hole are exquisitely sensitive to the properties of the gravitational field. Thus these higher order null geodesics provide the best test of Einstein's gravity in the strong field limit. We have developed a new strong gravity code capable of describing these paths, and calculate them for a geometrically thin, optically thick (standard) disc in both Schwarzschild and Kerr metrics. These higher order image paths must cross the equatorial plane, so are absorbed where this is filled by the optically thick disc. As has long been known, the major amplification effects of gravitational lensing are for the first

order paths from the far side of the underneath of the disc viewed at high inclination i.e. photons initially emitted downwards on the far side of the black hole, which are bent by gravity up above the disc plane. Most of these paths will re-intersect the disc unless it has very limited outer radial extent. While such discs *may* exist (Reynolds et al., 2004), it seems far more likely that these photons would be absorbed by material in the equatorial plane. However, there is some fraction of the higher order images where the light paths are so strongly bent that they re-intersect the equatorial plane very close to the photon orbit radius. By definition, this is below the minimum stable orbit for particles, so the standard disc cannot exist at this point. Instead, for a stress-free inner boundary condition, the disc material plunges rapidly though this region, so there is much less absorbing material in the equatorial plane. This material may be optically thick at high mass accretion rates (Reynolds & Begelman, 1997), but this depends on whether the flow in the plunging region is smooth or clumpy. Hence higher order photons which cross the plane below $6r_g$ need not be reabsorbed by the disc. We show that these *observable* higher order photons can carry 10% of the flux for a *face on* disc. Edge on discs *reduce* the expected observable flux as only about half of the orbiting photon ring can be seen through the gap below r_{ms}, while the rest re-intercepts the disc at $r \gg r_{ms}$.

The situation is less favourable in the Kerr geometry as photons now orbit at a range of radii depending on how their angular momentum is aligned with the spin of the black hole. Photons going against the spin will orbit at radii which are larger than that of the minimum stable orbit of the disc, so should be absorbed rather than escaping through the inner 'hole' in the disc (provided $a \gtrsim 0.65$). Thus for Kerr black holes, even though there is a greater fraction of photons in the higher order images, we expect that these are less observable due to the overlap between the photon and particle orbits. Also, even though there is still a gap between the last stable particle orbit and the aligned photon orbits, this gap is much smaller than in Schwarzschild, both in terms of radial coordinate and in terms of impact parameter on the sky. For a=0.998, the equilibrium spin for thin

disc accretion, $r_{ms} = 1.23r_g$ while the $r_{ph}^{(-)} = 1.07$, so $\Delta r = 0.16$. Since the photons orbit in slightly stronger gravity, their paths are more distorted, so the difference in their impact parameter at infinity is slightly less than the difference in radial coordinate. Thus the higher order images round a rapidly spinning black hole are much more difficult to spatially resolve from the direct image of the disc, and carry less flux than Schwarzschild as only a fraction re-intersect the plane below r_{ms}.

Thus the best chance of observing these higher order photon paths from a standard accretion disc is with a face-on Schwarzschild black hole. X-ray interferometry could potentially directly resolve such scales for supermassive black holes in nearby galaxies, and such missions are being seriously proposed (MAXIM: Gendreau et al., 2001). Even if the plunging region is optically thick, direct imaging with resolution $\leq 2r_g$ will clearly show the black hole spin from the apparent size of the 'hole' in the centre of the disc. The radial coordinate of the innermost stable orbit in an equilibrium spin Kerr metric is a factor of ~ 3 smaller than for Schwarzschild, which translates to a change in apparent size at infinity of the 'hole' diameter from $\sim 5r_g$ (a=0.998) to $\sim 14r_g$ (a=0). This is important as recent papers have emphasised that the true size of the shadow of the event horizon (in effect the impact parameter of the orbiting photons, given fairly accurately by our second order image) is rather similar in both Schwarzschild and Kerr (Falcke et al., 2000; Fukue, 2003; Takahashi, 2004). This is true, but different to the size of the 'hole' defined by the innermost stable orbit of the disc. For continuous energy release down to the event horizon, the 'hole' in the image of the accretion flow is set by the true shadow size, but for accretion flows where the energy is only released from stable particle orbits (the disc, as opposed to the plunging region) then the innermost stable orbit sets the size scale. Whether the energy release can be continuous across r_{ms} is currently a matter of active research (Krolik & Hawley, 2002). However, there is clear observational evidence for an innermost stable orbit in the disc dominated spectra of galactic black hole binaries (Ebisawa et al., 1993; Kubota et al., 1999; Gierliński & Done, 2004), so it seems likely

that the accretion flow can take the standard thin disc form assumed here.

The spectral signatures of these higher order photons only become apparent for high-inclination systems, where they carry between $\sim$ 20% (Schwarzschild) and $\sim$ 60% (extreme Kerr) of the total luminosity of the system. However, in a realistic system, the disc extends out to many thousands of gravitational radii from the black hole and so these photons return to the disc before reaching the observer. Far from the central black hole, the effect of the returning radiation is comparable to the gravitational potential energy of the material and so these photons can play an important role in shaping the properties of the disc here. In particular, reprocessing of this returning radiation at large distances from the hole will potentially provide a physical mechanism to flatten (at large radii) the $r^{-3/4}$ temperature profile of a planar accretion disc irradiated by a central source, which could help to resolve the conflict between the predicted and observed optical/UV colours in Active Galactic Nuclei (Koratkar & Blaes, 1999).

The code used to calculate these results is an extension of that of Beckwith & Done (2004). The new aspect described here is a set of analytic constraints on the possible photon trajectories which vastly reduce the scale of the calculation. This, combined with the use of the analytic integrals (elliptic functions) for the photon paths, has the result that the calculation of a photon trajectory linking two points (the emitter and observer, (Viergutz, 1993) can be performed by a simple minimisation, capable of being calculated to almost arbitrary accuracy on a standard desktop PC on time scales of a few minutes. This technique allows us to include the contribution of orbiting photons in the calculations without loss of resolution. The code is also flexible enough to be adapted to *any* accretion flow, and a future work will consider the contribution of the higher order images in an optically thin, geometrically thick flow.

Chapter 6

Observational Diagnostics of Modern Accretion Flows

Abstract

Modern descriptions of black hole accretion disks rely on the Magneto-Rotational Instability to provide angular momentum transport within the disk. In recent years, it has become clear that the properties of accretion disks in this description are rather different to those in the standard model. To date, the majority of these studies present results that are defined in the rest frame of the disk. Determination of the observational characteristics of the flow requires a description of dissipation within the disk, coupled to a GR ray-tracing code. We perform these calculations based on the GRMHD simulations presented previously by De Villiers et al. (2003). We explicitly compare dissipation derived from the magnetic 4-current density at late times in the simulations with that derived from the standard model, showing that these two quantities are well-matched.

Using this description of dissipation, we firstly calculate the observed spectral characteristics of optically thin, bound material within the disk. Observationally, such a flow could correspond to emission from the optically thin, geometrically thick, hot inner flow that may be found in the hard state of low mass X-ray binaries such as XTEJ1550-564 (Zdziarski & Gierliński, 2004). The shape of the high-energy cutoff at $\sim$ 100keV is found

to be strongly modulated by relativistic effects originating in the dynamics of the accretion flow combined with the effect of black hole spin, which should be directly testable.

In a separate approach, we examine the properties of fluorescent Iron Kα lines expected from these GRMHD accretion flows. We assume that the mid-plane of the disk is optically thick and illuminate this surface with hard X-ray photons. These photons originate in either bound material surrounding the mid-plane (the disk 'corona') or by rapidly outflowing, unbound material (the 'jet'). The resulting illumination patterns are well described by $\varepsilon(r_e) \propto r^{-q}$. For illumination due to unbound material, $q \sim -2$, independent of black hole spin. By contrast, $q \sim -3, -4$ for illumination due to bound material for slowly and rapidly rotating holes respectively. For a specified black hole spin, the resultant Iron Kα line profiles are found to extend to lower energies than would be expected from standard accretion disk models, as previously reported by Reynolds & Begelman (1997). However, the change in illumination pattern due to bound material with increasing black hole spin results in a noticeable change in the line shape.

6.1 Introduction

The standard model of a relativistic accretion disk due to Novikov & Thorne (1973), Page & Thorne (1974) is essentially a parametrised, one-dimensional, time-averaged description of what potentially is an extremely complex physical process. In these models, the authors specify an anomalous viscosity to provide angular momentum transport within the disk. However, in this description, the physical mechanism providing angular momentum transport is unclear. Furthermore, stability studies of these accretion disk models (see e.g. Frank et al., 2002) have shown them to suffer from many instabilities, which raises fundamental questions about their applicability.

The key question for accretion flow dynamics is the mechanism that supplies the outwards transport of angular momentum through the disk and hence enables the inflow of material. It now seems likely that this mechanism is provided by the magneto-rotational

instability (MRI Balbus & Hawley, 1991). Essentially, two radially adjacent fluid elements within a Keplerian accretion flow are connected by magnetic field lines, which are stretched by the relative motion of the two elements. If we imagine the field as a spring connecting the two elements, then it is apparent that the field will act to decrease the velocity of the inner fluid element, whilst increasing that of the outer element. Mass is therefore able to flow inward through the disk, whilst angular momentum is transferred into the outer regions. This instability leads directly to the generation of MHD turbulence within the flow, which in turn provides enhanced angular momentum transport. The dynamical properties of the inner regions of the accretion flow are crucially important in determining global properties of the flow, such as accretion efficiency and the amounts of matter-energy & angular momentum captured by the hole. In the MRI paradigm, although the flow does know about the presence of the marginally stable orbit, magnetic stress can extend below this radius (see e.g. Krolik & Hawley, 2002; Krolik et al., 2005). This is rather different to the picture in the standard model of thin disks, where (by construction) the stress goes to zero and the (stable) disk is truncated here. Our calculations are based on late-time, azimuthally averaged data from the global, General Relativistic Magneto-Hydrodynamic (GGRMHD) Keplerian Disk (KD) simulations described in the literature by De Villiers et al. (2003); Hirose et al. (2004); De Villiers et al. (2005); Krolik et al. (2005).

From an observational standpoint, these differences are rather important. Recent observational studies of both Galactic Black Hole Candidates and Active Galactic Nuclei (see Chapter 2 along with, e.g. Reynolds & Nowak, 2003; Miller et al., 2004; Fabian & Miniutti, 2005) have indicated the existence of a highly broadened Iron Kα line in the $2 - 10keV$ spectral band, which, at face value, implies black hole spins approaching maximal ($a = 0.998$). In a previous paper (Beckwith & Done, 2004, see Chapter 4) we have addressed the shortcomings of the currently available models in modelling the relativistic effects on the line, along with the effects of the accretion disk atmosphere. The properties of the line may well also be sensitive to the underlying dynamics of the

accretion disk. Reynolds & Begelman (1997) have shown that emission from within the plunging region can significantly broaden the line, although this may well be sensitive to both the radial and angular dependence of the emissivity pattern and the dynamics of the disk in this region. In this work, we examine the properties of the lines generated by these GGRMHD accretion flows and compare these to the lines expected from the standard disk models.

Connecting modern descriptions of accretion flows to observational data is not limited to calculations of Iron Kα line profiles. The geometry for the hard state of Galactic X-ray binary systems may consist of a hot, optically thin, geometrically thick, inner flow, which at some (possibly large) distance from the black hole, joins onto a cool, optically thick, geometrically thin accretion disk (Zdziarski & Gierliński, 2004). As such, the emission from the hot inner flow should be convolved with gravitational effects which modify the shape of the intrinsic spectrum, in particular the high energy cut off at $\sim 100keV$. Observationally, this rollover is well-defined, at odds with the expected broadening due to relativistic effects. We calculate the broadening predicted by the GGRMHD flows, assuming that bound material within the flow is optically thin. By combination of a description of dissipation within flow with the intrinsic flow dynamics and fully relativistic treatment of photon propagation, we are able to calculate the expected broadening of the low/hard state spectra, which can be compared to observational data to further constrain our understanding of both accretion and strong gravity.

The rest of this chapter is divided into six sections. In Section 6.2, we overview the results of the KD simulations on which this work is based. In Section 6.3, we describe how we model the heating distribution in the accretion flow, which we then apply in Section 6.4 - 6.6 where we describe generation of the spectra. In Sections 6.7 & 6.8, we examine the spectral properties of emission from the optically thin, geometrically thick hot inner flow and the Iron Kα diagnostics, respectively. Finally in Section 6.9, we summarise our results and point the way to future work.

6.2 Overview of Simulations

The calculations presented here are based on the results of the Keplerian Disk (KD) simulations which have been presented in a series of papers by De Villiers et al. (2003); Hirose et al. (2004); De Villiers et al. (2005); Krolik et al. (2005). For purposes of clarity, we give a brief recap of the key points of these simulations which shall be necessary for future discussions. The equations of ideal non-radiative Magnetohydrodynamics (MHD) are solved in the metric of a rotating black hole by use of the algorithm described in detail by De Villiers & Hawley (2003a). We work in the Kerr metric (with determinant $\sqrt{-\mathbf{g}}$) written in Boyer-Lindquist coordinates, using gravitational units ($G = M = c = 1$).

The initial conditions for the KD simulations consist of an isolated gas torus orbiting near the black hole, with the pressure maximum located at $r \approx 25M$ and a (slightly) sub-Keplerian distribution of angular moment throughout, whilst the magnetic field is initialised to consist of loops of weak poloidal field lying along isodensity surfaces within the torus. This work will focus on the properties of the four high resolution models presented by De Villiers et al. (2003), which are designated KD0, KDI, KDP and KDE and correspond to black hole spins of $a = 0.0, 0.5, 0.9, 0.998$ respectively. Each model consists of $192 \times 192 \times 64$ (r, θ, ϕ) grid zones, where the inner radial boundary is located at $r_{in} = 2.05, 1.90, 1.45, 1.175M$ for models KD0, KDI, KDP, KDE respectively (i.e. just above the black hole event horizon in each case). The outer radial boundary is located at $r_{out} = 120M$ in all cases and the radial grid is set by a hyperbolic cosine function in order to maximise resolution close to the inner boundary. For the θ-grid we take $0.045\pi \leq \theta \leq 0.955\pi$, using an exponential grid spacing function that concentrates zones near the equator along with a reflecting boundary condition. Finally, the ϕ-grid spans the quarter plane, $0 \leq \phi \leq \pi/2$, with periodic boundary conditions in ϕ, which significantly reduces the computational requirements of the simulation (for further discussions on the effect of this restriction see De Villiers & Hawley, 2003a,b). Each simulation was run to time $8100M$, which corresponds to approximately 10 orbits at the pressure maximum,

with the temporal time step, Δt being determined by the extremal light crossing time for a zone on the spatial grid, remaining constant for the entire simulation (De Villiers et al., 2003). The simulations are initialised to have only a finite reservoir of material in the disc, that is, the radial boundary conditions are set such that only outflow of material from simulation volume is permitted. As outlined in De Villiers et al. (2003), the quasi-steady-state system is usefully divided into five main regions: (i) the main body of the disk; (ii) the coronal envelope; (iii) the inner torus and plunging region; (iv) the funnel wall jet; (v) the evacuated axial funnel. The amount of material accreted by the black hole during the course of the simulation decreases with increasing black hole spin, however, even for the $a = 0$ case (KD0), this corresponds to only 14% of the total mass within the disk. Note that we distinguish between unbound and bound material within the simulation volume by requiring that unbound material possess $-hu_t > 1$ and be have positive proper radial velocity, $u^r > 0$, where h is the relativistic enthalpy and u^μ is the 4-velocity of the gas (see De Villiers et al., 2005).

6.3 Dissipation & Relation to Current Density

For our purposes, the most important point of interest in the properties of the magnetic field is to identify regions of the simulation where X-ray release is likely to occur. However, the KD simulations were conducted with no explicit resistivity and as such do not address the questions of where the magnetic field is dissipated, or the rate at which this process occurs. A naive application of Ohm's law (Power $\propto$ Current^2) leads us towards considering the magnetic current density as a trace of dissipation within the flow. Rosner et al. (1978) have suggested that (in the case of the solar corona), regions of high current density are *candidates* for regions of high magnetic dissipation (and hence thermal heating), as high current density *may* trigger anomalous resistivity through mechanisms such as ion-acoustic turbulence, although it should be emphasised that no physical model relating current density and dissipation is currently known. In the absence of such a physical

model, we follow Hirose et al. (2004) and simply set the heating distribution proportional to the square of the 4-current density. With this assumption, let us define the dissipation per unit disk radius to be:

$$D(r_e) = \frac{2}{\pi} \int_{0.045\pi}^{0.955\pi} \int_0^{\pi/2} \sqrt{-\mathbf{g}} J^\mu J_\mu d\theta d\phi \tag{6.1}$$

In Figure 6.1 we show an explicit comparison of this quantity and the dissipation per unit disk area derived from the standard relativistic disk model (see Section 2.4 and Novikov & Thorne, 1973), where we have assumed the stress-free inner boundary condition. Clearly, the two descriptions of dissipation are well matched for $r \gtrsim 10M$, independent of black hole spin. For the slowly rotating holes (KD0,KDI), this remains true until the turnover in the Novikov-Thorne description close to r_{ms} (due to the application of the stress-free inner boundary condition in the latter case). However, in the case of the rapidly rotating black holes (KDP,KDE), dissipation in the simulations is in deficit by comparison to the prediction of the standard model in this region. However, the closeness of the match between the dissipation derived from the shell-integrated current density and that demanded by energy conservation within the standard disk lends support to our assumption that dissipation within the simulation is traced by the current-density.

We assume that a volume element within the simulation emits radiation with specific intensity proportional to the 4-current density. The observed spectra of this material is generated from this heating distribution, convolved with a transfer function (see Section 6.4). The total heat dissipated in each volume element is therefore proportional to the locally-integrated square of the 4-current density:

$$\jmath(r_e, \theta_e) = \frac{2}{\pi} \int_{r_e - dr/2}^{r_e + dr/2} \int_{\theta_e - d\theta/2}^{\theta_e + d\theta/2} \int_0^{\pi/2} \sqrt{-\mathbf{g}} J^\mu J_\mu dr d\theta d\phi \tag{6.2}$$

Figure 6.2 shows a map of this heating distribution for each of the KD simulations. From these maps, it is clear that the heating distribution for the simulations corresponding to slowly rotating black holes (KDO, KDI) are dominated by the contribution from bound material in the disk, whilst the simulations corresponding to rapidly rotating black holes

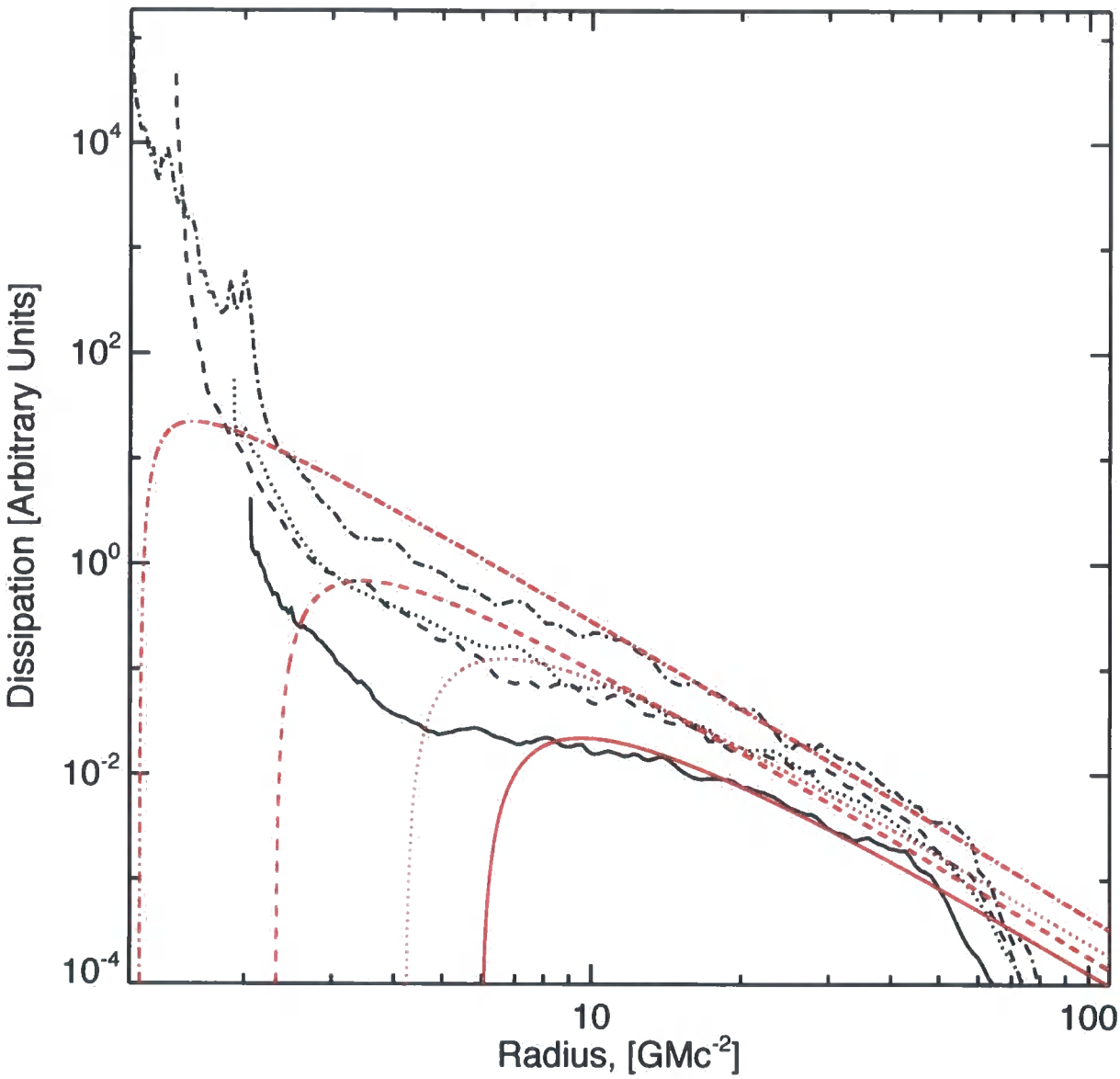

Figure 6.1: Comparison of dissipation in the KD simulations (black lines) with that in the standard model of accretion disk (red lines, Novikov & Thorne, 1973), where we have assumed the stress-free inner boundary condition. We denote KD0 ($a = 0$) with solid lines, KDI ($a = 0.5$) with dotted lines, KDP ($a = 0.9$) with dashed lines and KDE ($a = 0.998$) with dot-dash lines. The standard disk model gives a remarkably good description of dissipation in the simulations for $r \gtrsim 10M$, independent of black hole spin. For the slowly rotating holes this remains true until close to r_{ms}. For the rapidly rotating holes (KDP,KDE), dissipation in the simulations is in deficit compared to the standard for $r_{ms} \leq r \leq 10M$.

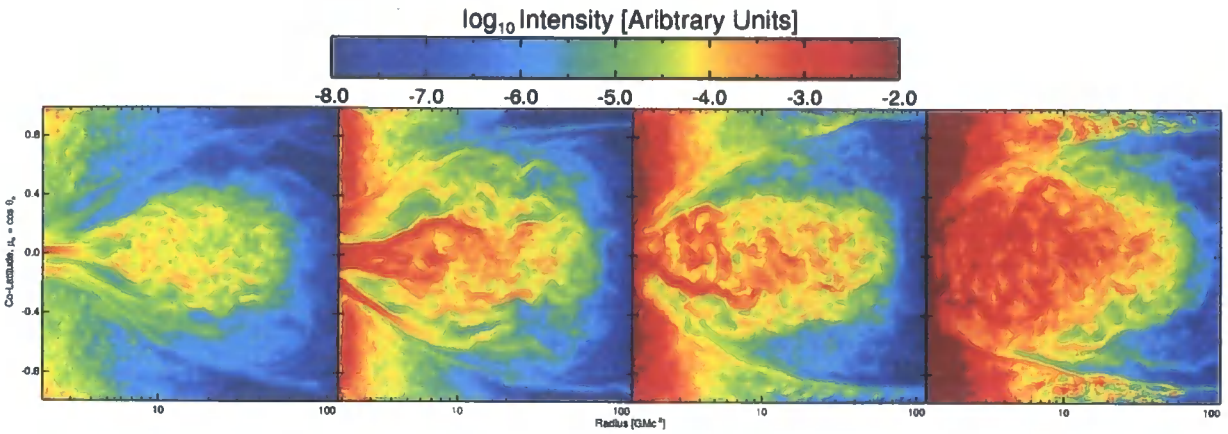

Figure 6.2: Maps of the heating distribution (emitted intensity), $\jmath(r_e, \theta_e)$. From left to right, the panels are maps for the KD0, KDI, KDP & KDE simulation data sets, which correspond to black hole spins of $a = 0.0, 0.5, 0.9, 0.998$ respectively. Clearly, emission from the flows surrounding the slower spinning black holes is dominated by the contribution from bound material in the disk, whereas emission from the higher spin black holes is dominated by the contribution from unbound material in the jet/outflow.

(KDP, KDE) are dominated by the contribution from unbound material in the outflow/jet structure close to the symmetry axis (see Hirose et al., 2004).

Note that construction of the 4-current, J^{μ} requires the construction of the time derivative of the electromagnetic field strength tensor, $F_{\mu\nu}$, which requires the use of three adjacent time steps for each simulation. Only one current density snapshot is available for each of the four simulations, corresponding to a late time in the simulation ($t = 8080GMc^{-3}$) and so we are limited to considering observational properties of the simulations corresponding to this particular snapshot.

6.4 Calculating the Observed Spectrum

The observed spectral properties of the accretion flow are determined by a complex convolution of the intrinsic (i.e. emitted) spectral shape with a description of dissipation, flow dynamics and the effect of gravity on photon propagation. The greatest uncertainty in these calculations lies in the first and second of these properties, as we do not possess a physical model relating the current density at a given point in the spacetime to the local heating rate at this point, nor do we possess a physical description relating the local heating distribution to the radiation spectrum. In Section 6.3, we saw that the local 4-current density may well provide a good description of dissipation within flow and so we adopt this description here.

Ignoring, for the moment, the effect of the intrinsic spectral shape, the flux measured by a distant observer from optically thin material within the disk body (i.e. 'bound' material), moving with 4-velocity u^{μ}_{e} may be written as (see e.g. Asaoka, 1989; Laor et al., 1990; Kurpiewski & Jaroszyński, 1999; Gierliński et al., 2001):

$$F_o(g) = \int\int\int g^2 T(g, \mu_o; r_e, \theta_e) ||J||^2 dr' d\theta' dg \tag{6.3}$$

Here, $||J||^2$ is the azimuthal average of the square of the 4-current density, $T(g, \mu_o; r_e, \theta_e)$ is the transfer function and dr', $d\theta'$ are the coordinate differentials measured in the co-moving rest frame of the emitting material (the 'fluid frame'). The observed redshift of a photon, g is determined via:

$$g = \frac{E_o}{E_e} = \frac{p_\mu u^\mu_o}{p_\mu u^\mu_e} \quad \text{where} \quad u^\mu_o = (1, 0, 0, 0) \tag{6.4}$$

Some fraction of the photons emitted from this optically thin material will cross the equatorial plane of the black hole. The flux received per unit radius, r_{eq} on this plane is given by (Laor et al., 1990):

$$F_{r_{eq}} = \frac{1}{dr'_{eq}} \int\int\int g^2 T(g, r_{eq}; r_e, \theta_e) ||J||^2 dr' d\theta' dg \tag{6.5}$$

In this case, the observed redshift of a photon, g is determined via:

$$g = \frac{E_{r_{eq}}}{E_e} = \frac{p_\mu u^\mu_{r_{eq}}}{p_\mu u^\mu_e} \text{ where } u^\mu_{r_{eq}} = u^t_{r_{eq}}(1, v^r_{r_{eq}}, v^\theta_{r_{eq}}, v^\phi_{r_{eq}}) \tag{6.6}$$

Note that both u^μ_e and $u^\mu_{r_{eq}}$ are obtained directly from the late-time data set corresponding to the 4-current density snapshot used to generate $||J^2||$.

To generate Iron Kα fluorescence line profiles, we assume that the equatorial plane is optically thick and that all incident photons are reprocessed into the line at a rest frame energy of 6.4keV. This corresponds to a radial emissivity pattern of the form $\varepsilon(r_e) \propto F_{r_{eq}}$. The Iron K$\alpha$ line measured by a distant observer is determined via (Laor, 1991):

$$F_o(g) = \int\int\int g^2 T(g, \mu_o; r_{eq}) \varepsilon(r_e) dr' dg \tag{6.7}$$

In this case (u^μ_o, $u^\mu_{r_{eq}}$ as previously defined):

$$g = \frac{E_o}{E_{r_{eq}}} = \frac{p_\mu u^\mu_o}{p_\mu u^\mu_{r_{eq}}} \tag{6.8}$$

6.5 Integration of Photon Trajectories

The fate of a photon emitted in some initial direction from a fluid element with spacetime coordinate (r_e, θ_e) is determined by the geodesic equations discussed at length in Chapter 3. Determining the relationship between the photons initial direction and its eventual fate requires the construction of a set of (analytically) invertible relationships between this direction and the photon angular parameters (λ, q). From the discussion of Section 3.3.3, it is apparent that, for a generally moving fluid element, no such expressions can be obtained. However, such relationships can be derived in the Locally Non-Rotating Frame (LNRF), where it is found that (see Section 3.3.2):

$$\lambda = \frac{\cos\Psi}{1 + \omega e^{\nu - \psi}\cos\Psi}; \quad q = e^{2(\mu_2 - \nu)}(1 - \lambda\omega)^2 \cos^2\Theta - \cos^2\theta \left[a^2 - \frac{\lambda^2}{\sin^2\theta}\right]; \tag{6.9}$$

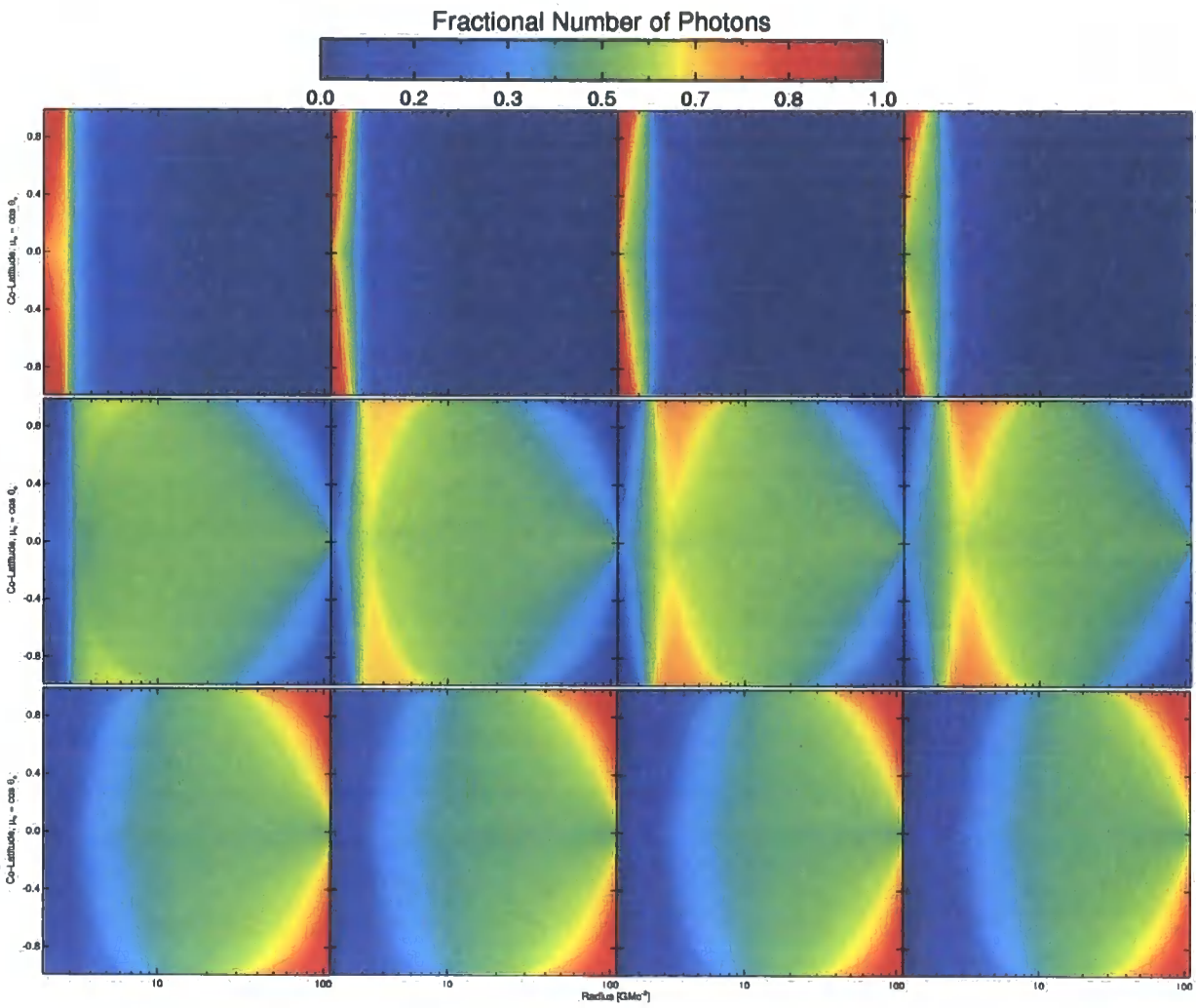

Figure 6.3: Maps of the fractional number of photons arriving at a particular destination as measured in the Locally Non-Rotating Frame (LNRF) attached to a particular spacetime point, r_e, μ_e. From left to right, the columns are maps for the KD0, KDI, KDP & KDE simulation data sets, which correspond to black hole spins of $a = 0.0, 0.5, 0.9, 0.998$ respectively. The rows are, from top to bottom, the fraction of photons captured by the black hole, the fraction crossing the equatorial plane within the disk body and the fraction reaching infinity. Each column is normalised to the peak intensity for a particular black hole spin which arrives at any of the three destinations. For further information, see text.

This enables us to quickly integrate photon trajectories and establish relationships between the initial direction of a photon (relative to the basis vectors of the LNRF) and its fate (i.e. capture by the black hole, crossing of the equatorial plane or escape to infinity).

Figure 6.3 shows maps of the fractional number of photons as measured in the LNRF for each of these possible fates as a function of (r_e, θ_e). If we were to emit an even distribution of photons in the LNRF at a particular (r_e, θ_e) point in spacetime, then the corresponding point on the map represents the probability that a photon arrives at a given destination for the black hole spin[1]. It is apparent that the majority of the the photons that are emitted below $3M$ are captured by the black hole, with 40% crossing the equatorial plane within the disk body. Above $3M$, only a very small fraction of the photons are captured by the black hole. In the region $3 - 10M$, as much as 70% of the emitted photons cross the equatorial plane, with the strength of this effect showing a strong correlation with black hole spin. This reflects the change in the lensing properties of the black holes with increasing angular momenta, as discussed by Beckwith & Done (2005). Above $10M$, the fraction of photons crossing the equatorial plane falls off to $\lesssim 50\%$, with virtually all the remaining photons escaping to infinity, as expected from a simple consideration of the solid angle subtended by the equatorial plane in regions where lightbending does not play a substantial role. In the outer regions of the simulation, the effects of the finite simulation volume become apparent, with the majority of the emitted photons escaping to infinity.

6.6 The Transfer Functions

The transfer functions, $T(g, \mu_o; r_e, \theta_e)$, $T(g, r_{eq}; r_e, \theta_e)$ and $T(g, \mu_o; r_{eq})$ are constructed from an even distribution of photons in the locally inertial rest frame of the emitting fluid element, the fluid frame. In our calculations, the photons are initially given an even

[1]Note that photons that cross the equatorial plane within the disk body are only counted within this category, i.e. we do not 'double count' photons

distribution in the LNRF and so this distribution must be transformed to an even distribution in the fluid frame. In our calculations, this frame is described by the construction of an orthonormal tetrad directly from the four-velocity of the fluid by use of a Gram-Schmidt orthogonalisation procedure (as described in Krolik et al., 2005). This approach is advantageous to that described in Section 3.3.3 as the resulting expressions are rather more compact.

The basis vectors are chosen so that physical interpretation is as straightforward as possible. In particular, the time-leg of the tetrad is chosen in the direction of the four-velocity of the fluid element (accomplished by setting $e^{\mu}_{[t]} = u^{\mu}$), which allows the easy identification of the direction of proper time in this observers frame. Additionally, this has the advantage that the time-leg of the tetrad automatically has the correct normalisation as the four-velocity of the fluid element is subject to the normalisation condition $u^{\mu}u_{\mu} = 1$. The choice of directions in three-space is ambiguous, however - many different approaches to their generation can be taken, all of which produce different (but equally correct) results. This mathematical ambiguity reflects the physical ambiguity in the choice of axes in three-space. We then orthonormalise the covariant components of the three-space legs of the tetrad in the order (ϕ, r, θ) in order to enable the closest possible comparison with Novikov & Thorne (1973). We obtain (see Figure 6.4):

$$\begin{aligned}
e^{\mu}_{[t]} &= u^{t} \left| \begin{array}{cccc} 1 & v^{r} & v^{\theta} & v^{\phi} \end{array} \right| ; \\
e^{\mu}_{[r]} &= N^{t}_{[r]} \left| \begin{array}{cccc} g_{tt} + g_{t\phi}N^{\phi}_{[r]} & g_{rr}N^{r}_{[r]} & 0 & g_{t\phi} + g_{\phi\phi}N^{\phi}_{[r]} \end{array} \right| ; \\
e^{\mu}_{[\theta]} &= N^{t}_{[\theta]} \left| \begin{array}{cccc} g_{tt} + g_{t\phi}N^{\phi}_{[\theta]} & g_{rr}N^{r}_{[\theta]} & g_{\theta\theta}N^{\theta}_{[\theta]} & g_{t\phi} + g_{\phi\phi}N^{\phi}_{[\theta]} \end{array} \right| ; \\
e^{\mu}_{[\phi]} &= N^{t}_{[\phi]} \left| \begin{array}{cccc} g_{tt} + g_{t\phi}N^{\phi}_{[\phi]} & 0 & 0 & g_{t\phi} + g_{\phi\phi}N^{\phi}_{[\phi]} \end{array} \right| ;
\end{aligned} \tag{6.10}$$

Here:

$$u^{t} = \frac{1}{\sqrt{-\left[g^{tt} + 2g^{t\phi}v^{\phi} + g^{rr}\left(v^{r}\right)^{2} + g^{\theta\theta}\left(v^{\theta}\right)^{2} + g^{\phi\phi}\left(v^{\phi}\right)^{2}\right]}};$$

$$N^t_{[r]} = \frac{1}{\sqrt{-\left[g^{tt} + 2g^{t\phi}N^\phi_{[r]} + g^{rr}\left(N^r_{[r]}\right)^2 + g^{\phi\phi}\left(N^\phi_{[r]}\right)^2\right]}};$$

$$N^r_{[r]} = -\frac{1}{v^r}(1 + N^\phi_{[r]}); \quad N^\phi_{[r]} = -\frac{g^{tt} + g^{t\phi}N^\phi_{[\phi]}}{g^{t\phi} + g^{\phi\phi}N^\phi_{[\phi]}};$$

$$N^t_{[\theta]} = \frac{1}{\sqrt{-\left[g^{tt} + 2g^{t\phi}N^\phi_{[\theta]} + g^{rr}\left(N^r_{[\theta]}\right)^2 + g^{\theta\theta}\left(N^\theta_{[\theta]}\right)^2 + g^{\phi\phi}\left(N^\phi_{[\theta]}\right)^2\right]}};$$

$$N^r_{[\theta]} = -\frac{1}{g^{rr}N^r_{[r]}}\left[g^{tt} + g^{t\phi}\left(N^\phi_{[r]} + N^\phi_{[\theta]}\right) + g^{\phi\phi}N^\phi_{[r]}N^\phi_{[\theta]}\right]; \quad N^\phi_{[\theta]} = -\frac{g^{tt} + g^{t\phi}N^\phi_{[\phi]}}{g^{t\phi} + g^{\phi\phi}N^\phi_{[\phi]}};$$

$$N^t_{[\phi]} = \frac{1}{\sqrt{-\left[g^{tt} + 2g^{t\phi}N^\phi_{[\phi]} + g^{\phi\phi}\left(N^\phi_{[\phi]}\right)^2\right]}}; \quad N^\phi_{[\phi]} = -v^\phi;$$

The photons four-momentum has moving frame components $p_{[\mu]} = p_\nu e^\nu_{[\mu]}$:

$$\begin{aligned}
p_{[t]} &= u^t\left[1 + s_r v^r\sqrt{R_{\lambda,q}(r)} + s_\theta v^\theta\sqrt{\Theta_{\lambda,q}(\theta)} - \lambda v^\phi\right];\\
p_{[r]} &= N^t_{[r]}\left[g_{tt} + g_{t\phi}N^\phi_{[r]} + g_{rr}N^r_{[r]}s_r v^r\sqrt{R_{\lambda,q}(r)} - \lambda\left(g_{t\phi} + g_{\phi\phi}N^\phi_{[r]}\right)\right];\\
p_{[\theta]} &= N^t_{[\theta]}\left[\begin{array}{r} g_{tt} + g_{t\phi}N^\phi_{[\theta]} + g_{rr}N^r_{[\theta]}s_r v^r\sqrt{R_{\lambda,q}(r)} \\ +g_{\theta\theta}N^\theta_{[\theta]}s_\theta v^\theta\sqrt{\Theta_{\lambda,q}(\theta)} - \lambda\left(g_{t\phi} + g_{\phi\phi}N^\phi_{[\theta]}\right)\end{array}\right];\\
p_{[\phi]} &= N^t_{[\phi]}\left[g_{tt} + g_{t\phi}N^\phi_{[\phi]} - \lambda\left(g_{t\phi} + g_{\phi\phi}N^\phi_{[\phi]}\right)\right];
\end{aligned} \tag{6.11}$$

The angles formed by the photon trajectory relative to the basis vectors of the fluid frame are given by (see Figure 6.4):

$$\cos\Sigma = \frac{p_{[\theta]}}{p_{[t]}}; \quad \sin\Sigma\sin\Xi = \frac{p_{[r]}}{p_{[t]}}; \quad \sin\Sigma\cos\Xi = \cos\Psi = -\frac{p_{[\phi]}}{p_{[t]}}; \tag{6.12}$$

The amount of emitted solid angle attached to each photon in the fluid frame is determined by means of a simple algorithm which calculates the area on the (Σ, Ξ)-plane associated with a given photon trajectory. The photons that are emitted with constant angular distribution in the Locally Non-Rotating Frame are then redistributed such that they

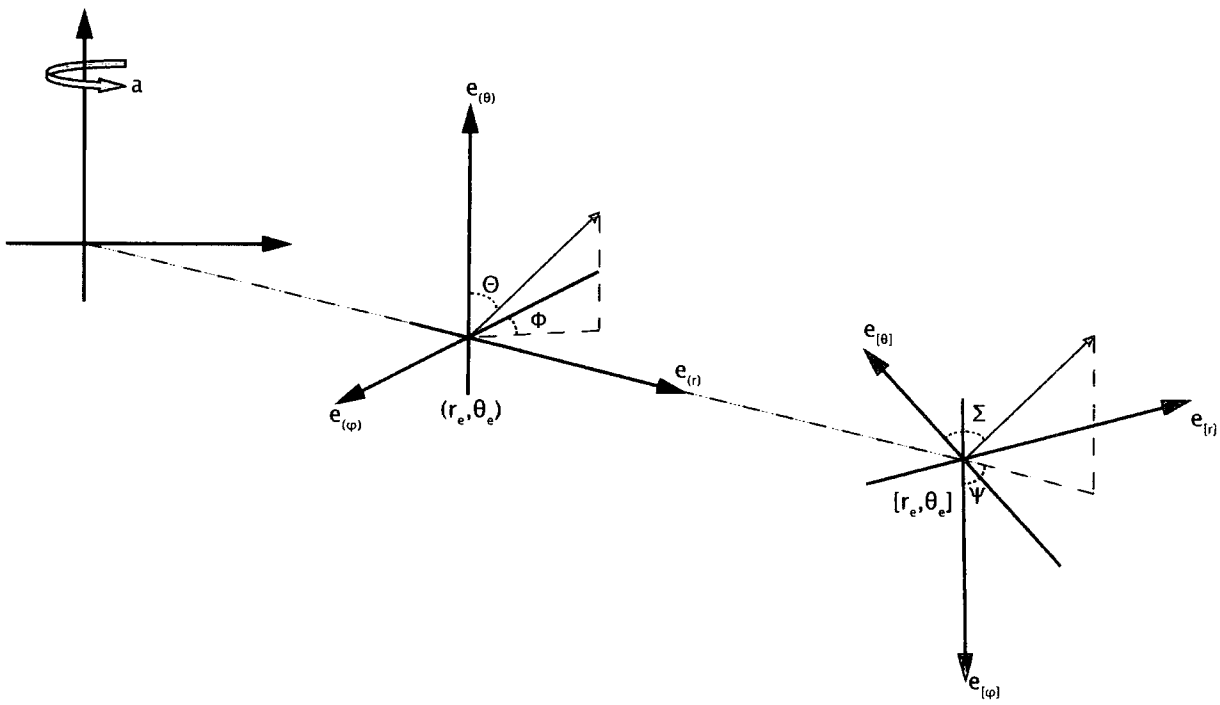

Figure 6.4: The co-ordinate systems associated with the Locally Non-Rotating Frame (LNRF, blue lines) and the Fluid Frame (green lines) associated with a particular emission point in the spacetime. We invert the simple relationships between the angles made by the photons 4-momenta in the LNRF, Θ, Φ and the conserved quantities λ, q to integrate the null geodesics. The angles made by the photons 4-momenta with the basis vectors in the fluid frame, Σ, Ψ are then obtained by through $p_{[\mu]} = p_\nu e^\nu_{[\mu]}$.

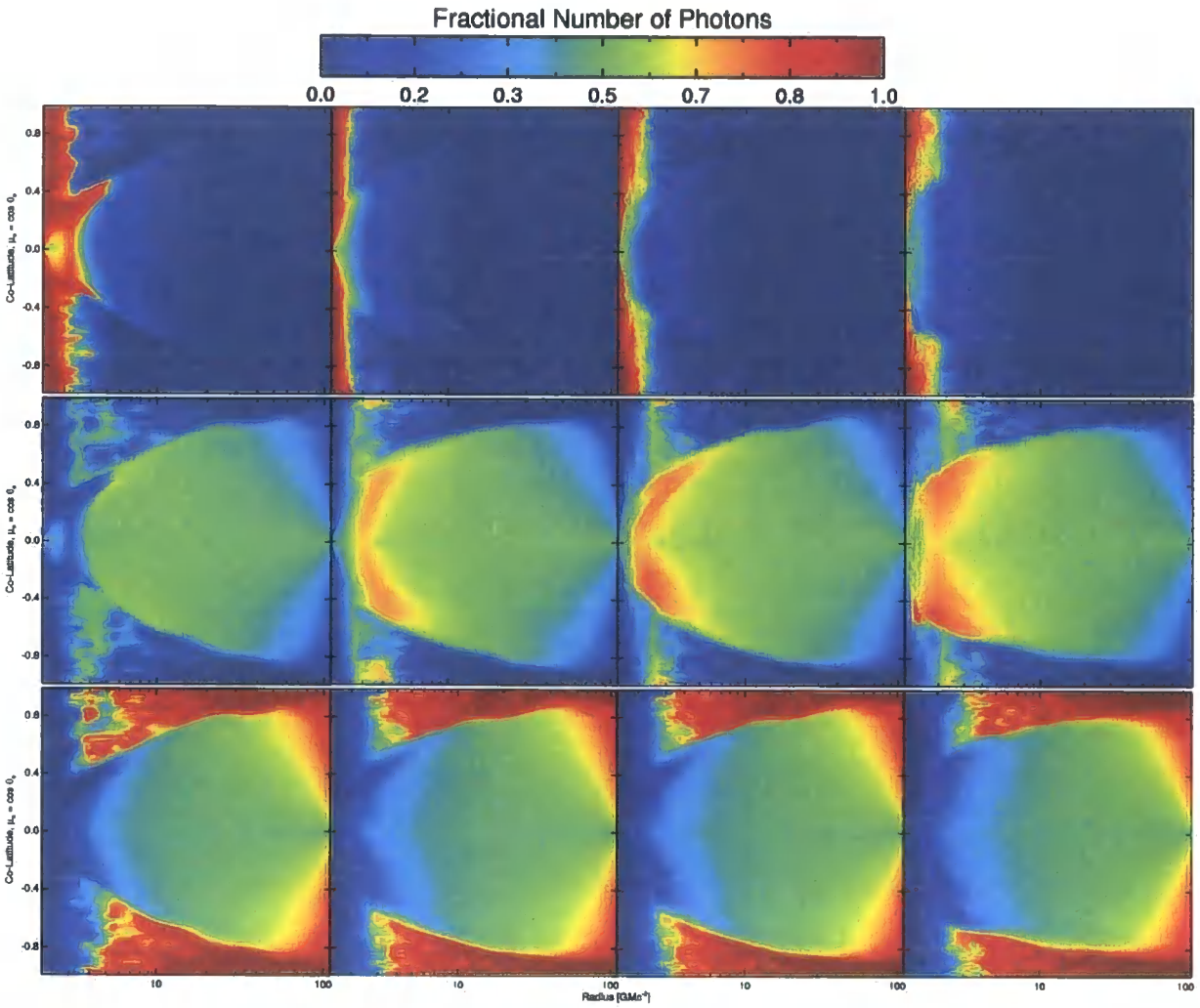

Figure 6.5: Maps of the fractional number of photons arriving at a particular destination as measured in the Fluid Frame (FF) attached to a fluid element at a particular spacetime point, r_e, μ_e. From left to right, the columns are maps for the KD0, KDI, KDP & KDE simulation data sets, which correspond to black hole spins of $a = 0.0, 0.5, 0.9, 0.998$ respectively. The rows are, from top to bottom, the fraction of photons captured by the black hole, the fraction crossing the equatorial plane within the disk body and the fraction reaching infinity. For further information, see text.

have an even distribution in the fluid frame, as specified by the fractional amounts of solid angle attached to each photon trajectory. These projections now enable us to create maps relating directions in the fluid frame to the three destinations of the trajectory outlined previously, which are shown in Figure 6.5. The principle difference between the maps shown in Figure 6.3 and those shown in Figure 6.5 is that those shown here contain the effects of the motion of the fluid elements. Relativistic beaming effects mean that the majority of the emission from rapidly moving material is directed in the direction of motion. Clearly, the majority of the photons from the rapidly outflowing material in the jet-like structures situated in the regions around the symmetry axis are directed to infinity, as can be seen from the bottom row of panels in Figure 6.5. Similarly, the majority of photons emitted from the rapidly infalling material in the inner regions of the flow are captured by the black hole. It is therefore far harder for photons from these two sources to illuminate the equatorial plane and thereby contribute to Iron Kα production.

6.7 Spectral Diagnostics of Optically Thin, Geometrically Thick Accretion Flows

In Figures 6.4 and 6.5, we show dynamical spectra and convolution kernels describing optically thin, bound material for each of the KD simulations. These spectra include photons that cross the equatorial plane, possibly on multiple occasions. In terms of the observed states of real accretion flows, this is most likely to correspond to the hot inner flow in the proposed geometry for the hard state of low mass X-ray binary systems (see e.g. Zdziarski & Gierliński, 2004). These spectra should therefore be interpreted as convolution kernels for the broad band X-ray spectrum, such as those discussed for an geometrically thin, optically thick accretion disk in Section 2.5.

Reynolds & Begelman (1997), in the context of Iron Kα line profiles, showed that emission below r_{ms} acts to broaden the line in the case of the Schwarzschild hole. Figures

6.4 and 6.5 demonstrate that the spectra resulting from emission from optically thin, bound material are generically broad, independent of black hole spin. The spectral shape is, however, strongly dependent on the black hole spin and is a result of a complex interplay of the flow dynamics and dissipation profile.

For the slowly rotating holes, the spectra strongly resemble the profiles due to standard accretion disks, with the addition of a broad component in the red wing of the line, which has its origin in the rapidly infalling material in the plunging region. As black hole spin increases, we observe a corresponding increase of the relative amount of flux contained within this component relative to the blue wing of the line, as can be clearly seen from Figure 6.5. Photons emitted from material on the near side of the black hole must be emitted in a direction opposite to that of the materials motion and so arrive at the observer with their energies much reduced. Photons emitted from the rapidly infalling material on the far side of the hole are strongly concentrated in the direction of the hole and so are captured, rather than being able to propagate to the distant observer. A large fraction of the photons ($\sim$ 90%) forming this component perform multiple crossings of the equatorial plane, as described in Chapters 3 and 5, which, when combined with the marked increase in dissipation in the inner regions of the flow, results in the increase in the relative strength of the red wing component with increasing black hole spin. Gravitational lensing is always important for optically thin, geometrically thick flows as a significant amount of flux is carried by these photons.

There is a marked difference between the spectral shapes associated with the two fastest rotating black holes, KDP and KDE. Recall that for KDP, which corresponds to $a = 0.9$, $r_{ms} = 2.32$, whilst for KDE, corresponding to $a = 0.998$, $r_{ms} = 1.235$. Below $\sim 3M$, material in the KDP simulation is rather rapidly infalling. As noted in Krolik et al. (2005), there is a marked decrease in the radial infall velocities for material within the disk for the most rapidly rotating black hole, KDE. In fact, examination of the azimuthally averaged velocity field used to generate the spectra reveals that bound material within the

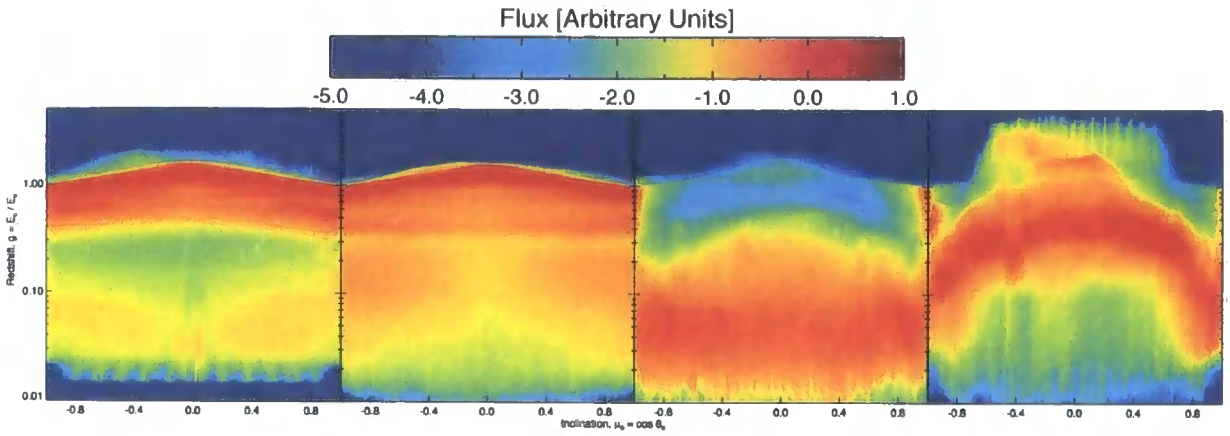

Figure 6.6: Dynamical spectra of optically thin, bound material. From left to right, the panels are maps for the KD0, KDI, KDP & KDE simulation data sets, which correspond to black hole spins of $a = 0.0, 0.5, 0.9, 0.998$ respectively. The spectra for each inclination along the x-axis are normalised such that each slice along constant x contains one photon. There is a clear distinction between spectra associated with the slowly rotating holes (KD0, KDI) and those associated with rapidly rotating holes (KDP, KDE).

KDE accretion flow is predominantly Keplerian, down to the event horizon, in marked contrast to the more slowly rotating cases. Furthermore, a large fraction of the total dissipation within the flow occurs close to the black hole event horizon in the KDE case, strongly weighting the resultant spectra to these regions. Photons emitted from the inner regions of the flow therefore exhibit a substantially different energy distribution (as measured by the distant observer) to those associated with the more slowly rotating holes. A large fraction of these photons are strongly lensed by the black hole, which, in combination with the changed dynamics and dissipation profiles, results in the distinctive crescent shape observed in Figure 6.6.

It is clear from Figures 6.6 and 6.7 that the differences between the convolution kernels for different black hole spins are most apparent when the observer is close to the equatorial plane, so that the differing properties of the inner regions of the accretion

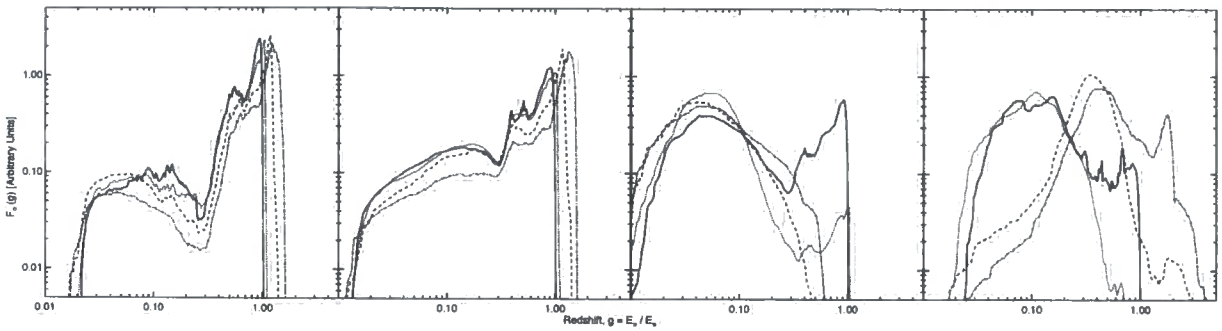

Figure 6.7: Convolution Kernels for Optically Thin, Geometrically Thick Accretion Flows. From left to right, the panels are maps for the KD0, KDI, KDP & KDE simulation data sets, which correspond to black hole spins of $a = 0.0, 0.5, 0.9, 0.998$ respectively. On each panel we show four different lines corresponding to different inclinations of the observer: (i) 11° (solid lines); (ii) 30° (dotted lines); (iii) 60° (dashed lines); (iv) 89° (dot-dash lines). Each kernel corresponds to a slice through the dynamical spectra show in Figure 6.6 and again is normalised to one photon. It is clear that there is a marked contrast between the spectral shape associated with slowly and rapidly rotating holes

flow can be enhanced by the combined effects of gravitational lensing, Doppler boosting and special relativistic length contraction. The best prospect for testing these accretion models is therefore by observations of a highly inclined galactic black hole system, such as XTEJ1550-564 ($\theta_o = 70°$, see Gierliński & Done, 2003, and references therein) in the low hard/state. Indeed, the April 2000 observation carried out by the PCA & HEXTE detectors on board NASAs Rossi X-ray Timing Explorer (RXTE) caught this source in such a state. In Figure 6.8 we show the Comptonising continuum associated with the approximate best fit to this data set using the `EQPAIR` model (Coppi, 1999) within `XSPEC` (Arnaud, 1996), assuming either a purely thermal (left-hand panel) or alternatively a non-thermal distribution (right-hand panel). For each type of distribution, we convolve the best-fit spectrum with the appropriate kernel for each of the KD accretion flows, which are shown in Figure 6.8 by the red lines (KD0), green lines (KDI), blue lines (KDP) and

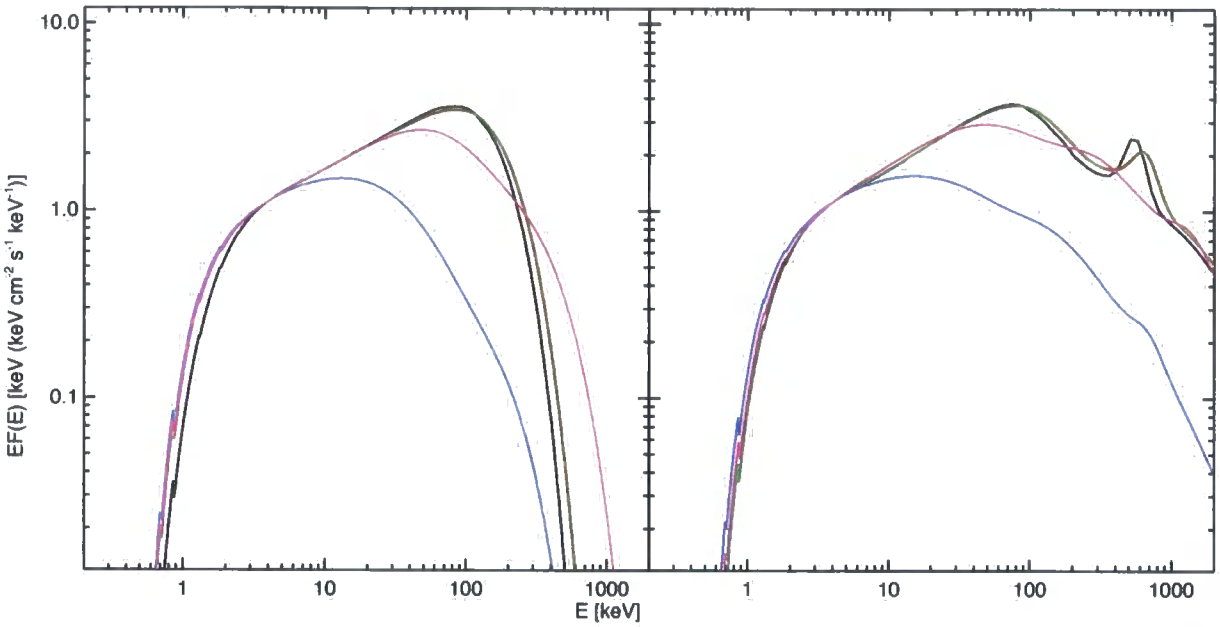

Figure 6.8: Model Spectra for the April 2000 simultaneous PCA & HEXTE observations of XTEJ1550-564 in the low/hard state. The inclination of the source is taken to be 70°. The models are generated using the `EQPAIR` model within `XSPEC`, assuming either a purely thermal (left-hand panel) or alternatively a non-thermal distribution (right-hand panel) for particles within the corona (left-hand panel). For each type of particle distribution, the approximate best fitting, unconvolved spectrum is shown by the black line. Red lines denote the spectrum convolved with the $a = 0$ flow, green lines the spectrum convolved with the $a = 0.5$ flow, blue lines the spectrum convolved with the $a = 0.9$ flow and magenta lines lines the spectrum convolved with the $a = 0.998$ flow. The principal effect of increasing black hole spin is to broaden the continuum shape, in particular the high energy cutoff at $\sim$ 100keV.

magenta lines (KDE). The principle effect of black hole spin on the thermal spectrum is to change the shape of the high energy cutoff, which becomes broader as black hole spin is increased (until the most rapidly rotating case). For the non-thermal spectrum, increasing black hole spin again broadens the high-energy cutoff at $\sim$ 100keV. There is also now an additional effect on the (as yet unobserved) annihilation lane at 511keV, which becomes substantially broader with increasing black hole spin (again until the most rapidly rotating case for both effects).

6.8 Generation of Broad Iron Kα Lines

The second approach to calculating spectral diagnostics of these accretion flows, generation of Iron Kα profiles is more complex. As outlined in Section 6.4, we assume that the accretion flow is optically thick in the equatorial plane and illuminate this surface with photons emitted from both bound and unbound material in the surrounding simulation volume, which are reprocessed into a fluorescent Iron Kα line and propagated to a distant observer.

Figure 6.9 shows the illumination patterns generated by this model for the four different KD simulations. For each simulation, two different illumination models are shown - solid lines denote the illumination pattern generated by bound material and dotted lines the pattern generated by unbound material. Generically, the illumination patterns take the form $\varepsilon(r_e) \propto r_e^{-q}$, where $q \sim -2$ for illumination by unbound material (independent of black hole spin). In the case of illumination by bound material, $q \sim -3$ for the slowly rotating black holes (KD0,KDI), steepening to $q \sim -4$ for the rapidly rotating holes.

For illumination of the surface by bound material, simple considerations of the release of gravitational potential energy indicate that we should expect a dependence of the illumination pattern on radius approximately matching r^{-3}. The proposed geometry for the soft state of galactic X-ray binaries consists of a thin, cold accretion disk, extending down to the last stable orbit, surrounded by an optically thin, Comptonising corona.

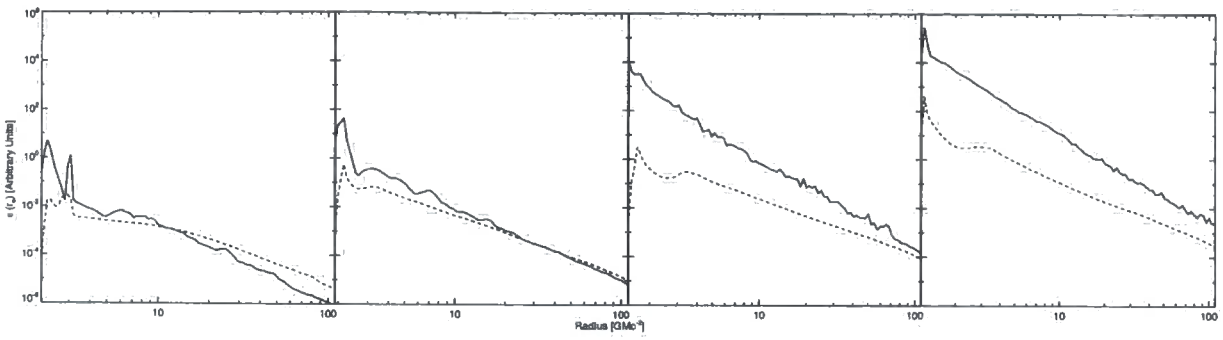

Figure 6.9: Plots of Iron Kα emissivity, $\varepsilon(r_e)$ for a simple reflection geometry. From left to right, the panels are maps for the KD0, KDI, KDP & KDE simulation data sets, which correspond to black hole spins of $a = 0.0, 0.5, 0.9, 0.998$ respectively. Solid lines denote the illumination pattern generated by bound material and dotted lines denoting the illumination pattern generated from unbound material.

Active regions/flares in this corona reprocess soft seed photons from the cold disk, which are Compton up-scattered to higher energies. These hard X-ray photons are then reflected by the disk and are responsible for the Iron Kα fluorescence observed in many systems. The radial dependence of the illumination pattern is therefore determined by the density of the active regions performing the Compton up-scattering, which should be approximately proportional to the release of gravitational potential energy. In Section 6.3, we saw that the 4-current density provides a close match to the dissipation function derived in the standard relativistic disk model. In the calculations presented in this section, we have used the 4-current density (convolved with the appropriate transfer functions) to provide a description of the illumination pattern responsible for Iron Kα fluorescence. The close match between the resulting illumination patterns for the slowly rotating holes and the expectation from the standard disk model further encourages us in our choice of the 4-current density in describing the underlying dissipation in the flow. In the rapidly rotating cases, dissipation in the inner regions of the flow is significantly enhanced in comparison to the standard case, which results in the steeper coronal illumination pattern exhibited

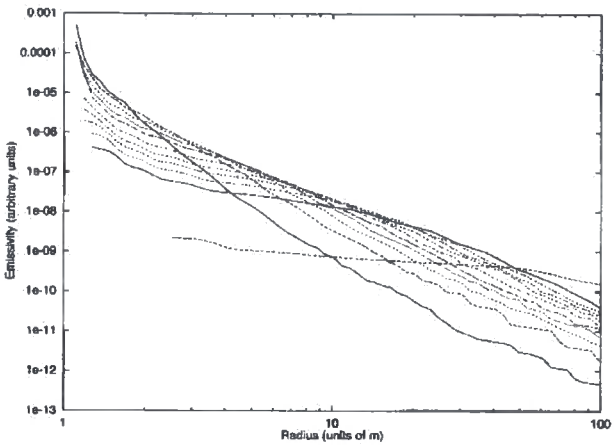

Figure 6.10: "Emissivity laws $I(r)$ (in arbitrary units) corresponding to different source heights above an extreme Kerr hole, as discussed in Martocchia & Matt (1997). Looking at the right side of the diagram the curves correspond, from top to bottom, to heights of 100, 20, 15, 12, 10, 8, 6, 5, 4, 3 and 2 (units of m). The curves steepen when h decreases, which corresponds to increasing anisotropy of emission." Taken from Martocchia et al. (2000)

in Figure 6.9

The alternate illumination mechanism, due to unbound material, is similar to that suggested by several authors previously as the lamppost model (see e.g. Martocchia et al., 2000, and references therein). In this model, illumination of the disk is provided by a discrete, stationary source located on (or close to) the symmetry axis of the black hole at some height, h above a standard relativistic disk. The resultant illumination patterns for this model are shown in Figure 6.10. In our approach, the illumination of the surface is provided by an an extended distribution of rapidly outflowing sources, a rather different physical scenario to that proposed in the lamppost model. Photons emitted from the rapidly out-flowing fluid elements are directed away from the inner regions of the disk. Those that do illuminate the disk are concentrated to large radii, enhancing the illumination in these regions. This results in the rather shallow illumination patterns

shown in Figure 6.9

In Figures 6.10 and 6.11 we show the Iron Kα profiles generated for the illumination pattern due to emission from either bound or unbound material shown in Figure 6.6. For a given black hole spin, the profiles due to illumination by bound material are significantly broader than those due to unbound material, reflecting the difference between these two illumination patterns. The line becomes broader with increasing black hole spin, although this effect is less pronounced than in the standard disk case (c.f. Figure 4.6). Consider the lines resulting from illumination by bound material. Here, there is a clear dichotomy between the rapid and slow rotating holes. The underlying dissipation is more strongly peaked towards the inner regions in the rapidly rotating cases, resulting in a steeper illumination pattern. This change is reflected in the properties of the line, which, for the rapidly rotating holes, contains far more flux in the red wing in comparison to the slowly rotating case.

In the standard model of relativistic accretion disks, the width of the Iron Kα line is used as a diagnostic of the black hole spin (see Section 2.5). From Figures 6.10 and 6.11, it is apparent that although the derived widths of the Iron Kα lines are correlated with black hole spin, this dependence is far less pronounced than the standard case. Figure 6.13 shows an explicit comparison of the lines generated from the KD simulations with those predicted from the standard model of accretion disks. To generate the standard disk line profiles, we have assumed a radial emissivity law of the form $\varepsilon(r_e) = r^{-q}$ and an angular emissivity law $f(\mu_e) = 1$. The power law index, q is chosen to be -2 for comparison with lines produced by the illumination pattern due to unbound material. Similarly, we take $q = -3, -4$ for comparison with the lines due to illumination by bound material for slowly rotating and rapidly rotating holes, respectively. As expected from Reynolds & Begelman (1997), the lines from the KD simulations are generically far broader than those predicted from the standard disk model, with a large excess of flux in the red wing of the line.

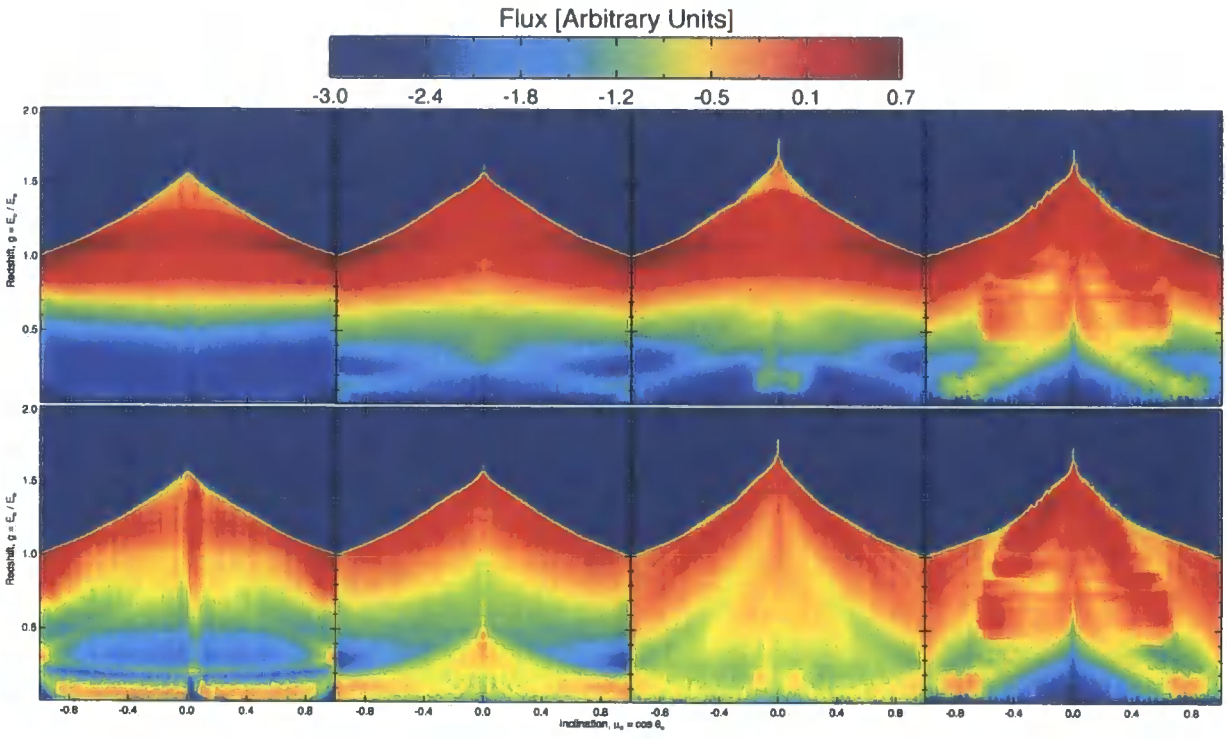

Figure 6.11: Dynamical Iron Kα profiles for a simple reflection geometry. From left to right, the panels are maps for the KD0, KDI, KDP & KDE simulation data sets, which correspond to black hole spins of $a = 0.0, 0.5, 0.9, 0.998$ respectively. Profiles on the top row are generated using the illumination pattern from unbound material, those on the bottom using the illumination pattern from bound material (both shown in Figure 6.9). The spectra for each inclination along the x-axis are normalised such that each slice along constant x contains one photon. The width of the profiles clearly increases with increasing black hole spin. Additionally, the lines associated with the rotating holes exhibit an excess of flux in both the red (at low inclinations) and blue wings (at high inclinations) in comparison to the non-rotating case.

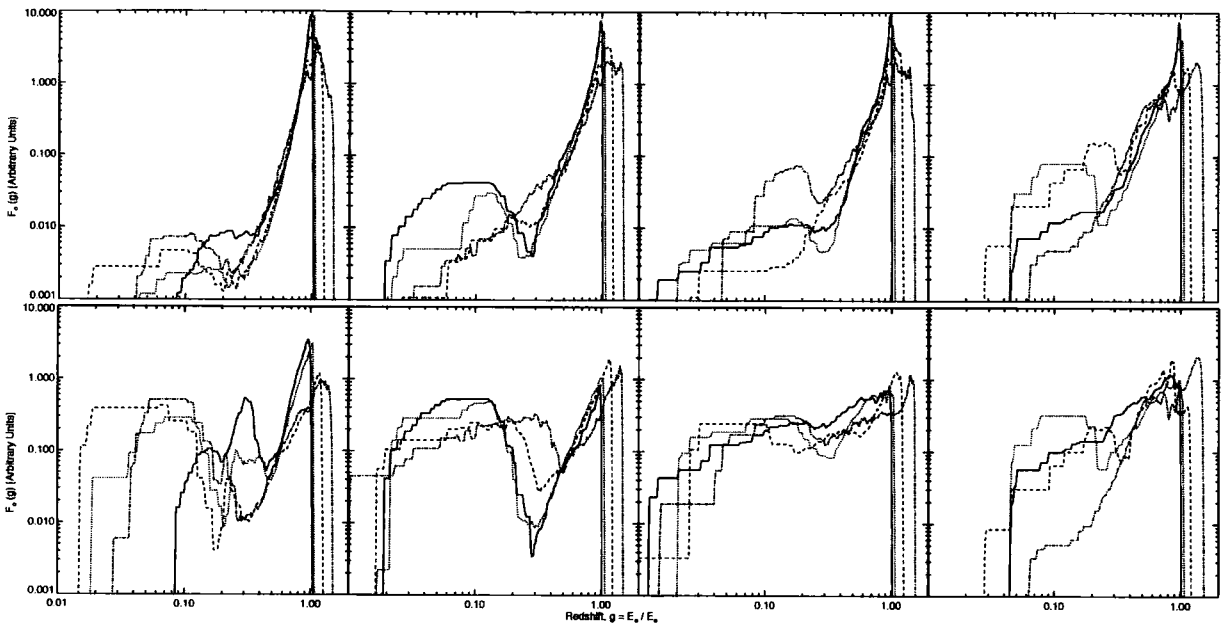

Figure 6.12: Selected Iron Kα profiles for a simple reflection geometry. From left to right, the panels show lines for the KD0, KDI, KDP & KDE simulation data sets, which correspond to black hole spins of $a = 0.0, 0.5, 0.9, 0.998$ respectively. Profiles on the top row are generated using the illumination pattern from bound material, those on the bottom using the illumination pattern from unbound material (both shown in Figure 6.6). On each panel we show four different lines corresponding to different inclinations of the observer: (i) 11° (solid lines); (ii) 30° (dotted lines); (iii) 60° (dashed lines); (iv) 89° (dot-dash lines). Each profile corresponds to a slice through the dynamical spectra shown in Figure 6.10 (at the given inclination) and again is normalised to one photon. For the slowly rotating holes, the principle effect of increasing inclination is to increase the relative amounts of flux in the blue wing of the line. For the rapidly rotating holes, increasing inclination results in the line becoming far more centrally concentrated.

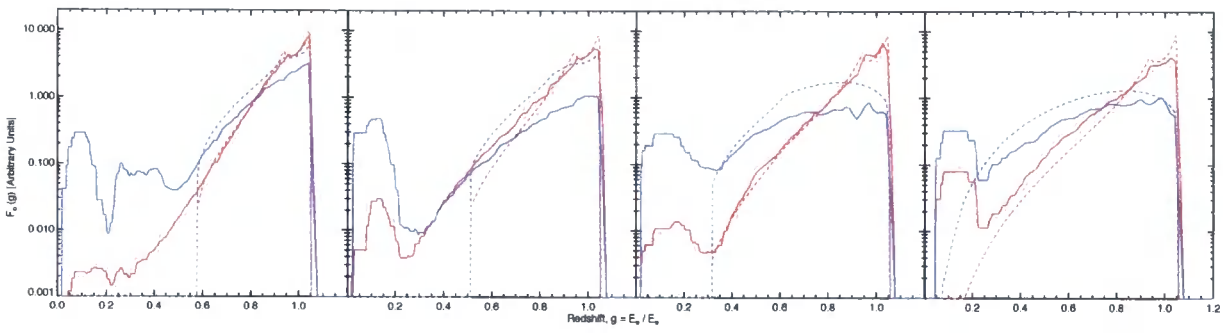

Figure 6.13: Explicit comparison of Iron Kα profiles generated from KD Simulations and the standard disk model. From left to right, the panels show lines for the KD0, KDI, KDP & KDE simulation data sets, which correspond to black hole spins of $a = 0.0, 0.5, 0.9, 0.998$ respectively. The inclination of the observer is taken to be 30°. On each panel we show four different lines corresponding to (i) lines generated from the KD simulation using illumination by bound material (blue lines); (ii) lines generated from the KD simulation using illumination by unbound material (red lines); (iii) lines generated from the standard model assuming $\varepsilon(r_e) \propto r_e^{-3}$ for slowly rotating holes or $\varepsilon(r_e) \propto r_e^{-4}$ for rapidly rotating holes (blue dashed lines) (iv) lines generated from the standard model assuming $\varepsilon(r_e) \propto r_e^{-2}$ (blue dashed lines). Each profile is normalised to one photon. Generically, the lines generated from the KD simulations are far broader than those predicted by the standard model, as expected from Reynolds & Begelman (1997)

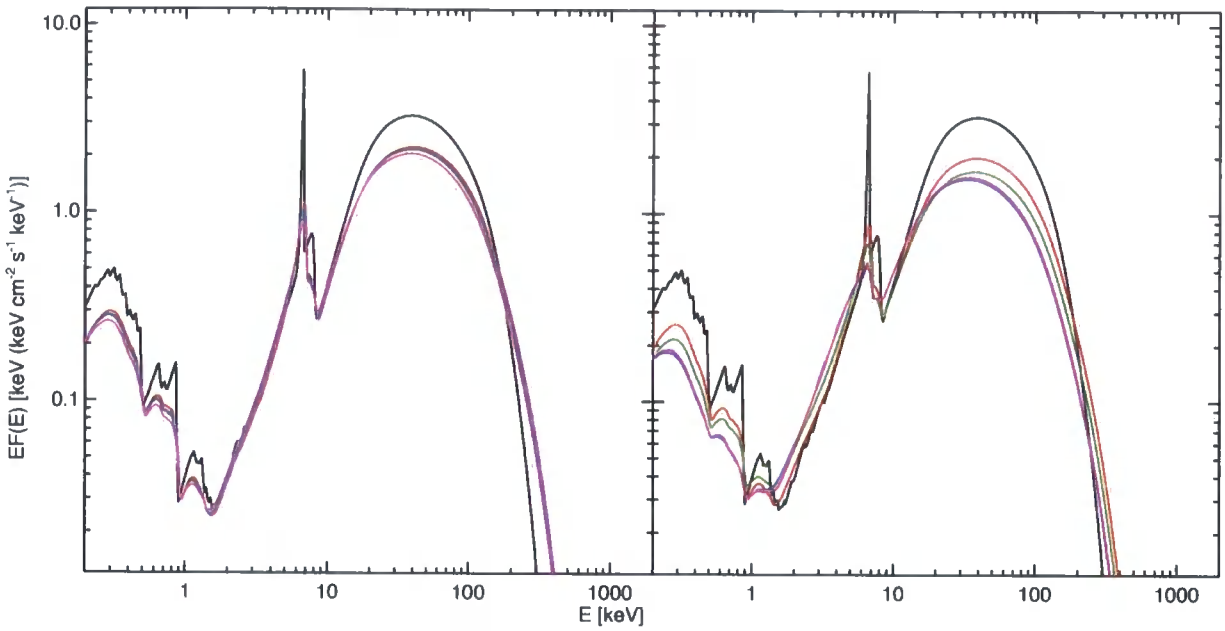

Figure 6.14: Model reflection spectra for cold, neutral material. The inclination of the observer is taken to be 30°. The unconvolved spectrum (black lines) is generated using the `THCOMPML` model within `XSPEC`. On the left-hand panel, we show the effect of convolving this spectrum with the appropriate kernel for each black hole spin where the illumination pattern is provided by unbound material. On the right-hand panel, we show the effect of convolving this spectrum with the appropriate kernel for each black hole spin where the illumination pattern is provided by bound material. Red lines denote the spectrum convolved with the $a = 0$ flow, green lines the spectrum convolved with the $a = 0.5$ flow, blue lines the spectrum convolved with the $a = 0.9$ flow and magenta lines lines the spectrum convolved with the $a = 0.998$ flow. The most prominent change in the reflection spectrum is observed for illumination by bound material, due to the dichotomy between slowly and rapidly rotating black holes.

A realistic direct comparison of the effects of the transfer function between the different black hole spins is best accomplished by examining their effect on the reflection spectrum, rather than solely the line. In Figure 6.14 we show the reflection spectrum due to cold, mostly neutral material ($\xi = 100$ ergs cm s^{-1}) generated by the `XSPEC` model `THCOMPML` (black lines, see Zdziarski et al., 1996; Życki et al., 1999) convolved with with the 30° kernel for KD0 (red lines), KDI (green lines), KDP (blue lines) and KDE (magenta lines). On the left-hand panel, we show the resultant spectra when the illumination pattern is generated from unbound material, the right-hand panel using bound material. In the former case, black hole spin plays only a small ($\sim$ 5%) role in shaping the observed reflection spectra. However, in the latter case, the effect of black hole spin is rather more pronounced, with a clear distinction between the slowly and rapidly rotating holes, due to the changed illumination pattern. Not only does the line become broader with increasing spin, but additionally the relative height between the peak of the Iron Kα line at $\sim 6keV$ and the end-point of the Iron edge at $\sim 7keV$ decreases. However, we caution that this feature is strongly dependent on the underlying ionisation state of the material, as can be seen from the right-hand panel of Figure 2.6.

6.9 Conclusion

We have presented a series of calculations based on the results of the Keplerian Disk (KD) simulations which have been presented in a series of papers by De Villiers et al. (2003); Hirose et al. (2004); De Villiers et al. (2005); Krolik et al. (2005). These calculations employ a modified form of the strong gravity code described by Beckwith & Done (2004, 2005) to determine various observational properties of these global, general relativistic magneto-hydrodynamic accretion flows.

We assume that the rest frame emission intensity follows the heating distribution within the simulation, which in turn corresponds to regions of high current density, as proposed by Rosner et al. (1978). Explicit comparison of this choice with the dissipation

derived in the context of the standard relativistic disk model exhibits a surprisingly close match between the two descriptions. To calculate observational diagnostics of these accretion flows, our calculations take two distinct approaches. In the first, we assume that the accretion flow is optically thin and consider emission from bound material. This emission is used to generate convolution kernels for the optically thin, hot inner flow thought to be present in the low/hard state of low mass X-ray binaries, such as XTEJ1550-564 (Zdziarski & Gierliński, 2004). All of the kernels are broader than those expected from a standard accretion disk. Those associated with slowly rotating holes are intrinsically narrower than those associated with the rapidly rotating cases, with a large number of the observed photons strongly modulated by strong gravitational lensing effects. If the low/hard state of low mass X-ray binaries really does consist of a hot optically thin inner flow *and* if this flow is described by KD simulations, then the shape of the high-energy spectral cut-off is modulated strongly modulated by black hole spin. Observationally, this spectral feature is rather sharp, which may be incompatible with the spectral shapes associated with rapidly rotating black holes.

In the second approach, we assume, *a priori*, that the accretion flow is optically thick in the equatorial plane. Hard X-ray photons are emitted throughout the rest of the simulation volume, with the emitted intensity tracing the heating distribution in the rest frame of the emitter. The photon trajectories are traced to the equatorial plane and illumination patterns for emission from both bound and unbound material calculated. Both types of illumination pattern are similar and are well described by $\varepsilon(r) \propto r^{-q}$, where $q = -2$ for illumination by unbound material (the jet) and $q = -3, -4$ for illumination by bound material (the corona) for slowly and rapidly rotating black holes respectively.

We find that the properties of Iron Kα lines generated from these modern descriptions of the accretion flow exhibit rather different characteristics to those predicted from the standard relativistic accretion disk model. However, there still exists a clear correlation between these properties and the rotation of the hole, although much less distinct than for

the standard case. The principle origin of this change is the fact that the accretion flow extends below the marginally stable orbit in these simulations. This results in the line extending to lower energies, regardless of black hole spin, as expected from Reynolds & Begelman (1997). However, if the disk is illuminated by bound material within the corona, the lines associated with slowly and rapidly rotating holes are rather different, reflecting the changed radial dependence of the illumination pattern. We caution, however, that this results is likely to be strongly sensitive to changes in the reflection model. Additionally, it is important to note that the emission from the surface is assumed to be isotropic in the rest frame of the emitting material and as such these lines do not taken account of the issues concerning limb-darkening/brightening (see Beckwith & Done, 2004). Other important questions remain, in particular the effect of introducing a physical description of the location of the disk surface, which is likely to have a significant impact on the coronal illumination model. These calculations are currently in progress and will be presented in a future work.

Chapter 7

Summary & Conclusions

Einstein's crowning achievement, the General Theory of Relativity, for the first time provides a physical description of the origin of the Gravitational force, whilst resolving the fundamental contradiction between Newtonian gravity and the Special Theory of Relativity. From an experimental standpoint, General Relativity has been remarkably successful, passing every test to which it has been subject, from the advance of the perihelion of Mercury to the bending of light rays by the gravitational field of the Sun. The theories most remarkable predictions concern the properties of spacetime where the gravitational field is so strong that not even light can escape, the black hole. Such objects are thought to exist in many astronomical systems, from Black Hole Binaries to Active Galactic Nuclei. By attempting to understand the observed properties of these systems, we can hope to test the properties of the gravitational field and hence confirm that General Relativity does indeed provide an accurate physical description of the properties of black holes.

In the past two decades, the launch of a series of high-resolution high energy X-ray satellites have yielded remarkable new insights into the properties of these systems. For stellar mass black holes contained within Black Hole Binaries (where mass transfer occurs via Roche Lobe overflow), it is possible to explain the bewildering variety of observed phenomena in terms of a two-phase accretion flow. Spectra dominated by a blackbody component in the soft X-rays are explained in the context of a cool accretion disk, which may be accompanied by an optically thin corona that Compton scatters soft seed photons

into the observed hard X-ray tail. By contrast, spectra that are hard X-ray dominated are interpreted as consisting of a hot inner flow, which undergoes a transition to the cool disk at large radii from the black hole.

Attempts to explain these observations theoretically can be traced back to the standard disk model developed due to Novikov & Thorne (1973), based on Shakura & Sunyaev (1973). Gas accreted onto black holes is likely to be in possession of large amounts of angular momentum, leading to the formation of a structure known as an accretion disk. For the gas to be accreted onto the black hole, angular momentum must be transported out through the disk, allowing material to fall inwards. If we assume that there is some local viscosity mechanism capable of driving this process, then we are lead to the standard model of relativistic accretion disks. Over the past three decades, it has become apparent that this description of accretion disks has many shortcomings, not least of which is the absence of any physical mechanism capable of providing the required local viscosity. In fact, the only physical mechanism capable of providing the required levels of angular momentum transport is the Magneto-Rotational Instability (Balbus & Hawley, 1991), which is fundamentally non-viscous. In this description, accretion disks are rather different to the standard model (see Section 2.4).

In reality, the observed spectra are more complex. Illumination of cool gas by hard X-ray photons results in a complex reflection spectrum that is observed in many systems. Dependent on the ionisation state of the gas, this spectrum contains an intrinsically narrow feature due to Iron Kα fluorescence at $\sim$ 6.4 keV. The photons that form this spectral feature originate in rapidly moving material, close to the black event horizon. They are therefore subject to the combined dynamical effects of the accretion disk and those of General Relativity, resulting in a highly broadened Iron Kα line. The observed form of the line can then, in principle, be used as a test of the strong gravitational field of the black hole.

In Chapter 3, we detailed how calculations of the spectral properties of accretion

flows in the strong gravitational field of a rotating black hole are performed. The null geodesic equations governing photon propagation were derived and reformulated to enable the rapid calculation of large numbers of photons trajectories. We outlined how physical properties may be evaluated in the local-rest frame of the disk by means of the tetrad formalism, before finally showing how all these calculations can be combined to generate observed spectra.

In Chapter 4, we applied a fast, accurate strong gravity code developed from this description to determine the expected shape of the Iron Kα line. We compared our results to those predicted by the `XSPEC` models `diskline` (Fabian et al., 1989) and `laor` (Laor et al., 1990), finding a close match ($\sim 5\%$) between the codes. However, the `diskline` and `laor` models make very specific assumptions regarding the (poorly understood) vertical structure of the accretion disk, which may not be correct. We demonstrate that these assumptions strongly affect the radial emissivity derived from measurements of the line shape, which has important consequences for interpretation of observed broad lines, in particular those seen in MCG-6-30-15.

Chapter 5 extends these calculation to consider the contribution of orbiting photons to the observed properties of standard accretion disks. For high-inclination systems, these photons carry a substantial fraction of the total luminosity of the system back to the disk at a range of radii. However, for low-inclination systems containing slowly rotating black holes, these photons may be able to escape through the gap between the inner edge of the accretion disk and the position of the photon orbits. This is potentially observable for supermassive black holes with the proposed X-ray interferometer, MAXIM, and as such has the potential to provide an observational test of strong field gravity.

Finally, in Chapter 6, we move away from the standard relativistic disk model and examine the observational properties of accretion flows where angular momentum transport is provided by the Magneto-Rotational Instability. Currently, there is no explicit physical description of how dissipation occurs within these flows. However, we are able to

show that there is a close correspondence between the magnetic 4-current density and the expected dissipation profile derived from the standard relativistic accretion disk models. Taking dissipation within the simulation to be proportional to this quantity, we show that if the flows are optically thin, then there are observable consequences for the spectra of Galactic Black Holes in the low / hard state. In an alternative approach, we calculate Iron Kα profiles using a simple reflection geometry, which exhibit rather different characteristics to those predicted from the standard relativistic accretion disk model, originating in the markedly different dynamics of the accretion flow.

It is clear therefore that the observed properties of Iron Kα profiles are dependent not only on the well-understood effects of strong gravity, but also on the poorly understood physics of accretion. Line profiles show a clear dependence on black hole spin, but the details of their shape are strongly dependent on both the vertical structure and dynamics of the reflecting material. Before we can make robust, detailed conclusions regarding the observed properties of the Iron Kα line, we will need to have a much better understanding of the physics of accretion.

Bibliography

Abramowicz, M. A., & Kluźniak, W. 2001, A&A, 374, L19

Afshordi, N., & Paczyński, B. 2003, ApJ, 592, 354

Agol, E. 1997, Ph.D. Thesis

Agol, E., & Krolik, J. H. 2000, ApJ, 528, 161

Antonucci, R. R. J., & Miller, J. S. 1985, ApJ, 297, 621

Armitage, P. J. 2004, Theory of Disk Accretion onto Supermassive Black Holes (ASSL Vol. 308: Supermassive Black Holes in the Distant Universe), 89–+

Arnaud, K. A. 1996, in ASP Conf. Ser. 101: Astronomical Data Analysis Software and Systems V, 17–+

Asaoka, I. 1989, PASJ, 41, 763

Balbus, S. A., & Hawley, J. F. 1991, ApJ, 376, 214

—. 1998, Reviews of Modern Physics, 70, 1

Ballantyne, D. R., Ross, R. R., & Fabian, A. C. 2001, MNRAS, 327, 10

Bao, G., Hadrava, P., & Ostgaard, E. 1994, ApJ, 435, 55

Bardeen, C. T., & Cunningham, J. M. 1973, ApJ, 183, 237

Bardeen, J. M., Press, W. H., & Teukolsky, S. A. 1972, ApJ, 178, 347

Beckwith, K., & Done, C. 2004, MNRAS, 352, 353

—. 2005, MNRAS, 359, 1217

Begelman, M. C. 2001, in ASP Conf. Ser. 250: Particles and Fields in Radio Galaxies Conference, 1–58381

Blaes, O. M. 2004, in Accretion Discs, Jets and High Energy Phenomena in Astrophysics, 137–185

Blandford, R. D. 2002, in Lighthouses of the Universe: The Most Luminous Celestial Objects and Their Use for Cosmology Proceedings of the MPA/ESO/, p. 381, 381–+

Boller, T., Brandt, W. N., & Fink, H. 1996, A&A, 305, 53

Boroson, T. A. 2002, ApJ, 565, 78

Bower, G. C., Falcke, H., Herrnstein, R. M., Zhao, J., Goss, W. M., & Backer, D. C. 2004, Science, 304, 704

Brandt, W. N., Mathur, S., & Elvis, M. 1997, MNRAS, 285, L25

Bursa, M., Abramowicz, M. A., Karas, V., & Kluźniak, W. 2004, ApJ, 617, L45

Čadež, A., Calvani, M., & Fanton, C. 2003, Memorie della Societa Astronomica Italiana, 74, 446

Čadež, A., Fanton, C., & Calvani, M. 1998, New Astronomy, 3, 647

Carter, B. 1968, Physical Review, 174, 1559

Chandrasekhar, S. 1961, Hydrodynamic and hydromagnetic stability (International Series of Monographs on Physics, Oxford: Clarendon, 1961)

—. 1983, The mathematical theory of black holes (Research supported by NSF. Oxford/New York, Clarendon Press/Oxford University Press (International Series of Monographs on Physics. Volume 69), 1983, 663 p.)

Chen, K., & Halpern, J. P. 1990, ApJ, 354, L1

Coppi, P. S. 1999, in ASP Conf. Ser. 161: High Energy Processes in Accreting Black Holes, 375–+

Cunningham, C. 1976, ApJ, 208, 534

Cunningham, C. T. 1975, ApJ, 202, 788

de Felice, F., & Preti, G. 1999, Classical and Quantum Gravity, 16, 2929

De Villiers, J., & Hawley, J. F. 2003a, ApJ, 589, 458

—. 2003b, ApJ, 592, 1060

De Villiers, J., Hawley, J. F., & Krolik, J. H. 2003, ApJ, 599, 1238

De Villiers, J., Hawley, J. F., Krolik, J. H., & Hirose, S. 2005, ApJ, 620, 878

Done, C., & Gierliński, M. 2003, MNRAS, 342, 1041

—. 2004, Progress of Theoretical Physics Supplement, 155, 9

Done, C., & Gierlinski, M. 2005, ArXiv Astrophysics e-prints

Dovčiak, M., Karas, V., & Yaqoob, T. 2004, ApJS, 153, 205

Ebisawa, K., Makino, F., Mitsuda, K., Belloni, T., Cowley, A. P., Schmidtke, P. C., & Treves, A. 1993, ApJ, 403, 684

Ebisawa, K., Mitsuda, K., & Hanawa, T. 1991, ApJ, 367, 213

Einstein, A. 1905, Annalen der Physik, 17, 891

—. 1916, Annalen der Physik, 49, 769

Eisenhauer, F., Schödel, R., Genzel, R., Ott, T., Tecza, M., Abuter, R., Eckart, A., & Alexander, T. 2003, ApJ, 597, L121

Elvis, M., Wilkes, B. J., McDowell, J. C., Green, R. F., Bechtold, J., Willner, S. P., Oey, M. S., Polomski, E., & Cutri, R. 1994, ApJS, 95, 1

Fabian, A. C., Iwasawa, K., Reynolds, C. S., & Young, A. J. 2000, PASP, 112, 1145

Fabian, A. C., & Miniutti, G. 2005, ArXiv Astrophysics e-prints

Fabian, A. C., Rees, M. J., Stella, L., & White, N. E. 1989, MNRAS, 238, 729

Fabian, A. C., & Vaughan, S. 2003, MNRAS, 340, L28

Falcke, H., Melia, F., & Agol, E. 2000, ApJ, 528, L13

Fanton, C., Calvani, M., de Felice, F., & Cadez, A. 1997, PASJ, 49, 159

Fender, R., & Belloni, T. 2004, ARA&A, 42, 317

Fender, R., Belloni, T., & Gallo, E. 2005, ArXiv Astrophysics e-prints

Fender, R. P., Belloni, T. M., & Gallo, E. 2004, MNRAS, 355, 1105

Frank, J., King, A., & Raine, D. J. 2002, Accretion Power in Astrophysics: Third Edition (Accretion Power in Astrophysics: Third Edition, by Juhan Frank, Andrew King, and Derek J. Raine. Cambridge University Press, 2002, 398 pp.)

Fukue, J. 2003, PASJ, 55, 155

Gendreau, K. C., White, N., Owens, S., Cash, W., Shipley, A., & Joy, M. 2001, in Liege International Astrophysical Colloquia, 11–16

George, I. M., & Fabian, A. C. 1991, MNRAS, 249, 352

Ghez, A. M., Duchêne, G., Matthews, K., Hornstein, S. D., Tanner, A., Larkin, J., Morris, M., Becklin, E. E., Salim, S., Kremenek, T., Thompson, D., Soifer, B. T., Neugebauer, G., & McLean, I. 2003, ApJ, 586, L127

Ghez, A. M., Salim, S., Hornstein, S. D., Tanner, A., Lu, J. R., Morris, M., Becklin, E. E., & Duchêne, G. 2005, ApJ, 620, 744

Gierliński, M., & Done, C. 2003, MNRAS, 342, 1083

—. 2004, MNRAS, 347, 885

Gierliński, M., Maciołek-Niedźwiecki, A., & Ebisawa, K. 2001, MNRAS, 325, 1253

Gilfanov, M., Churazov, E., & Revnivtsev, M. 2000, in Proceedings of 5-th Sino-German workshop on Astrohpysics, 1999, Eds. Gang Zhao, Jun-Jie Wang, Hong Mei Qiu and Gerhard Boerner, SGSC Conference Series, vol.1, pp.114-123, 114–123

Goldstein, H. 1950, Classical mechanics (Addison-Wesley World Student Series, Reading, Mass.: Addison-Wesley, 1950)

Hirose, S., Krolik, J. H., De Villiers, J., & Hawley, J. F. 2004, ApJ, 606, 1083

Hollywood, J. M., & Melia, F. 1997, ApJS, 112, 423

Iwasawa, K., Fabian, A. C., Reynolds, C. S., Nandra, K., Otani, C., Inoue, H., Hayashida, K., Brandt, W. N., Dotani, T., Kunieda, H., Matsuoka, M., & Tanaka, Y. 1996, MNRAS, 282, 1038

Jackson, J. D. 1975, Classical electrodynamics (92/12/31, New York: Wiley, 1975, 2nd ed.)

Karas, V., Lanza, A., & Vokrouhlicky, D. 1995, ApJ, 440, 108

Karas, V., Martocchia, A., & Subr, L. 2001, PASJ, 53, 189

Karas, V., Vokrouhlicky, D., & Polnarev, A. G. 1992, MNRAS, 259, 569

Kaspi, S., Brandt, W. N., George, I. M., Netzer, H., Crenshaw, D. M., Gabel, J. R., Hamann, F. W., Kaiser, M. E., Koratkar, A., Kraemer, S. B., Kriss, G. A., Mathur, S., Mushotzky, R. F., Nandra, K., Peterson, B. M., Shields, J. C., Turner, T. J., & Zheng, W. 2002, ApJ, 574, 643

Kerr, R. P. 1963, Physical Review Letters, 11, 237

Koratkar, A., & Blaes, O. 1999, PASP, 111, 1

Krolik, J. H. 1999, Active galactic nuclei : from the central black hole to the galactic environment (Active galactic nuclei : from the central black hole to the galactic environment /Julian H. Krolik. Princeton, N. J. : Princeton University Press, c1999.)

Krolik, J. H., & Hawley, J. F. 2002, ApJ, 573, 754

Krolik, J. H., Hawley, J. F., & Hirose, S. 2005, ApJ, 622, 1008

Kubota, A., Marshall, F., Makishima, K., Dotani, T., Ueda, Y., & Negoro, H. 1999, Astronomische Nachrichten, 320, 353

Kurpiewski, A., & Jaroszyński, M. 1999, A&A, 346, 713

Laor, A. 1991, ApJ, 376, 90

Laor, A., Fiore, F., Elvis, M., Wilkes, B. J., & McDowell, J. C. 1997, ApJ, 477, 93

Laor, A., & Netzer, H. 1989, MNRAS, 238, 897

Laor, A., Netzer, H., & Piran, T. 1990, MNRAS, 242, 560

Li, L., Zimmerman, E. R., Narayan, R., & McClintock, J. E. 2005, ApJS, 157, 335

Lindquist, R. W. 1966, Annals of Physics, 37, 487

Lorentz, H. A. 1928, Contributions from the Mount Wilson Observatory / Carnegie Institution of Washington, 373, 5

Lubiński, P., & Zdziarski, A. A. 2001, MNRAS, 323, L37

Luminet, J.-P. 1979, A&A, 75, 228

Lynden-Bell, D. 1969, Nature, 223, 690

Magorrian, J., Tremaine, S., Richstone, D., Bender, R., Bower, G., Dressler, A., Faber, S. M., Gebhardt, K., Green, R., Grillmair, C., Kormendy, J., & Lauer, T. 1998, AJ, 115, 2285

Makishima, K., Kubota, A., Mizuno, T., Ohnishi, T., Tashiro, M., Aruga, Y., Asai, K., Dotani, T., Mitsuda, K., Ueda, Y., Uno, S., Yamaoka, K., Ebisawa, K., Kohmura, Y., & Okada, K. 2000, ApJ, 535, 632

Martocchia, A. 2000, PhD thesis, SISSA-ISAS, Trieste, Italy

Martocchia, A., Karas, V., & Matt, G. 2000, MNRAS, 312, 817

Martocchia, A., & Matt, G. 1997, in General Relativity and Gravitational Physics; Proceedings of the 12th Italian Conference, edited by M. Bassan, V. Ferrari, M. Francaviglia, F. Fucito, and I. Modena. World Scientific Press, 1997., p.419, 419–+

Matt, G., Brandt, W. N., & Fabian, A. C. 1996, MNRAS, 280, 823

Matt, G., Fabian, A. C., & Ross, R. R. 1993a, MNRAS, 262, 179

Matt, G., Perola, G. C., & Piro, L. 1991, A&A, 247, 25

Matt, G., Perola, G. C., & Stella, L. 1993b, A&A, 267, 643

McClintock, J. E., Narayan, R., & Rybicki, G. B. 2004, ApJ, 615, 402

McClintock, J. E., & Remillard, R. A. 2003, ArXiv Astrophysics e-prints

Meier, D. L. 2003, New Astronomy Review, 47, 667

Michell, J. 1784, Philosophical Transactions Series I, 74, 35

Miller, J. M., Fabian, A. C., Nowak, M. A., & Lewin, W. H. G. 2004, ArXiv Astrophysics e-prints

Miller, M. C., & Colbert, E. J. M. 2004, International Journal of Modern Physics D, 13, 1

Misner, C. W., Thorne, K. S., & Wheeler, J. A. 1973, Gravitation (San Francisco: W.H. Freeman and Co., 1973)

Nandra, K., George, I. M., Mushotzky, R. F., Turner, T. J., & Yaqoob, T. 1997, ApJ, 477, 602

Nandra, K., Pounds, K. A., Stewart, G. C., Fabian, A. C., & Rees, M. J. 1989, MNRAS, 236, 39P

Narayan, R., Garcia, M. R., & McClintock, J. E. 1997, ApJ, 478, L79+

Narayan, R., & Heyl, J. S. 2002, ApJ, 574, L139

Narayan, R., & Yi, I. 1995, ApJ, 452, 710

Nayakshin, S., Kazanas, D., & Kallman, T. R. 2000, ApJ, 537, 833

Novikov, I. D., & Thorne, K. S. 1973, Black Holes: Les Astres Occlus, ed. ed. C DeWitt & B. DeWitt (New York; Gordon and Breach)

Page, D. N., & Thorne, K. S. 1974, ApJ, 191, 499

Pounds, K. A., Nandra, K., Stewart, G. C., George, I. M., & Fabian, A. C. 1990, Nature, 344, 132

Psaltis, D., & Norman, C. 2000, ArXiv Astrophysics e-prints

Rauch, K. P., & Blandford, R. D. 1994, ApJ, 421, 46

Reynolds, C. S. 1996, Ph.D. Thesis

Reynolds, C. S., & Begelman, M. C. 1997, ApJ, 488, 109

Reynolds, C. S., & Nowak, M. A. 2003, Phys. Rep., 377, 389

Reynolds, C. S., Wilms, J., Begelman, M. C., Staubert, R., & Kendziorra, E. 2004, MNRAS, 349, 1153

Rosner, R., Golub, L., Coppi, B., & Vaiana, G. S. 1978, ApJ, 222, 317

Ross, R. R., & Fabian, A. C. 1993, MNRAS, 261, 74

—. 2005, MNRAS, 358, 211

Ross, R. R., Fabian, A. C., & Young, A. J. 1999, MNRAS, 306, 461

Różańska, A., & Czerny, B. 2000, A&A, 360, 1170

Rybicki, G. B., & Lightman, A. P. 1979, Radiative processes in astrophysics (New York, Wiley-Interscience, 1979. 393 p.)

Sanders, D. B., Phinney, E. S., Neugebauer, G., Soifer, B. T., & Matthews, K. 1989, ApJ, 347, 29

Schödel, R., Ott, T., Genzel, R., Hofmann, R., Lehnert, M., Eckart, A., Mouawad, N., Alexander, T., Reid, M. J., Lenzen, R., Hartung, M., Lacombe, F., Rouan, D., Gendron, E., Rousset, G., Lagrange, A.-M., Brandner, W., Ageorges, N., Lidman, C., Moorwood, A. F. M., Spyromilio, J., Hubin, N., & Menten, K. M. 2002, Nature, 419, 694

Schurch, N. J., & Warwick, R. S. 2002, MNRAS, 334, 811

Schurch, N. J., Warwick, R. S., Griffiths, R. E., & Sembay, S. 2003, MNRAS, 345, 423

Shakura, N. I., & Sunyaev, R. A. 1973, A&A, 24, 337

Stella, L., Vietri, M., & Morsink, S. M. 1999, ApJ, 524, L63

Strohmayer, T. E. 2001a, ApJ, 552, L49

—. 2001b, ApJ, 554, L169

Takahashi, R. 2004, ApJ, 611, 996

Tanaka, Y., Nandra, K., Fabian, A. C., Inoue, H., Otani, C., Dotani, T., Hayashida, K., Iwasawa, K., Kii, T., Kunieda, H., Makino, F., & Matsuoka, M. 1995, Nature, 375, 659

Thorne, K. S. 1974, ApJ, 191, 507

Titarchuk, L., Lapidus, I., & Muslimov, A. 1998, ApJ, 499, 315

Turner, N. J. 2004, ApJ, 605, L45

Turner, N. J., Blaes, O. M., Socrates, A., Begelman, M. C., & Davis, S. W. 2005, ApJ, 624, 267

Vaughan, S., & Fabian, A. C. 2004, MNRAS, 348, 1415

Velikhov, E. P. 1959, Soviet Physics JETP-USSR, 9, 995

Viergutz, S. U. 1993, A&A, 272, 355

Weisstein, E. W. 2005, MathWorld – A Wolfram Web Resource.

Wilkins, D. C. 1972, Phys. Rev. D, 5, 814

Will, C. 2001, Living Reviews in Relativity, 4, 4

Wilms, J., Reynolds, C. S., Begelman, M. C., Reeves, J., Molendi, S., Staubert, R., & Kendziorra, E. 2001, MNRAS, 328, L27

Zakharov, A. F., & Repin, S. V. 2003, A&A, 406, 7

Zdziarski, A. A., & Gierliński, M. 2004, Progress of Theoretical Physics Supplement, 155, 99

Zdziarski, A. A., Johnson, W. N., & Magdziarz, P. 1996, MNRAS, 283, 193

Życki, P. T., Done, C., & Smith, D. A. 1999, MNRAS, 309, 561

Życki, P. T., Done, C., & Smith, D. A. 1999, MNRAS, 305, 231